AFOSR. TR. 89-0302

AD-A206 257

FREE RADICAL-SURFACE INTERACTIONS USING MULTIPHOTON IONIZATION OF FREE RADICALS

January 1989

Final Technical Report
Covering Period: 1 October 1985 to 30 September 1988

By: Robert M. Robertson, David M. Golden,
and Michel J. Rossi
Department of Chemical Kinetics
SRI International, Menlo Park CA 94025-3493

Prepared for:

AIR FORCE OFFICE OF SCIENTIFIC RESEARCH
Directorate of Chemical and Atmospheric Sciences
(AFSC) Building 410
Bolling Air Force Base
Washington, DC 20332-6448

Attention: Major Larry P. Davis

Contract No. F49620-86-K-0001

SRI Project PYU-1227

DTIC
ELECTE
MAR 1 0 1989
S D
H

SRI International
333 Ravenswood Avenue
Menlo Park, California 94025-3493
(415) 326-6200
TWX: 910-373-2046
Telax: 334486

SRI International

89 3 09 045

FREE RADICAL-SURFACE INTERACTIONS USING MULTIPHOTON IONIZATION OF FREE RADICALS

January 1989

Final Technical Report
Covering Period: 1 October 1985 to 30 September 1988

By: Robert M. Robertson, David M. Golden,
and Michel J. Rossi
Department of Chemical Kinetics
SRI International, Menlo Park CA 94025-3493

Prepared for:

AIR FORCE OFFICE OF SCIENTIFIC RESEARCH
Directorate of Chemical and Atmospheric Sciences
(AFSC) Building 410
Bolling Air Force Base
Washington, DC 20332-6448

Attention: Major Larry P. Davis

Contract No. F49620-86-K-0001

SRI Project PYU-1227

Approved by:

David M. Golden, Laboratory Director
Chemistry Laboratory

G. R. Abrahamson
Senior Vice President
Sciences Group

REPORT DOCUMENTATION PAGE		Form Approved OMB No 0704 0188

1a REPORT SECURITY CLASSIFICATION UNCLASSIFIED	1b RESTRICTIVE MARKINGS
2a SECURITY CLASSIFICATION AUTHORITY	3 DISTRIBUTION / AVAILABILITY OF REPORT
2b DECLASSIFICATION / DOWNGRADING SCHEDULE	Approved for public release; distribution is unlimited.

4 PERFORMING ORGANIZATION REPORT NUMBER(S)	5 MONITORING ORGANIZATION REPORT NUMBER(S)

6a NAME OF PERFORMING ORGANIZATION SRI International	6b OFFICE SYMBOL (If applicable)	7a NAME OF MONITORING ORGANIZATION AFOSR/NC
6c ADDRESS (City, State, and ZIP Code) Menlo Park, CA 94025		7b ADDRESS (City, State, and ZIP Code) Building 410, Bolling AFB DC 20332-6448

8a NAME OF FUNDING / SPONSORING ORGANIZATION AFOSR	8b OFFICE SYMBOL (If applicable) NC	9 PROCUREMENT INSTRUMENT IDENTIFICATION NUMBER F49620-86-K-0001

8c ADDRESS (City, State, and ZIP Code) Building 410, Bolling AFB DC 20332-6448	10 SOURCE OF FUNDING NUMBERS			
	PROGRAM ELEMENT NO 61102F	PROJECT NO 2303	TASK NO B1	WORK UNIT ACCESSION NO

11. TITLE (Include Security Classification)
(U) FREE RADICAL-SURFACE INTERACTIONS USING MULTIPHOTON IONIZATION OF FREE RADICALS

12 PERSONAL AUTHOR(S)
Robert M. Robertson, David M. Golden, and Michel J. Rossi

13a TYPE OF REPORT Final Report	13b TIME COVERED FROM 10-1-85 TO 9-30-88	14 DATE OF REPORT (Year, Month, Day) January 1989	15 PAGE COUNT 109

16 SUPPLEMENTARY NOTATION

17 COSATI CODES			18. SUBJECT TERMS (Continue on reverse if necessary and identify by block number)
FIELD	GROUP	SUB-GROUP	(keyword index) Sticking Coefficients of Free Radicals and Atoms, REMPI of Free Radicals and Atoms, Cross Section for REMPI of Free Radicals and Atoms.

19 ABSTRACT (Continue on reverse if necessary and identify by block number)

Free Radical and Atom Surface interactions have been studied in a low pressure reactor (Knudsen cell) where the atomic and molecular transients predominantly collide with the walls of the reaction vessel. The approach taken involved generating the neutral transients using IR-multiphoton decomposition of an appropriate precursor and subsequently exposing the photolysis products to given surfaces at variable temperature (ambient to 450°C). The detection was performed by molecular beam sampling mass spectrometry and in situ Resonance Enhanced Multiphoton Ionization using a tunable dye laser. The combination of both techniques affords the possibility to determine the kinetics of the neutral transients in quantitative terms, that is competition between first order and second-order processes, and the determination of quantitative REMPI ionization cross sections. The heterogeneous loss rate constants are cast in the form of a sticking coefficient for a specific radical on a given surface.

We have investigated the interaction of CF_3 radical on SiO_2 and Si over a range of temperatures. SiH_2 has been investigated in its interaction with solid Si-containing surfaces, and I and Br atoms have been studied as to their reaction with various surfaces.

Silicon
Carbon trifluoride,
Silicon dioxide.
Argon

20 DISTRIBUTION / AVAILABILITY OF ABSTRACT ☐ UNCLASSIFIED/UNLIMITED ☒ SAME AS RPT ☐ DTIC USERS	21 ABSTRACT SECURITY CLASSIFICATION UNCLASSIFIED
22a NAME OF RESPONSIBLE INDIVIDUAL F J WODARCZYK	22b TELEPHONE (Include Area Code) (202) 767-4963	22c OFFICE SYMBOL AFOSR/NC

DD Form 1473, JUN 36   Previous editions are obsolete   SECURITY CLASSIFICATION OF THIS

CONTENTS

EXECUTIVE SUMMARY

APPENDICES

For

A-1

EXECUTIVE SUMMARY

Support by AFOSR from 1985 to 1988 has enabled us to study the interaction of free radicals and atoms with surfaces of technological interest. The primary economic force impetus for such an endeavor is represented by the multi-billion-dollar-a-year semiconductor processing industry, whose independence from foreign suppliers possesses strategic significance for the United States. Our contribution has been to provide fundamental understanding of two archetypical processes upon which the industry is based, namely, etching and deposition. Understanding on the molecular level affords control of these two prototypical processes, resulting in bypassing the labor-intensive and time-consuming process of trial and error that dominates the industry.

Despite some progress, the application of the limited fundamental knowledge to real-world conditions is still in its infancy. Our work is intended to bridge the gap between single crystal studies typically conducted at a fraction of a monolayer coverage and high pressure studies addressing practical deposition or etching situations. Accordingly, the surfaces we studied were of technological importance and are not yet well characterized. However, our results are reproducible, indicating sufficient control of the surface conditions from one experiment to another.

The hallmark of our experiments was the generation of a well-defined gas-phase neutral transient, either an atom or a free radical, in the absence of other competing reactive species, and the subsequent study of its heterogeneous interaction with a surface of interest. Because we

1

determined the number density of the neutral transient, we are able to extract quantitative data on its heterogeneous chemistry with various surfaces under different experimental conditions.

Specific results of our research are presented in Appendices A through H, which are papers that have already appeared or will appear in the open literature. Following is a brief overview of the work reported in Appendices A through H.

Appendix A

We investigated the reactivity of CF_3 radicals on SiO_2 using an improved version of our low pressure reactor. The Knudsen cell reactor was a gold-coated stainless steel vessel with an internal resistive heater whose background pressure was $\sim 10^{-7}$ Torr, representing an improvement of two orders of magnitude over the previously used gold-coated Pyrex vessel. Our main conclusion was the fact that CF_3 was inert toward SiO_2, even at temperatures up to 350°C. This finding contradicted the rule of thumb, derived from discharge studies, that fluorocarbon free radicals are responsible for SiO_2 etching.

Appendices B and E

These two papers describe the heterogeneous interaction of CF_3 radicals with single-crystal silicon. The temperature of the silicon wafer was varied from room temperature up to 450°C, and etching of Si was observed, albeit at rates that are unimportant in a practical environment. However, the initial etching efficiency of CF_3 approached that of F_2 at higher temperatures. Furthermore, the etching efficiency

was not constant but decreased with increasing exposure of CF_3 to Si and approached a steady-state value of 10% to 50% of the initial value, depending on experimental conditions. This result implies that etching still continues, even though a fluorocarbon layer forms on the Si surface.

Appendices C and D

The next step in our investigations was the application of a new technique with which we were able to monitor the gas-phase density of the transient inside the Knudsen cell. Resonance-enhanced multiphoton ionization (REMPI) of atoms and free radicals afforded new opportunities of detecting short-lived transient species in real time, and we made a considerable effort to validate our experimental procedure. We showed that quantitative kinetic information could be obtained when the REMPI signals were calibrated using the on-line mass spectrometer, even if the kinetics consisted of concurrent first and second order processes. In addition, we characterized the REMPI spectra of I and Br and their kinetic behavior inside a Knudsen cell.

Appendices F, G, and H

Finally, we turned our attention to SiH_2, a free radical thought to be important in the deposition of hydrogenated amorphous silicon. Because the REMPI spectrum of SiH_2 was not known, we had to secure its assignment. We determined the sticking coefficient of SiH_2 on a growing hydrogenated amorphous silicon surface to be between 0.10 and 0.15, depending on the nature of the surface. This result was somewhat surprising, since modeling results had suggested significantly higher values than the above. However, the growing surface was at ambient

temperature, which could affect the sticking coefficient if the insertion of SiH_2 into Si-H bonds had a small activation energy. We also found that highly vibrationally excited SiH_2 with 7000 cm^{-1} of excess energy is deactivated upon every collision (essentially unit efficiency) with the above-mentioned growing hydrogen-containing Si surface.

Appendix A

KINETICS OF SURFACE REACTIONS OF CF_3 RADICALS

Kinetics of surface reactions of CF$_3$ radicals

Robert M. Robertson,[a] Michel J. Rossi, and David M. Golden

Department of Chemical Kinetics, SRI International, Menlo Park, California 94025

The kinetics of reactions of CF$_3$ radicals on various substrate materials has been studied in a gold-coated, stainless-steel, very-low-pressure photolysis (VLPΦ) cell as a function of temperature and radical concentration. The substrate materials were gold, stainless steel, copper, copper oxide, and silica. The CF$_3$ radicals were generated from CF$_3$I by IR-multiphoton decomposition. The reaction products observed with a mass spectrometer included HF, CO, CO$_2$, COF$_2$, SiF$_4$, and C$_2$F$_6$. Rate constants were obtained as a function of temperature. CF$_3$ reacted most rapidly on copper oxide surfaces; the other metal surfaces were less reactive, and the silica surfaces were least reactive. Previous studies from this laboratory that had reported the reaction of CF$_3$ on fused silica are reinterpreted as reactions of CF$_3$ on the stainless-steel heater assembly.

I. INTRODUCTION

The dry processing techniques used in the semiconductor industry involve very complex chemical systems. The ability to better control the processes and improve their capabilities depends on a better quantitative understanding of the elementary steps in these reaction systems. Dry-etching processes usually take place in vacuum systems and are energized by electrical discharges (dc or rf). The details of the chemistry and physics in those systems are not fully understood, but some useful rules that guide the operation of commercial plasma or reactive ion etchers have emerged.[1,2] The conventional wisdom in silicon and silicon-dioxide etching by fluorocarbon discharges is that small additions of O$_2$ enhance the etch selectivity toward Si, whereas the addition of H$_2$ enhances the selectivity toward SiO$_2$. This rule is understood by analyzing the effect of these additives on the gas composition in the discharge. O$_2$ will cause the gas to be fluorine rich through the reaction of O$_2$ with CF$_x$ radicals to produce saturated molecules, such as CO, CO$_2$, and COF$_2$, and F atoms. H$_2$ will cause CF$_x$ radicals to be the dominant reactive species because hydrogen will react with the F atoms. The implication of this empirical rule is that F atoms are mainly responsible for Si etching, whereas perfluorocarbon radicals CF$_x$ are primarily responsible for SiO$_2$ etching.

Some time ago, we began studying individual free radical–surface reactions to obtain a fundamental understanding of the reaction mechanism and kinetics with the goal of systematizing and codifying the rate data. We found few experimental studies of the gas–surface interaction of neutral transients (atoms,[3] radicals,[4-7] and metastable species) with surfaces of technological interest; in contrast, many studies were performed to gain a quantitative understanding of the fundamental interaction of ionic species[8-10] (atomic and molecular) with these surfaces. The basic philosophy of our program consists of generating a particular neutral species at low pressures commensurate with dry processing conditions and studying its interaction with selected surfaces as to the kinetics, reaction pathways, branching ratios as a function of temperature, and more.

The subject of the present paper is the study of a typical perfluorocarbon radical CF$_3$ in its interaction with SiO$_2$, in-

vestigating the above simple rule on oxide etching. In an earlier report,[11] we presented our results on the same reaction system conducted in a Pyrex reaction cell in the presence of background concentrations of the order of 2×10^{12} molecules cm^{-3} H$_2$O. This study reports on the same system in a stainless-steel cell where H$_2$O levels of about 2×10^{10} molecules cm^{-3} could be achieved after thorough bakeout. However, in most experiments, the H$_2$O background level in the stainless-steel reaction cell was of the same order or less than our earlier study because a thorough bakeout of the cell was not always performed.

II. BACKGROUND

In the earlier study, the reaction of CF$_3$ on silica surfaces took place in a very-low-pressure photolysis (VLPΦ) cell made of Pyrex that was subsequently gold coated. The VLPΦ cell is a Knudsen flow reactor with typical pressures below 10^{-3} Torr and gas residence times of ~ 1 s. A silica sample was placed in the gold-coated Pyrex cell with a stainless-steel heater and thermocouples. The source gas and products that effused from the reactor were monitored with a mass spectrometer using phase-sensitive detection. CF$_3$ radicals were generated from CF$_3$I by infrared-multiphoton decomposition (IR-MPD) using a CO$_2$-TEA laser. The laser was operated at 20 Hz, producing a depletion of 5% to 15% of the source gas and a steady-state concentration of CF$_3$.

The fractional decrease of the mass spectrometric signal at steady state was monitored at a fragment peak corresponding solely to the reactant CF$_3$I and was taken as a measure of the extent of IR-MPD under the given conditions. The reaction scheme for the production and reaction of the CF$_3$ radicals is as follows:

$$CF_3I + nh\nu \rightarrow CF_3 + I. \tag{1}$$

$$CF_3 + CF_3 \xrightarrow{k_2} C_2F_6, \tag{2}$$

$$CF_3 \xrightarrow{k_3} escape, \tag{3}$$

$$CF_3 + surface \xrightarrow{k_w} loss. \tag{4}$$

where k_r is the second-order gas-phase recombination rate constant[12,13] of the radicals, k_e is the first-order rate constant for escape of the radicals out of the reactor, and k_w is the total first-order wall loss rate constant of CF_3. This rate constant includes any wall loss for the whole reaction vessel, whether on a hot or cold wall, and whether the CF_3 remains adsorbed on the wall or contributes to product formation. The gas-phase products were reported to be CO, CO_2, COF_2, HF, C_2F_6, and SiF_4. Iodine atom from reaction (1) has been found unreactive with the surfaces investigated in this report, presumably because of the endothermic nature of its reactions with adsorbed atoms and molecules in view of the weakness of bonds involving iodine.

The rate parameters of primary interest were the first-order CO production rate constant k_{CO} taken to be representative of the surface reaction pathway of CF_3, and the total wall loss rate k_w. k_{CO} is determined by examining the CO concentrations as a function of radical density and temperature. k_w can be determined through a steady-state analysis of the above reaction scheme. The rate constant for gas-phase CF_3 radical recombination k_r can be measured in our VLPΦ flow reactor by monitoring the yield of the recombination product C_2F_6 as a function of flow rate (or concentration) of the free radical CF_3. In the absence of free radical wall losses, this dependence would be quadratic because of the bimolecular nature of the elementary radical recombination step. Experimentally, however, we find a departure from this quadratic dependence, and the extent of this effect is proportional to k_w.

Algebraically, we can linearize the equations governing the steady-state reaction system, reactions (1)–(4), with the result shown in Eq. (5):

$$f \times F'_{CF_3I}/F^0_{C_2F_6} = 2 + (k_e + k_w)k_r^{-1/2}V^{1/2}(F^0_{C_2F_6})^{-1/2},$$
(5)

where F'_{CF_3I} is the initial flow rate of CF_3I, $F^0_{C_2F_6}$ is the flow rate of C_2F_6 out of the reactor with the laser on, f is the extent of depletion of the source gas, and V is the volume of the cell. Since k_e and k_r are known, or have been measured in the absence of active surfaces,[12] and f, F'_{CF_3I}, and $F^0_{C_2F_6}$ are measured, the only undetermined parameter in this expression is k_w. In a plot of $fF'_{CF_3I}/F^0_{C_2F_6}$ vs $(F^0_{C_2F_6})^{-1/2}$, the slope of the line is related to k_w. The intercept of 2 results because the gas-phase loss reaction is second order in CF_3.

The advantage of our VLPΦ method, as with all stirred-flow reactors, is that the gas-phase densities of all species can be calculated if the absolute rate constants are known or can be measured. An expression for the steady-state free radical density of CF_3 has been derived[11] for the above reaction system [Eqs. (1)–(4)]. Also, it is possible to derive the radical sticking coefficient and etch efficiency because the gas–wall collision frequency has a simple geometric dependence. The first-order rate constant for the escape of radicals out of the reactor is shown in Eq. (6):

$$k_e = \tfrac{1}{4} v_{th} A_{exit}/V,$$
(6)

where v_{th} is the thermal molecular velocity of CF_3 and A_{exit} is the area of the exit aperture. Analogously, the gas–wall collision rate constant k_{coll}, sometimes referred to as collision frequency, for CF_3 with substrate is given in Eq. (7):

$$k_{coll} = \tfrac{1}{4} v_{th} A_{subst}/V,$$
(7)

where A_{subst} is the area of the sample substrate. The CF_3 sticking coefficient γ is then given by Eq. (8):

$$\gamma = k_w/k_{coll},$$
(8)

where k_w has been corrected by subtracting any cold wall losses. The etch efficiency ϵ is also easily derived:

$$\epsilon = \frac{F^0_{SiF_4}}{Vk_{coll}[CF_3]},$$
(9)

where $F^0_{SiF_4}$ is the flow of SiF_4 out of the reactor.

Selamoglu et al.[11] concluded that the surface reactions of CF_3 were occurring on the hot silica surface and not on the cold walls or the heater assembly (by doing the appropriate control experiments and temperature variation experiments). Through the use of isotopic analogs, they were able to conclude that the primary surface reaction of CF_3 on silica was with ambient adsorbed water, and this reaction produced the products containing oxygen and hydrogen. There was very little etching of the silica surface under their conditions in view of the small yields of SiF_4.

This paper reports the follow-up experiments to these initial results. The intent was to be able to reduce the ambient water levels in the reactor, so that the etching reaction could be measured with higher sensitivity and the effect of water could be better studied and quantified. For this purpose, the gold-coated Pyrex cell was replaced with a bakable stainless-steel VLPΦ cell. With this new apparatus, the reaction of CF_3 with water proceeded rapidly on hot metal surfaces. This conclusion requires that the results of the earlier experiments[11] be reinterpreted as occurring on the metal surfaces of the given heater assembly (stainless steel) and not on the silica surface as had been reported.

III. EXPERIMENTAL

The gold-coated Pyrex VLPΦ cell of the earlier experiments was replaced with a bakable stainless-steel cell. The cell, shown in Fig. 1, is built around a 2⅜-in. metal-gasketed cube. Two sides are used to mount KCl windows, giving a path length of 15 cm for the CO_2-TEA laser infrared beam
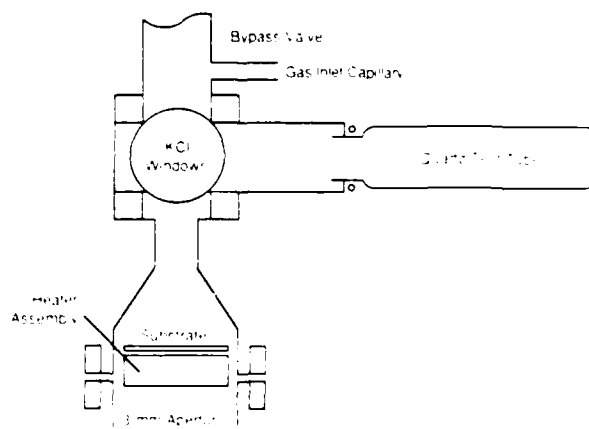

FIG. 1. VLPΦ cell used to study radical–surface interactions. The infrared laser enters the cell perpendicular to the plane of the diagram through salt windows.

[the $R(16)$ line of the 9.6-μm band]. The laser provides pulse energies of ~ 1 J, and the beam area at the cell is 1 cm^2. One of the sides is connected to a bypass valve and 1.5-in.-diam tubing for evacuating the cell. The heater assembly and 2-in.-diam substrate are contained in the lower extension. The 3-mm exit aperture that leads to the chopper and mass spectrometer is located at the end of this extension. Another side of the cube is used to mount a quartz test tube. The radical precursor gas, water vapor, and other gases flow into the cell through capillary tubes that connect to the glass gas-handling system. The inside walls of the reactor were coated with gold by vacuum evaporation. The total cell volume is 665 cm^3, and the total surface area is 680 cm^2. For CF$_3$, the escape rate constant is 0.46 s^{-1}, and the substrate collision rate constant is 230 s^{-1}. In order to transfer these rate constants for other species, it is necessary to include the factor $(T/M)^{1/2}$, where T is the cold-wall temperature and M is the molecular mass.

Two methods are used to produce hot sample surfaces. The primary method is the use of the heater and substrate inside the cell because it allows easy exchange of various substrate materials. The heater assembly is 2 in. in diameter and $\frac{3}{4}$ in. high. It consists of two metal disks with a flat spiral stainless-steel-clad immersion heater clamped between them. The substrate disk is placed on top of the heater assembly, facing the region where the radicals are produced. The materials used to make the substrate disks and the heater assembly are discussed below. The area of the substrate is 20 cm^2, and the area of the exposed heater with the substrate in place is 40 cm^2. Thermal contact between the heater and the substrate is maintained by using a thin liquid film of gallium between the two materials. The temperature of the substrate is measured with a thermocouple placed in a well in the heater block.

The second method of creating a hot-sample surface is to use a quartz test tube, which is connected to the cell with a Viton O-ring fitting. The test tube is 36 mm in diameter and has an overall length of 165 mm. The hot surface area, 130 cm^2, is produced using heating tape that is wrapped around the outside of the quartz test tube. The temperature is measured with thermocouples on the outside surface of the test tube. Inhomogeneous heating produces temperature variations of 15 °C along the length of the test tube. This method of creating a hot surface does not allow us to easily change the substrate material, but it does enable us to place the heater outside the vacuum.

The mass spectrometer signals are identified and calibrated by comparison with authentic samples of the gases of primary interest: CO, CO$_2$, COF$_2$, C$_2$F$_6$, and the source gas CF$_3$I. These gases were monitored at the m/e values of 28, 44, 47, 119, and 196, respectively. We assume that the signal at the above m/e value is due only to the respective parent molecule. This assumption should cause only minor signal contributions at the lower mass peaks. The signal at $m/e = 20$ corresponded to HF, which was not quantitatively monitored because of well-known sampling problems.

The other mass peak that is monitored is at $m/e = 85$. In previous work in this laboratory, this peak was identified as SiF$_3$ from SiF$_4$, which was produced by etching of the silica

surface. (Also, it is known that CF$_3$ will quantitatively form CO and SiF$_4$ in a quartz reactor at temperatures around 1000 K.) However, this identification is uncertain because in the experiments discussed below, this peak is still present when no obvious source of silicon is present in the cell. The next most likely candidate for this mass peak is CF$_3$O$^+$ from CF$_3$O or some heavier parent molecule. The usual mass spectrometer tests using low-resolution (quadrupole) instruments cannot distinguish between CF$_3$O$^+$ and SiF$_3^+$ at $m/e = 85$. The presence of a heavier parent peak or other lighter fragment peaks will not be conclusive in identifying the $m/e = 85$ signal because the Si/F species and C/O/F species are expected to have overlapping peaks. The expected appearance potentials of the candidate ions are too close to be resolved with our mass spectrometer.

Two experiments were done in an effort to show that the signal might be due to a C/F/O species. The first was a trapping experiment with NO$_2$. We know the rate constant for the reactions of CF$_3$ with NO$_2$,[14] which is similar to that reported[15,16] for CH$_3$ with NO$_2$. The initial product is expected to be CF$_3$O, which may react to form other species or may survive sufficient gas-wall collisions to reach the ionizer of the mass spectrometer. The trapping experiments were done at room temperature with CF$_3$I flow of $3.5 \cdot 10^{15}$ molecules s^{-1} and with NO$_2$ flows of 4×10^{15} and $1 \cdot 10^{16}$. The depletion of the feed gas by IR-MPD was 20%, and in the presence of NO$_2$ the signals for CO, CO$_2$, and COF$_2$ increased significantly. The signal at $m/e = 85$ increased only slightly over its background level, possibly due to other secondary effects. This test was thus not conclusive in identifying the $m/e = 85$ signal.

The second experiment used H$_2$^{18}O to test for the presence of oxygen in the $m/e = 85$ signal. In this test, the appearance of a new peak at $m/e = 87$ would be identified as the ion of CF$_3$^{18}O. The cell was conditioned with the isotopic water overnight at a static pressure of several Torr to ensure that this water would be incorporated into reactive surface sites. The resulting change in the mass spectra at high temperature and our usual flow conditions was the appearance of isotopic analogs of CO, CO$_2$, and COF$_2$, as seen in earlier experiments.[11] However, there was no change in the signal at $m/e = 87$. Thus, we conclude that the signal at $m/e = 85$ cannot be due to a C/F/O species.

Under our usual conditions, there is insufficient signal at the $m/e = 86$ and 87 peaks to determine if they are due to the silicon isotopes of the $m/e = 85$ (5.1% and 3.4% of the m/e 85 peak). However, at more extreme conditions (425 °C, CF$_3$I flow of 2×10^{16}, and laser depletion of 30%), there is enough signal to confirm that these signals are due to silicon isotopes. The signals depend on the presence of CF$_3$I and high temperature, and the signals increase by a factor of 3 when the laser is on. In this test, a stainless-steel heater was used without a silicon oxide or silicon substrate, i.e., no materials obviously containing silicon were present in the cell.

These observations were done under extreme conditions, but we expect that the same source of the signal is present at lower temperature. Thus, we conclude that the signal at $m/e = 85$ is due to SiF$_3^+$ from SiF$_4$, which is produced in a reaction of CF$_3$ with a silicon impurity in the heated metallic

materials of the VLPΦ cell, most likely, the heater assembly. The mass spectrometer signal was then calibrated using an authentic sample of SiF$_4$, whose flow into the reaction cell was measured together with the signal strength at $m/e = 85$.

IV. RESULTS AND DISCUSSION

A. Gold-coated heater assembly

The first set of experiments were done with a gold-coated copper heater assembly. The coating, applied by a high-purity electroplating technique, resulted in a thick, well-adhered gold coating. Three substrates were studied: gold, oxidized copper, and silica. The gold substrate was studied by leaving the gold-plated heater assembly empty. The oxidized copper was made by baking a disk of copper in atmosphere at 500 °C for 1 h. A macroscopic film of oxide resulted. The fused-silica disk was a ⅛-in.-thick optical window that had been etched in diluted HF until the surface developed a rough texture.

The products from the reaction of CF$_3$ with these surfaces were studied as a function of temperature at a constant CF$_3$I flow rate of 3.5×10^{15} molecules s^{-1} (6×10^{-4} Torr in the cell) and a constant source gas depletion of 20%. Figure 2 shows the densities of products in the reactor for the gold substrate Au/Au. (This notation indicates a gold substrate on top of a gold-plated heater assembly.) The trends in product densities versus temperature for the other substrate materials were similar.

Figure 3 shows the CO densities in the reactor for the three substrate materials. For the curve labeled Au/Au, 60 cm^2 of gold is exposed. For the curve labeled CuO$_x$/Au, 20 cm^2 of copper oxide and 40 cm^2 of gold are exposed. Similarly, for the curve labeled SiO$_2$/Au, 20 cm^2 of silica and 40 cm^2 of gold are exposed. Assuming that all exposed areas of gold
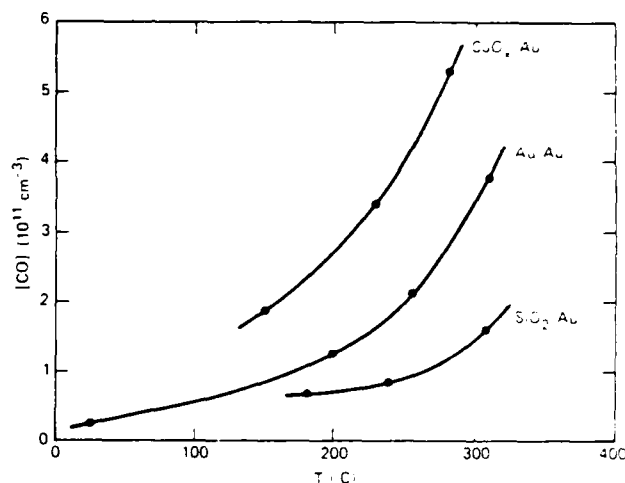
FIG. 3. CO concentration as a function of temperature for three substrate materials on the gold-plated heater assembly: gold (Au/Au), oxidized copper (CuO$_x$/Au), and fused silica (SiO$_2$/Au). The area of the substrate is 20 cm² and that of the heater assembly is 40 cm².

are equally reactive, we can subtract the contribution of the 40-cm^2 gold-plated heater assembly. This results in the conclusion that the oxidized copper is four times as reactive toward producing CO as the gold surface and that the silica surface is totally unreactive at our sensitivity.

A comparison of the CO$_2$, COF$_2$, and SiF$_4$ densities is less quantitative because of the weaker signals, but they all showed the reverse trend in that the gold was more reactive toward the production of these species than the oxidized copper. The silica was less reactive than either of the metals. The wall-loss rate coefficients k_w for all three situations were comparable to each other in magnitude and temperature dependence. The rates are discussed further in a following section. The ambient water densities for the Au/Au, CuO$_x$/Au, and SiO$_2$/Au experiments were 1.2×10^{12}, 9×10^{11}, and 8×10^{11} cm^{-3}, respectively.

The primary conclusion from this set of experiments is that CF$_3$ reacts on metal surfaces faster than on silica.

B. Other heater assembly materials

Stainless steel (SS) and unoxidized copper were also used to produce the heater assemblies. These materials were found to produce CO and the other products discussed above at rates comparable to the gold surface. Figure 4 shows the CO concentrations as a result of the CF$_3$–surface interaction in the reactor for several choices of substrate and heater assembly materials, as well as the results from the earlier study for comparison.[11] Two curves are shown for a stainless-steel heater assembly: one with a silica substrate, SiO$_2$/SS, and one without any substrate, SS/SS. A comparison of these two curves shows again that the silica is less reactive (if reactive at all) toward the production of CO than the metal surfaces.

The data for a clean, copper-heater assembly without a substrate, Cu/Cu, in Fig. 4, show that the reactivity of the clean copper is comparable to that of other metals. The curve for SiO$_2$/CuO$_x$ represents data taken with a highly oxidized, copper-heater assembly with a silica substrate in the stain-
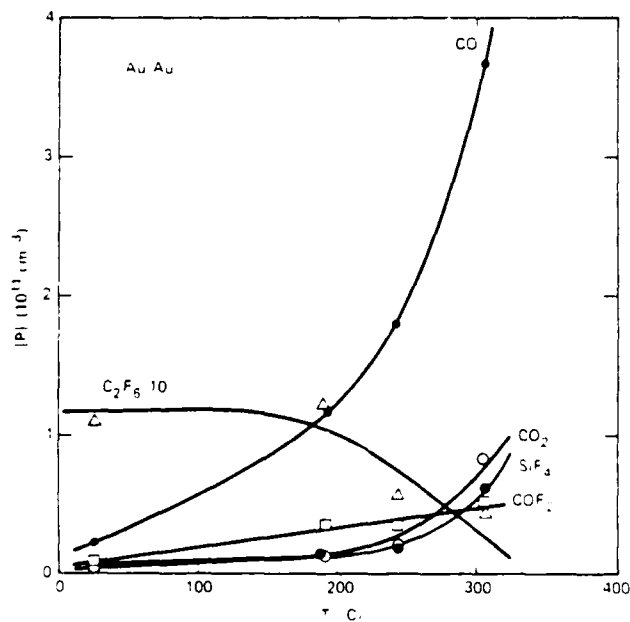

FIG. 2. Product concentrations as a function of temperature for the gold-plated heater assembly without a substrate, i.e., a gold substrate on the gold heater Au/Au. F$_{CF_3}$ = 3.5 · 10^{15} molecules s^{-1} and $f = 0.2$.

less-steel cell. These data are comparable to the data from the gold-coated Pyrex reactor of the previous experiments[11] [the dashed curve in Fig. 4 labeled SiO_2/SS (H_2O)] where the heater assembly was stainless steel and the ambient water density was high. In all of the current experiments, the water densities were comparable to the levels discussed in the previous section.

We conclude from these qualitative tests that the commonly available metals are all reactive and that other metals are not likely to provide an unreactive surface. The gold-coated heater assembly was chosen for many of the experiments because it was expected that the surface would change the least during the long periods of high-temperature exposure to CF_3 and the ambient water in the reactor. The copper-heater assembly was seen to oxidize excessively, producing a highly reactive surface. The stainless steel was also seen to oxidize over time, resulting in a somewhat less reactive surface.

C. Influence of water vapor

The effect of water vapor was investigated for several experimental configurations in an effort to reproduce the very large CO densities seen in previous experiments[11] where the water concentrations in the cell were typically 2×10^{12} cm^{-3}. Figure 5 shows the CO concentration as a function of H_2O densities for the stainless-steel heater assembly with a silica substrate. In one case where the water density was

FIG. 5. CO concentration as a function of H_2O concentration. Both sets of data were taken with a stainless-steel heater and a silica substrate. The curve that shows a CO dependence on water concentration was taken with a clean, new stainless-steel heater, whereas the stainless-steel heater was well oxidized for the case where no dependence on water vapor was observed. Typical flow and depletion conditions were used.

varied from 3×10^{11} to 1.5×10^{14}, no change in CO density was observed. In another case, there was an apparently linear dependence on water flow. The apparent cause of this difference is that the data that were independent of water concentrations were taken with a heater assembly that had an oxidized stainless-steel surface; whereas the data that showed a linear dependence on water concentration were taken with a new stainless-steel heater assembly that was not oxidized.

Figure 6 shows the ambient water and CO concentrations as a function of time for a thermally grown oxide sample (inactive) on a thoroughly oxidized stainless-steel heater assembly. These data show that over long times the CO concentration is dependent on the water concentration. However, when the water levels are raised significantly on a short time scale, the CO levels do not immediately respond. In other cases that are not shown, the effect of water addition was inconsistent or showed hysteresis effects. The complications made it impossible to quantitatively determine the role of water in producing the CO.
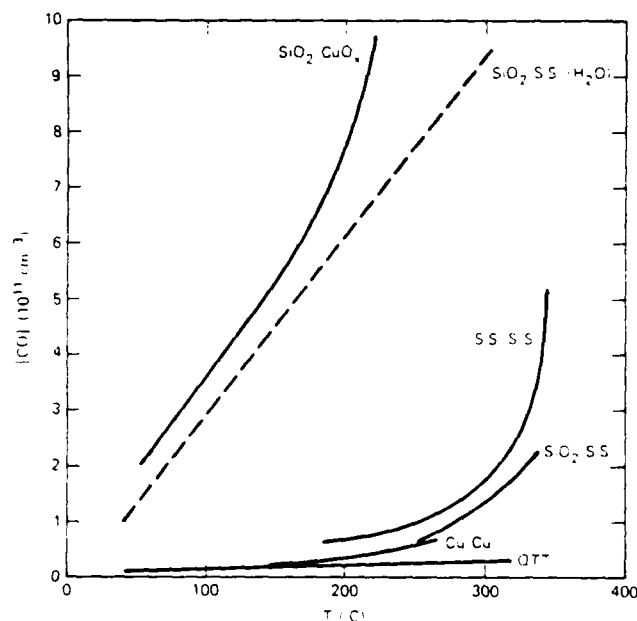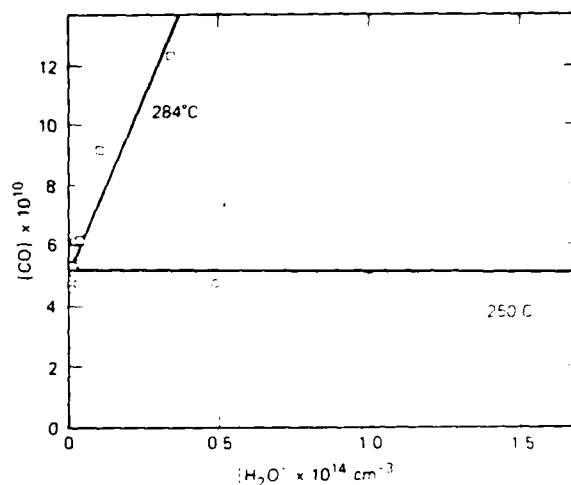

FIG. 4. CO concentration as a function of temperature for various substrates and heater assembly materials. Data taken with a stainless-steel heater with a silica substrate and without a substrate are labeled SiO, SS and SS/SS, respectively. Data taken with a clean copper heater and no substrate are labeled Cu/Cu. Data from an oxidized copper heater with a fused-silica substrate are labeled SiO/CuO. The dashed line, labeled SiO. SS (H₂O), represents data from Selamoglu et al (Ref 11). The curve labeled QTT pertains to a quartz test-tube experiment. The flow rate in all these cases was ~4 × 10¹⁴ molecule s⁻¹. The laser depletion f was ~20% for all cases, except for the dashed curve, where f was between 4% and 14%.
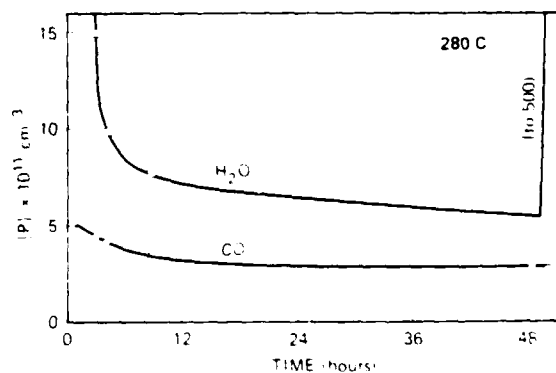

FIG. 6. CO and H₂O concentration as a function of time (in h) for a stainless-steel heater and a thermally grown silicon oxide surface.

The effect of water on the other mass peaks was not investigated as thoroughly. The $m/e = 85$ peak, which is a monitor for SiF_4, was reduced in the presence of water with the oxidized copper disk in the gold-coated heater assembly. This result is consistent with the previous experiments.[11]

The conclusion from these observations is that ambient water vapor is involved in the CF_3 surface reactions that produce CO. These results are consistent with the results of previous experiments[11] and show, moreover, that additional effects (other than water-vapor concentration) influence the way water interacts with CF_3, depending on the surface to which the H_2O is chemisorbed.

D. Surface kinetic data

As discussed in the previous paper,[11] our method generates two kinds of data: (1) the total heterogeneous loss of CF_3 in the VLPΦ cell, and (2) the production of closed-shell, stable reaction products, such as CO.

Figure 7 presents typical data for a stainless-steel reaction vessel with a SiO_2 substrate on a stainless-steel heater assembly, plotted according to Eq. (5). The slope of the reciprocal plot is independent of temperature in the indicated range (400–500 K). Previous work on the absolute magnitude of k_r, as a function of temperature, indicates that its value is temperature independent.[12] We conclude therefore that k_w, the total wall-loss rate constant for CF_3, which is measured to be $0.6 s^{-1}$, must be independent of the temperature of the SiO_2 substrate in the covered range and in our reaction vessel. We interpret this result to mean that the wall loss of CF_3 takes place predominantly on the cold stainless-steel surface of the reaction vessel. In this way, the heterogeneous CF_3 removal rate is not affected by the temperature of the SiO_2 substrate. This interpretation is consistent with the qualitative tests regarding the surface activity of SiO_2 versus stainless steel discussed in the previous sections.

The straight line from the linearized data plot, Eq. (5), is expected to go through the intercept 2. In cases where we have few data or where the data spanned a limited range of the independent variable, we obtained k_r from a forced fit through the theoretical intercept 2. In the example of Fig. 7,
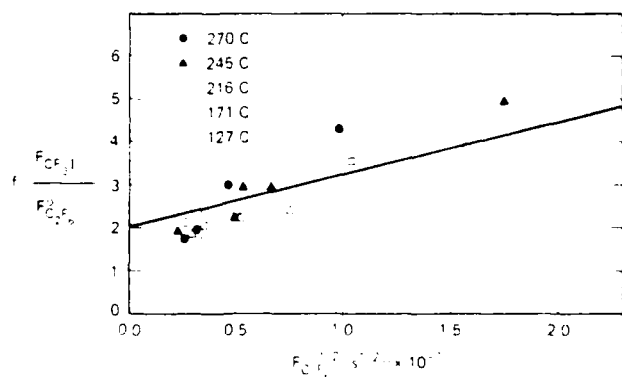
k_w amounts to $1.2 s^{-1}$ when the linear least-squares line (intercept of 1.0) is used, whereas the forced fit results in $k_w = 0.6 s^{-1}$. With the gold coating of the cold walls, k_w dropped to $0.1 s^{-1}$ at room temperature, which is a very low value of k_w for CF_3 free radicals. Thus, gold is less reactive than stainless steel with CF_3 at room temperature.

Figure 8 summarizes our data on k_w for CF_3 with different cell wall material, substrate, and heater assembly combinations. The horizontal line at $k_w = 0.6 s^{-1}$ represents the data analyzed in Fig. 7 for the cell with stainless-steel cold walls. This k_w value corresponds to a CF_3 sticking coefficient on cold stainless steel of $\gamma \sim 6 \times 10^{-5}$. The curve below this, which is labeled SiO_2/SS represents data taken after the cold walls were coated with gold. The horizontal section of this curve represents CF_3 loss on the cold gold-coated walls ($\gamma \sim 1 \times 10^{-5}$). The increasing k_w at higher temperatures represents CF_3 loss on the substrate and heater assembly. Similar k_w curves were found for a gold-plated heater assembly in the cell with gold-coated cold walls. k_w did increase at higher temperatures, indicating that the gold surface had an increased reactivity toward CF_3 at higher temperatures.

Also shown are the values for SiO_2/CuO_x in a cell with gold-coated cold walls, which shows the increased reactivity of the CuO_x surface (heater assembly) toward CF_3. The temperature dependence for the previous results[11] [SiO_2/SS (H_2O)] are also shown for comparison. The nature of the surface obviously has a dramatic effect on k_w, which spans from one to two orders of magnitude at moderate temperatures.

When we plot the yield of CO as a function of the steady-state concentration of CF_3, we obtain a curve showing saturation as shown in Fig. 9. This is because, unlike gas-phase reactions, surface reactions proceed on a finite number of

FIG. 7 Reciprocal plot of CF_3 radical recombination in a stainless-steel vessel with a stainless-steel heating assembly and an SiO_2 substrate at different temperatures. F_{CF_3I} and F'_{CF_3I} are the flow rates of CF_3I into the reactor and C_2F_6 out of the reactor, and f is the fractional decomposition of CF_3I upon IR-laser irradiation.
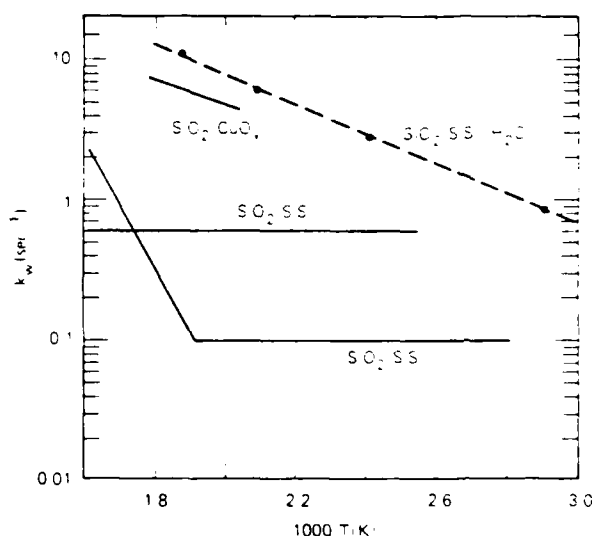
FIG. 8 Wall loss rates k_w as a function of inverse temperature. The solid line labeled SiO_2 SS and constant-with-temperature represents data taken in the stainless-steel cell before gold coating the cold cell walls. The other solid line labeled the same way represents data taken after the gold coating of the cold walls. Also shown are the data from Selamoglu *et al.* (Ref. 11) [dashed line labeled SiO_2/SS(H_2O)] and the data with the oxidized copper-heater assembly (SiO_2 CuO$_x$).

FIG. 9. Yield of CO, the principal surface reaction product of CF₃ with H₂O as a function of the steady-state free radical concentration [CF₃]ss. The reaction took place in the stainless-steel reaction vessel with stainless-steel heater assembly and 2-in.-diam fused-silica substrate heated to 220 °C under H₂O-rich conditions ([H₂O] ~ 3 · 10⁻³ Torr)

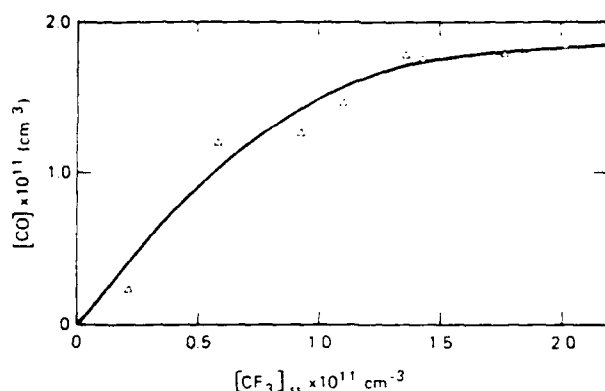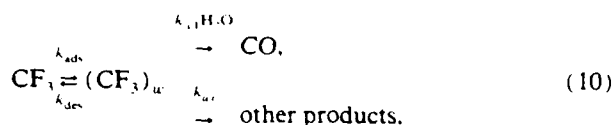sites with a corresponding upper limit of population or decay rate of these reaction sites. Thus, the saturation of the conversation rate is the hallmark of a surface reaction of which Fig. 9 gives an example.

To qualitatively understand such a dependence, we set up a Langmuir–Hinshelwood surface reaction model, such as Eq. (10):

$$CF_3 \underset{k_{des}}{\overset{k_{ads}}{\rightleftharpoons}} (CF_3)_w \underset{k_{w,t}}{\overset{k_{w,H_2O}}{\longrightarrow}} \begin{array}{l} CO, \\ other\ products. \end{array} \qquad (10)$$

where $(CF_3)_w$ is the molecular adsorbate of the gas-phase CF_3. The density of CF_3 is determined by reactions (1)–(3). We assume that H_2O is the majority component on the surface and is always present in excess, so that all surface reactions with water proceed in a pseudo-first-order manner with respect to $(CF_3)_w$. The reaction rate constants for the various reaction paths are $k_{w,i}$, and the sum of $k_{w,i}$ equals the total wall-loss rate constant k_w. In our case, we can replace k_w with $k_{w,i}$ because CO constitutes 90% of the products and thus represents the major loss channel of $(CF_3)_w$. A steady-state analysis of $(CF_3)_w$ leads to the following expression [Eq. (11)] for the unimolecular rate constant for the disappearance of gas-phase CF_3:

$$k = \frac{k_w k_{ads}}{k_w + k_{des}} A\ [(CF_3)_w]\ (1 - \theta), \qquad (11)$$

where A is the surface area. θ is the surface coverage of $(CF_3)_w$:

$$\theta = [(CF_3)_w]/[(CF_3)_w^x], \qquad (12)$$

where $[(CF_3)_w^x]$ is the surface density that would exist at an infinite density of gas-phase CF_3, that is, at saturation.

The primary observable in a flow reactor is the flow of a given species out of the reactor. For CO, the flow rate equals its production rate and assumes the form of Eq. (13):

$$R''_{CO} = k_e^{CO}[CO]$$

$$= [(CF_3)_w^x]\ k_w\ \theta\beta. \qquad (13)$$

where R''_{CO} is the production rate of CO and β is the branch-

ing ratio that relates the total CF₃ loss rate to the CO production rate, which we assume is near unity. Equation (13) reveals the important fact that [CO] is proportional to θ, which is itself a function of CF_3. The functional dependence of [CO] on [CF₃] reveals the dependence of θ on [CF₃]. The saturation of CO production, seen in Fig. 9, results when θ goes to unity.

We find this method of measuring θ for a free radical interesting, in that it provides a thermodynamic parameter that cannot be easily measured by other than kinetic methods in view of the transient nature of the reactant.

E. Quartz test tube

The final experiment in this series of qualitative tests involved the quartz test tube. Figure 4 shows the CO concentration in the reactor as a function of temperature (labeled QTT) for a CF₃I flow rate of 3.5×10^{15} molecules s⁻¹ and 20% depletion of CF₃I by the CO₂ laser. The hot surface area in this experiment was 130 cm² compared with 60 cm² total surface area of the heater assembly. There was no signal at the $m/e = 47$ and 85 peaks, and the signal at $m/e = 44$ was very small. The exposed quartz surface of the test tube had been etched with HF, resulting in a seemingly smooth surface, although a significant amount of quartz had been removed. A roughened quartz surface was also used to determine whether this treatment would promote the surface reactions. The quartz was bead blasted and then etched in diluted HF. This process increased the production of CO only slightly, and no increases in the other products were observed. In an experiment where an extra flow of water was added $(1 \times 10^{16}$ molecules s⁻¹), the CO concentration in the reactor did not increase. The wall loss rates were comparable to those observed with the metal-heater assembly shown in Fig. 7; the low-temperature rate constant was ~0.1 s⁻¹, and it increased at 250 °C.

We conclude from this test that quartz is less reactive than metals and does not act as a catalyst for the reaction of CF₃ with water vapor. This conclusion is consistent with the conclusion reached for fused silica or thermally grown oxide on silicon on the gold-plated heater assembly, despite the differences in surface morphology and composition of these silicon oxide surfaces. An upper limit on the etching efficiency of CF₃ [Eq. (9)] can be determined if we assume that the noise level in the signal of $m/e = 85$ equals the maximum signal from the etching product SiF₄. This gives an upper limit on the density of SiF₄ in the reactor of 2×10^9 cm⁻³. For our typical conditions (250 °C, $F_{CF_3I}^x = 4 \times 10^{15}$ s⁻¹ and $f = 0.20$), the steady-state density of CF₃ is ~4×10^{11} cm⁻³. With these densities and the escape and wall-collision rate constants, we derive an upper limit of 3×10^{-6} for the etching efficiency of CF₃.

V. CONCLUSIONS

The qualitative conclusions of these tests are that CF₃ reacts readily on metal surfaces with adsorbed water. The oxidized copper surface was found to be the most reactive. The other metal surfaces—stainless steel, copper, and gold—react with the CF₃ at a slower rate, and within the

day-to-day variations of our reactor, these materials react at roughly the same rates at these elevated temperatures (150–250 °C). We observe that gold is less reactive at room temperature, and it is a better material to use for the heater assembly because it will not oxidize. The quartz and silica surfaces were seen to be unreactive with CF_3; no spontaneous etching was observed. The simple rule that a CF_x species is responsible for SiO_2 etching is still valid, but that CF_x species is not CF_3; at least not in the absence of the radiation and charged particles that exist in discharges.

The data are consistent with previous experiments in this laboratory. However, the new data require a reinterpretation of the earlier data in two respects. Previously, we reported that all the surface reactions of CF_3 occurred on the silica disk and not on the stainless-steel heater assembly that was used at the time. This conclusion is at variance with the present results; the reactions in the earlier experiment with the high background of water apparently occurred on the metal surface, and the control experiments that were used were not valid or were incomplete. The other disagreement with the conclusions reached in that paper is the identification of SiF_4 as an etching product of SiO_2. SiF_4 now appears to be due to a silicon impurity in the cell. The other data in that paper are useful and correct with the understanding that the reactions were occurring on the metal.

The isotopic analog experiments showed that adsorbed water is involved in the production of the oxygen- and hydrogen-containing products. The data are useful because they point out the potential importance of wall reactions occurring in various dry-processing reactors. Water adsorbed on metal surfaces may significantly consume reactive species that might otherwise be used for the desired process.

ACKNOWLEDGMENT

[a] Postdoctoral Fellow.

[1] D. L. Flamm and V. M. Donnelly, Plasma Chem. Plasma Proc. 1, 317 (1981).

[2] J. A. Mucha and D. W. Hess, in *Introduction to Microlithography*, ACS Symp. Ser. No. 219, edited by L. F. Thompson, C. G. Wilson, and M. J. Bowden (American Chemical Society, Washington, DC, 1983), Chap. 5.

[3] G. L. Loper and M. D. Tabat, Appl. Phys. Lett. 46, 654 (1985).

[4] G. L. Loper and M. D. Tabat, in *Proceedings of the International Conference on Lasers '83*, edited by R. C. Powell (STS, McLean, VA, 1983).

[5] J. H. Brannon, J. Phys. Chem. 90, 1784 (1986).

[6] B. Roop, S. Joyce, J. C. Shultz, and J. I. Steinfeld, J. Chem. Phys. 83, 6012 (1985).

[7] J. W. Thoman, Jr., K. Suzuki, S. H. Kable, and J. I. Steinfeld, J. Appl. Phys. 60, 2775 (1986).

[8] S. C. McNevin and G. E. Becker, J. Vac. Sci. Technol. B 2, 27 (1984).

[9] D. L. Smith and P. G. Saviano, J. Vac. Sci. Technol. 21, 768 (1982).

[10] S. Tachi and S. Okudaira, J. Vac. Sci. Technol. B 4, 459 (1986).

[11] N. Selamoglu, M. J. Rossi, and D. M. Golden, J. Chem. Phys. 84, 2400 (1986).

[12] N. Selamoglu, M. J. Rossi, and D. M. Golden, Chem. Phys. Lett. 124, 68 (1986).

[13] M. J. Rossi and D. M. Golden, Int. J. Chem. Kinet. 11, 775 (1979).

[14] M. J. Rossi, J. R. Barker, and D. M. Golden, J. Chem. Phys. 71, 3722 (1979).

[15] F. Yamada, I. R. Slagle, and D. Gutman, Chem. Phys. Lett. 83, 409 (1981).

[16] J. A. McCaulley, S. M. Anderson, J. B. Jeffries, and F. Kaufman, Chem. Phys. Lett. 115, 180 (1985).

Appendix B

SUMMARY ABSTRACT: SPONTANEOUS THERMAL ETCHING
OF SILICON BY CF_3 RADICALS

Summary Abstract: Spontaneous thermal etching of silicon by CF_3 radicals
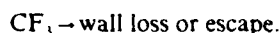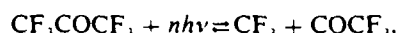
Robert M. Robertson, David M. Golden, and Michel J. Rossi

Department of Chemical Kinetics, SRI International, Menlo Park, California 94025-6448

In order to understand the complex chemistry in commercial etching chambers, it is necessary to understand the surface reactions of the individual species that are present. We have studied the reactions of CF_3 on silicon surfaces in a very low-pressure photolysis (VLPΦ) cell. The radicals are produced by IR photolysis of hexafluoroacetone (HFA). Mass spectrometry and resonance-enhanced multiphoton ionization (REMPI) are used to determine quantitative information about the kinetics of the CF_3 radicals. We have measured the pressure and temperature dependence of the formation of SiF_4, the product of the etching reaction. This information is combined with the REMPI measurement of the absolute density of CF_3 in the reactor to derive the reaction probability of the radical etching the silicon as a function of temperature. We found an inhibition effect on the etch rate that is due to the buildup of a carbon layer on the silicon.

These are flowing-gas experiments in which HFA ($P < 5 \times 10^{-3}$ Torr) is partially decomposed by a pulsed CO_2 laser [10 Hz, 1 J cm^{-2}, 10 R(12) line] to form CF_3. The cell is a stainless-steel six-way cross. The four side arms have windows for the crossed lasers. The bottom arm has an escape aperature (3-mm diam), which controls the cell escape rate constant and produces an effusive beam for the mass spectrometer. The top arm houses the hot sample surface which is pressed down on a circular knife edge (1.68-in.-diam opening). The heater and thermocouples are located on the back side of the sample and are pumped separately. The knife edge and its supporting flange are water cooled, so that only the hot sample surface is exposed to the reactive gases. The samples were 2-in.-diam, n-type silicon wafers with (100) orientation. The surface was etched with molecular fluorine prior to the experiments with CF_3

The primary reactions for IR photolysis of HFA are

$$CF_3COCF_3 + nh\nu \rightleftharpoons CF_3 + COCF_3,$$

$$CF_3 + CF_3 \rightarrow C_2F_6,$$

$$CF_3 \rightarrow \text{wall loss or escape.}$$

In contrast to the results of Hackett, Willis, and Gauthier,[1] we obtain one CF_3 for each HFA photolyzed. The COCF$_3$ radical does not decompose, and it is less reactive with the hot Si surface than CF_3 We have observed the recombination of CF_3 and COCF$_3$ at the upper end of our pressure range.

The mass spectrometer monitors stable species that effuse from the cell (HFA, C_2F_6, and SiF_4). The SiF_4 production was proportional to the initial production rate of CF_3 and had an activation energy of $\sim$8.5 kcal mol^{-1}. The SiF_4 rate of formation decreases proportionally to the time the surface is exposed to the HFA with the CO_2 laser on. The effect is

due to a buildup of carbon on the surface because fluorocarbon species are produced when the inhibited surface is etched with F_2. Experiments with CF_3I as the precursor gas yielded similar results for SiF_4 formation and surface inhibition. We conclude that the etching and inhibition effect are primarily caused by CF_3 since it is the only species that is common to both precursors.

REMPI is used to determine the reaction rates and the absolute density of CF_3 in the reactor. The ions and electrons produced by the focused dye laser are collected on biased wire electrodes inside the reactor. The signal difference with the laser on and off was due to CF_3 showing the expected wavelength dependence.[2] This difference signal was calibrated in terms of an absolute density by measuring how much CF_3 is produced per CO_2 laser shot; this is measured by monitoring the extent of decomposition of the HFA with the mass spectrometer. The average density between two CO_2 laser pulses for our typical conditions was 4×10^{11} cm^{-3}. These data enable us to determine the relative loss rates of CF_3 to form C_2F_6 (51%), escape from the cell (12%), or be lost on hot and cold walls (37%). The CF_3 density did not change significantly as the silicon surface temperature was raised to 450 °C, so the loss on the hot surface was a minor loss channel under all of our conditions. With this set of kinetic parameters, we are able to use an analytical expression to determine the CF_3 density under other conditions.

The reaction probability for the etching of silicon by CF_3 is

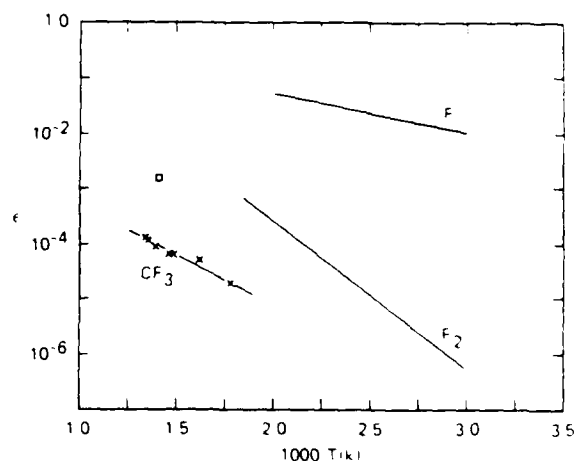$$\epsilon = \frac{F(SiF_4)}{\frac{1}{4}\bar{v}[CF_3]}\frac{4}{3}.$$

$F(SiF_4)$ is the flow of SiF_4 out of the reactor, and $\bar{v}$ is the thermal velocity of CF_3. In Fig. 1, the ×'s represent data for a surface that had been exposed to HFA and the CO_2 laser for a long period (90 min), such that the etch rate was inhibited. The reaction probability for a surface that had been etched with F_2 immediately prior to etching with CF_3 is represented by an open box in Fig. 1. The etch probability for CF_3 on an inhibited surface is much smaller than for F_2 molecules,[3] whereas the etch probability on a fluorinated surface (etched with F_2) is only slightly less than for F_2. The reaction probability of F atoms[4] is much higher than for CF_3.

[1] P. A. Hackett, C. Willis, and M. Gauthier, J. Chem. Phys. 71, 2682 (1979)
[2] M. T. Duignan, J. W. Hudgens, and J. R. Wyatt, J. Phys. Chem 86, 4156 (1982).
[3] N. Selamoglu, J. A. Mucha, D. L. Flamm, and D. E. Ibbotson, J Appl Phys. 62, 1049 (1987).
[4] M. J. Vasile and F. A. Stevie, J. Appl. Phys. 53, 3799 (1982).

Appendix C

IN-SITU RADICAL DETECTION UNDER VERY LOW PRESSURE PHOTOLYSIS
CONDITIONS USING RESONANCE-ENHANCED MULTIPHOTON IONIZATION.
KINETICS OF CF_3 RADICALS PRODUCED FROM IR MULTIPHOTON DISSOCIATION
OF HEXAFLUOROACETONE

In Situ Radical Detection under Very Low Pressure Photolysis Conditions Using Resonance-Enhanced Multiphoton Ionization. Kinetics of CF$_3$ Radicals Produced from IR Multiphoton Dissociation of Hexafluoroacetone

Robert M. Robertson,[†] David M. Golden, and Michel J. Rossi[*]

Department of Chemical Kinetics, Chemical Physics Laboratory, SRI International, Menlo Park, California 94025 (Received: January 7, 1988; In Final Form: May 17, 1988)

Resonance-enhanced multiphoton ionization (REMPI) and mass spectrometry have been used to measure the kinetics of CF$_3$ radicals inside of a very low pressure photolysis (VLPΦ) cell. Infrared multiphoton dissociation (IRMPD) of hexafluoroacetone (HFA) is used to generate the radicals according to CF$_3$COCF$_3 \rightarrow$ CF$_3$ + CF$_3$CO. REMPI spectra of vibrationally hot and thermalized CF$_3$ radicals are presented. The absolute density of CF$_3$ in the reactor is determined from the REMPI signal by using mass spectral data. This puts the calibration on the absolute basis necessary to treat competing unimolecular and bimolecular reactions of CF$_3$ free radical. Measuring the CF$_3$ density as a function of time between pulses of the IR laser and of HFA flow rate allows direct determination of the first- and second-order loss rates for CF$_3$. The CF$_3$CO radical is stable under our conditions and engages in recombination back to HFA at higher radical densities.

Introduction

We have used a technique that we have come to call VLPΦ (very low-pressure photolysis) to measure rate constants for radical–radical[1] reactions or fast radical–molecule[2] processes. This Knudsen cell based experiment involves making radicals by photolysis with either an excimer laser or an infrared laser. The initial radical production rates are known from the extent of photolysis of the precursor, and products of the above reaction types are monitored by modulated molecular-beam mass spectrometry as they effuse from the reactor. The quantitative relationships between the observables and the rate constant of interest are easily derived by using the steady-state assumption and have been presented many times. In the particular case of radical–radical reactions, eq 1 describes the reciprocal relationship of the observables with the kinetic parameters of interest:

$$\frac{R^i_R}{R^o_{R_2}} = 2\frac{k_d + k_r}{k_r} + \frac{k_1}{k_r^{1/2}} \frac{1}{R^o_{R_2}{}^{1/2}} \quad (1)$$

The precursor for this example is a molecule of the type RX. The kinetic parameters of interest are k_1 (the total first-order loss rate constant), k_r (the recombination rate constant for the free radical R leading to R$_2$), and k_d (the rate constant for disproportionation). The R terms in this equation are the specific flow rates of the respective species (subscript) into or out of (superscript i and o, respectively) the Knudsen cell.

We have recently applied this technique to the measurement of the rate constant for the recombination of CF$_3$ radicals[1] produced from the photolysis of CF$_3$I by either IRMPD or UV single-photon dissociation. In this case, the disproportionation reaction is unimportant, so eq 1 reduces to

$$\frac{R^i_R}{R^o_{R_2}} = 2 + \frac{k_1}{k_r^{1/2}} \frac{1}{R^o_{R_2}{}^{1/2}} \quad (2)$$

If the simple mechanism involving only radical combination and escape is indeed correct for our experimental conditions, it is a relatively simple matter to calculate the steady-state free radical density in the reactor. In the Appendix, it is demonstrated that the steady-state assumption is valid over the range of experimental conditions used in this set of experiments.

In the present paper, we discuss the kinetics of CF$_3$ radicals produced by IRMPD of hexafluoroacetone (HFA) in a VLPΦ apparatus that combined the mass spectrometric sampling technique with real time in situ detection of the radicals by resonance-enhanced multiphoton ionization (REMPI). REMPI has

TABLE I: Reactions in the IRMPD of HFA and CF$_3$I

no.	reaction	symbol
1	CF$_3$COCF$_3$ + $nh\nu \rightarrow$ CF$_3$ + COCF$_3$	
2	COCF$_3 \rightarrow$ CO + CF$_3$	
3	CF$_3$ + COCF$_3 \rightarrow$ CF$_3$COCF$_3$	k'_r
4	CF$_3$ + CF$_3 \rightarrow$ C$_2$F$_6$	k_r
5	CF$_3$ + CF$_3$COCF$_3 \rightarrow$ (CF$_3$)$_3$CO or (CF$_3$)$_2$COCF$_3$	
6	CF$_3$ + CF$_3$COCF$_3 \rightarrow$ CF$_4$ + CF$_2$COCF$_3$	
7	CF$_3 \rightarrow$ escape	k_e
8	CF$_3 \rightarrow$ wall loss	k_w
9	CF$_3$I + $nh\nu \rightarrow$ CF$_3$ + I	
10	CF$_3$ + I$_2 \rightarrow$ CF$_3$I + I	

been studied extensively to understand the process itself, as well as the spectroscopy of atoms and molecules. The selectivity and sensitivity of REMPI suggest it could also be a valuable diagnostic in kinetic systems. To keep the reaction vessel as simple as possible, we use a simple diode detector to collect the REMPI signal rather than doing mass-selection detection and rely on the selectivity of the resonant molecular transition to determine the origin of the ions produced. In the present work, the use of the REMPI technique in concert with VLPΦ allows us to quantify the density and kinetics of CF$_3$ radicals produced from the IRMPD of HFA.

The present work provides the underpinning for a mechanistic study of radical–surface reactions using the VLPΦ/REMPI technique. One goal is the quantitative study of the kinetics of the etching of silicon by CF$_3$. Such VLPΦ/REMPI experiments have been carried out and will be reported elsewhere.[3] In initial experiments employing combined mass spectrometric/REMPI detection, we used CF$_3$I and CF$_3$Br as sources of CF$_3$. Large background signals from the ionization of these precursor species prevented the detection of a REMPI signal due to CF$_3$ radicals. We were, however, able to detect interesting REMPI spectra of I and Br atoms that will also be reported elsewhere.[4] We then turned to the IRMPD of HFA as a source of CF$_3$ radicals. With HFA, the background problem of nonresonant precursor ionization was mitigated, but the photochemistry and kinetics of HFA proved to be more complicated than expected. Indeed, a different photochemical mechanism seems to obtain under our conditions than previously reported.

(1) Selamoglu, N.; Rossi, M. J.; Golden, D. M. *Chem. Phys. Lett.* **1986**, *124*, 68.

(2) Rossi, M. J.; Barker, J. R.; Golden, D. M. *J. Chem. Phys.* **1979**, *71*, 3722.

(3) Robertson, R. M.; Golden, D. M.; Rossi, M. J. *J. Vac. Sci. Technol., A* **1988**, *6*, 1407.

(4) Robertson, R. M.; Golden, D. M.; Rossi, M. J. *J. Chem. Phys.*, in press.

[*] To whom correspondence should be addressed.
[†] Postdoctoral Research Associate.

Background

The IRMPD[5-8] and UV photolysis[9-12] of HFA have been studied. The initial mechanism for both types of photolysis is a simple bond-breaking process, reaction 1 in Table I, followed often by secondary photolysis or thermolysis of the perfluoroacetyl radical, reaction 2. The decomposition of COCF$_3$ has been argued to be very fast under the experimental conditions employed, so that two CF$_3$ radicals are always generated for each HFA molecule decomposed. The kinetics of the CF$_3$ radical is reportedly dominated by reaction 4 under conditions of rapid decay of CF$_3$CO, thus preventing the reaction of CF$_3$ and CF$_3$CO back to HFA, reaction 3. The CF$_3$ recombination reaction has been studied over a wide temperature range by using VLPΦ[1] and other techniques.

At higher densities of HFA other possible reactions of the CF$_3$ radical are given by reactions 5 and 6. The addition of CF$_3$ to HFA, reaction 5, can proceed in two modes. In the first mode, CF$_3$ attacks the carbonyl carbon, forming an oxygen-centered radical, and in the second, CF$_3$ attacks the oxygen in HFA leading to a perfluoroether radical with the radical center on the carbon atom. Reactions 5 and 6 are thought to have small activation barriers[5,10,13] and may be important in some experiments. However, the importance of this secondary chemistry is minimized in our low-pressure cell in view of the fact that these reactions compete against radical–radical reactions with essentially no activating energy. Only in our highest pressure situations (small exit aperture and high input flow rates of HFA) do we expect some interference from reaction 5.

The reactions of the COCF$_3$ radical have been explored in experiments with a different precursor, CF$_3$COH.[14,15] These papers point out that there is a barrier for unimolecular decomposition of the radical and that the recombination with CF$_3$, reaction 3, apparently has no barrier.

Experimental Section

VLPΦ Reactor. the reactor has been described elsewhere.[16] but in the interest of completeness, we present a brief overview at this point. The main body of the cell is comprised of a 2^3/$_4$-in. stainless-steel corner cube. The inside of this corner cube as well as the extension tubes are coated with a thin coat of gold deposited by vacuum evaporation. Four side arms hold the windows for the two lasers. The top arm holds a large conductance valve that provides for initial rapid pumpdown. A 4-in.-long extension tube is attached to the bottom face of the corner cube. This extension tube normally holds a hot sample surface fixed against a heated copper block, but for the present experiments these parts were removed. At the bottom end of this extension tube an interchangeable aperture is located. It controls the escape rate out of the Knudsen cell and forms an effusive molecular beam that is skimmed and sent into the ionization region (electron impact) of the mass spectrometer.

The characteristic parameters of the Knudsen cell are as follows: the volume of the cell is 460 cm^3, the surface area is 620 cm^2, the escape rate constant for a 3-mm-diameter aperture for a species of molecular weight M, at temperature T (K), is $k_e^M = 0.323 \cdot$

$(T/M)^{1/2}$ s^{-1}, and the gas–wall collision frequency is $\omega = 4920 \cdot (T/M)^{1/2}$ s^{-1}. In some of the experiments the escape rate constant was changed to a value one-fourth of the above value by replacing the disk with the exit hole by another one whose center hole diameter was half as large (1.5 mm). When the 3-mm aperture is in place, we refer to the large-aperture reactor, and with the 1.5-mm hole employed, we refer to the small-aperture cell. The precursor gas is introduced into the cell through capillary inlets or a fine stainless-steel metering valve from a standard vacuum line.

The ions and electrons from the REMPI process are collected on biased wire electrodes (± 90 V) inside the cell. The ion and electron currents are amplified and then fed into a differential amplifier[17] to be added. This signal is then monitored with a boxcar averager. The details of the ion and electron collection are discussed elsewhere.[4]

The multiphoton decomposition of HFA was performed with a CO$_2$ laser tuned to the R(12) line of the 10.6-μm band. The laser was collimated to obtain a 1-cm^2 beam area and was reflected back through the cell to obtain a higher fluence. The repetition rate of the laser was 10 or 20 Hz, and the pulse energy was 1 J per pulse. The multiphoton ionization occurred by using a visible dye laser pumped by a XeF excimer laser at 351 nm. Focusing was done with a 50-mm lens. The maximum pulse energy was 12 mJ; however, the data were typically taken with pulse energies of 2–6 mJ to optimize the signal/noise and signal/background ratios. The delay between the two lasers was controlled by a digital delay generator. The jitter between the two lasers was a fraction of a microsecond, small on the time scales of interest. The average dye laser power was measured with a Scientech power meter and was held constant within a few percent by very slight adjustments of the excimer laser high-voltage power supply. Due to the strong intensity and fluence dependence of the MPI and MPD processes, respectively, the REMPI signal required long integration time constants.

REMPI Spectra of CF$_3$. In a pulsed photolysis system, the density and internal energy of the radicals will vary in time after being produced. The REMPI signal from these radicals will similarly depend on the delay time of the probe laser. In later sections of this paper, we will examine the signal dependence on delay time to determine the kinetics of the CF$_3$ radical. In this section, we present the REMPI spectra at two characteristic delay times: Immediately after being formed (a few microseconds delay time) the radicals are located in the photolysis-beam volume and contain the internal energy with which they are formed. After a short delay time (~ 2 ms), the radicals have diffused throughout the cell and have thermalized through wall collisions. Since the details of the REMPI spectra and power dependence are peripheral to the subject of this paper, we restrict ourselves to a brief discussion of these subjects.

The REMPI spectrum of CF$_3$ has been measured and analyzed in detail by Duignan et al.[18] Their sources of the CF$_3$ were pyrolysis of CF$_3$I and IRMPD of CF$_3$I, CF$_3$Br, and HFA. The focus of their dye laser was located in the ionization region of a quadrupole mass spectrometer, so that the ions generated could be mass analyzed. They concluded that the ionization of CF$_3$ was a [3 + 1] photon process and that the observed band-head progression was due to the out-of-plane bending of the resonant Rydberg state. We will use the reported REMPI spectra to determine the extent to which our total ionization signal is due to CF$_3$ radical.

Examples of our REMPI spectra are shown in Figure 1 for the wavelength range 450–475 nm (coumarin 460 dye) and in Figure 2 for the range 465–485 nm (coumarin 480 dye). Figure 1a presents the REMPI signal when only the dye laser was firing, that is, when no free radicals were generated by the IR laser. This background signal resulted from multiphoton processes in HFA,

(5) Hackett, P. A.; Willis, C.; Gauthier, M. *J. Chem. Phys.* **1979**, *71*, 2682.

(6) Drouin, M.; Hackett, P. A.; Willis, C.; Gauthier, M. *Can. J. Chem.* **1979**, *57*, 3053.

(7) Fuss, W.; Kompa, K. L.; Tablas, F. M. G. *J. Chem. Soc., Faraday Discuss.* **1979**, *67*, 180.

(8) Avatkov, O. N.; Aslanidi, E. B.; Bakhtadze, A. B.; Zainullin, R. I.; Turishchev, Yu. S. *Sov. J. Quantum Electron.* **1979**, *9*, 232.

(9) Perkins, G. G. A.; Austin, E. R.; Lampe, F. W. *J. Chem. Phys.* **1978**, *68*, 4357.

(10) Wu, E.-C.; Clark, R. R.; Tang, Y.-N. *Can. J. Chem.* **1978**, *56*, 1989.

(11) Ayscoughs, P. B.; Steacie, E. W. R. *Proc. R. Soc. London, A* **1956**, *234*, 476.

(12) Whytock, D. A.; Kutschke, K. O. *Proc. Roy. Soc. London, A* **1968**, *306*, 503.

(13) Gordon, A. S. *J. Chem. Phys.* **1962**, *36*, 1330.

(14) Amphlett, J. C.; Whittle, E. *Trans. Faraday Soc.* **1967**, *63*, 80.

(15) Kerr, J. A.; Wright, J. P. *J. Chem. Soc., Faraday Trans. I* **1985**, *81*, 1471.

(16) Robertson, R. M.; Rossi, M. J.; Golden, D. M. *J. Vac. Sci. Technol. A* **1987**, *5*, 3351.

(17) Adams, T. E.; Morrison, R. J. S.; Grant, E. R. *Rev. Sci. Instrum.* **1980**, *51*, 141.

(18) Duignan, M. T.; Hudgens, J. W.; Wyatt, J. R. *J. Phys. Chem.* **1982**, *86*, 4156.
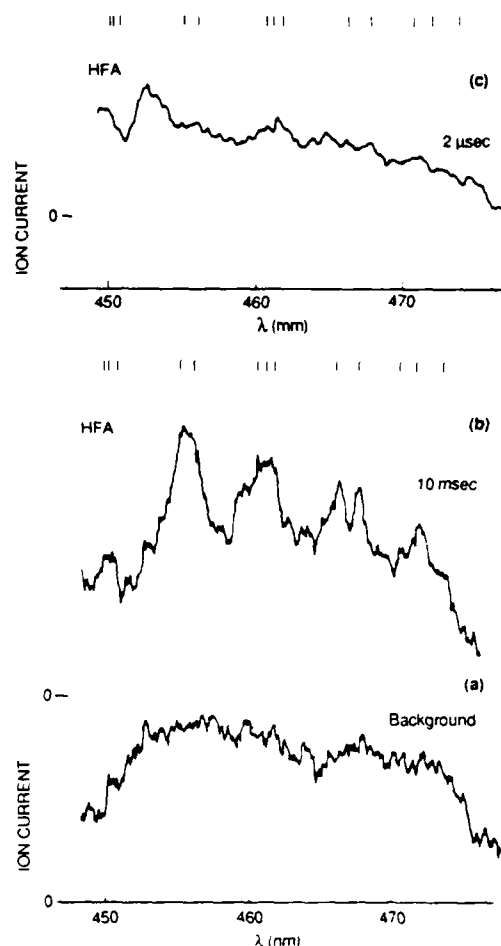
Figure 1. REMPI signal versus wavelength (coumarin 460 dye): (a) photolysis laser blocked (5 mV/div scale); (b) 10-ms delay (5 mV/div scale); (c) 2-μs delay (50 mV/div scale). The expected line positions[17] for the three-photon resonances of CF_3 are indicated at the top of each panel. The flow of HFA was 2.5×10^{16} s^{-1}, and the depletion was ~0.20. The dye laser pulse energy was 8 mJ at the center of the wavelength range, falling to 7 mJ at the ends. The repetition rate was 13 Hz. The feature at 455 nm was used to study the kinetics.

either ionization of HFA leading to the parent ion or the ionization of fragments brought about by visible-photon decomposition of HFA by the dye laser. Figure 1b presents the ionization signal with the CO_2 laser running at 13 Hz and the dye laser pulse following the CO_2 laser pulse by a fixed-time delay of 10 ms. This signal represents the superposition of the HFA background spectrum and the REMPI spectrum of thermalized CF_3. After subtraction of the background spectrum from the total signal spectrum, we obtain a spectral signature of CF_3 that matches the lines reported for REMPI of CF_3. The expected line positions are shown as vertical bars in Figure 1 and 2.

The delay time between the dye laser and the IR-photodissociation pulse was long enough for the radicals to have undergone many wall collisions and become thermalized. CF_3 radicals undergo approximately 10 collisions with the walls of the reaction vessel every millisecond they spend inside the cell. In Figure 1c, we present a spectrum taken with the CO_2 laser on and with a delay of only 2 μs for the probing dye laser. The larger intensity of the REMPI spectrum is due to the CF_3 radicals still being concentrated in the photolysis beam volume. The background contribution of the HFA REMPI signal is small, and the signal is primarily due to "hot" CF_3. Figure 1c shows diffuse spectra with minimum structure, which we take as a characteristics of vibrationally hot radicals.

The power dependences of the REMPI signals were not studied in detail; however, two observations are worth noting. The background signal (at 455 nm) from HFA alone increased as the
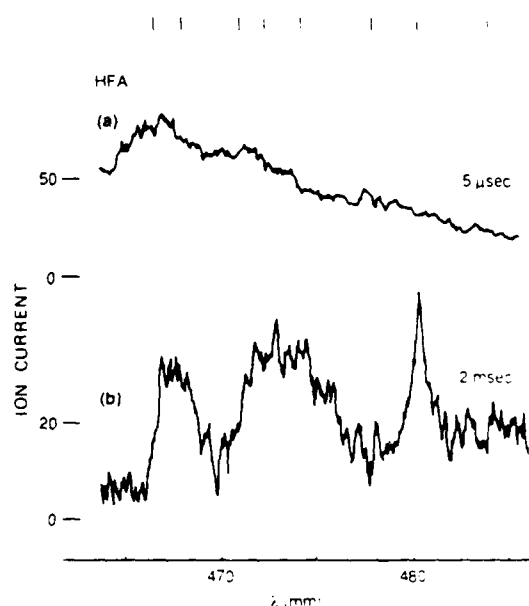

Figure 2. REMPI signal versus wavelength (coumarin 480 dye) (a) 5-μs delay (50 mV/div scale); (b) 2-ms delay (20 mV/div scale). The signal at 2-ms delay time was noisy, so that some of the apparent features may not be real. The expected line positions[17] for the three-photon resonances of CF_3 are indicated at the top of the figure. The flow of HFA was ~6 $\times 10^{16}$ s^{-1}, and $f = 0.20$. The dye pulse energy was 6 mJ in the center of the wavelength range, and the repetition rate was 13 Hz.

intensity to the fourth power, and the signal due to CF_3 (at 455 nm) increased as the intensity to the third power for both short and long delay times.

The spectra for short and long delay times are shown in Figure 2 for the higher wavelength range. Again we see that the characteristic lines are diffuse for the short delay time. The broadening of the REMPI signal caused by the IRMPD formation of excited radicals was also observed by Duignan et al.[18] for CF_3 and by Rockney and Grant[19] for NO_2 (from CH_3NO_2). In the VLPΦ reactor, it is possible to do quantitative experiments on the relaxation of hot polyatomic species.

In the kinetics experiments below, the wavelength of the dye laser will be set at 455 nm, one of the strong features in the CF_3 spectra. REMPI signals in the rest of the paper will refer to that part of the total signal that is due to CF_3, the subtraction of the background signal from HFA having already been done. Also, in the rest of the paper, we will be discussing only REMPI signals with delay times of 2 ms or longer, so we will only be concerned with thermalized radicals with uniform densities throughout the cell. We assert that neither the initial high concentration nor vibrational excitation can significantly influence chemical reaction rates because these effects disappear on a time scale that is short compared to expected reaction lifetimes.

Results and Discussion

The strategy of this work is to study kinetics by combining mass spectrometry (standard VLPΦ) and REMPI diagnostics. Each method provides limited information that taken together provide a more complete picture of the kinetics.

The mass spectrometry provides information on stable species that effuse from the reactor. However, because the residence time of the molecules in the reactor is typically 1–2 s, a time that is long compared to the period of the photolysis laser, the mass spectrometer measurements correspond to steady-state conditions effectively measuring average quantities. We do not observe the HFA decomposition for a single laser pulse but instead measure the net loss of HFA averaged over many pulses. This averaging can obscure important steps in the reaction mechanism and make it difficult or impossible to derive quantitative kinetic parameters.

(19) Rockney, B. H., Grant, E. R. *Chem. Phys. Lett.* **1981**, *79*, 15

Kinetics of CF$_3$ Radicals

The Journal of Physical Chemistry. Vol. 92, No. 19, 1988 **5341**

The REMPI diagnostic, on the other hand, can provide information on the variation in radical density in the cell between laser pulses. The good time resolution of these data provides better kinetic information, though data collection and calibration are more difficult than with the mass spectrometer, and only a few species are observable (only one species in our case).

In the following sections we will present first the mass spectrometry results, and then the REMPI results. It will be seen that the mass spectrometry results are essential for the understanding of the REMPI experiments and that indeed the REMPI results confirm the mechanism assumed in the analysis of the mass spectrometry experiments.

Mass Spectrometry. The stable species that are of primary interest in the kinetic study are HFA and C$_2$F$_6$, both of which can be monitored with good sensitivity by mass spectrometry. HFA was monitored at m/e 147 corresponding to CF$_3$COCF$_2$$^+$, and C$_2F_6$ at 119 corresponding to C$_2$F$_5$$^+$. Upon IRMPD, the signal at 147 decreased and from this decrease the depletion, f, was determined. Similarly, the signal at 119 increased signaling the formation of C$_2$F$_6$, and it was calibrated by using an authentic sample to obtain the absolute rate of formation of C$_2$F$_6$. Under IRMPD conditions, some of the lower masses that noticeably increased included m/e 12, 19, 28, 47, and 66, indicating that some C-, F-, and O-containing species were contributing signal to these mass peaks. Because these changes occur at lower mass, we are not able to identify the parent species. They may include CO, COF$_2$, CF$_4$, CF$_3$OF, and even the radical CF$_3$CO that eluded our attempts of identification by mass spectrometry.

To determine quantitative kinetic parameters from the mass spectrometry experiments, we must do a steady-state analysis of the relevant reactions in Table I. Reactions 1, 3, 4, 7, and 8 are included in this analysis. Reaction 2 will be shown below to be unimportant for our conditions, and reaction 3 will be shown to be important at the high end of our pressure range. The steady-state analysis is done in the same way as was done to derive eq 1 and 2, except that the back reaction to form HFA must be included. The resulting reciprocal relation is given in

$$\frac{fR^1{}_{HFA}}{R^0{}_{C_2F_6}} = 2 + \frac{k_e + k_w}{k_r^{1/2}R^0{}_{C_2F_6}{}^{1/2}} \qquad (3)$$

The meaning of the symbols has been discussed in the Introduction. f is the net steady-state depletion of the HFA:

$$f = (R^1{}_{HFA} - R^0{}_{HFA})/R^1{}_{HFA} \qquad (4)$$

This experimental parameter reflects the difference between the rates of reactions 1 and 3. In the steady-state analysis to derive the reciprocal equation it is not relevant how much of the initially decomposed HFA is re-formed by reaction 3. We will discuss below the experimental evidence for the occurrence of this reaction.

Reciprocal Plots. Equation 3 demonstrates the reciprocal relation between the observables C$_2$F$_6$ formation and HFA depletion, and the kinetic parameters can be determined graphically from the linear plot in Figure 3. Although eq 3 deals in specific flow rates R in molecules s^{-1} cm^{-3}, it is simpler to discuss the observables in terms of flow rates, molecules s^{-1} ($R = F/V$). The ordinate is the net rate of HFA depletion (and thus the net CF$_3$ production) divided by the C$_2$F$_6$ production rate, $F^0{}_{C_2F_6}$. The abscissa is the inverse square root of the production rate of C$_2$F$_6$. For the data in Figure 3 (representative of several data sets) the flow of HFA was varied from 1.9 × 10^{14} to 3 × 10^{16} s^{-1}. The CO$_2$ laser beam fluence was held constant, and the extent of depletion was nominally 27%, decreasing only a few percent over this range of HFA flows.

The y-axis intercept represents the flow rate of C$_2$F$_6$ in the limit of high CF$_3$ density. At this limit, the rate of the first-order losses of CF$_3$ on the walls (k_w) and the escape rate of CF$_3$ from the cell (k_e) are negligible. The value of the intercept therefore yields the overall stoichiometry for converting HFA to C$_2$F$_6$. The fact that the intercept is approximately 2 indicates that two HFA molecules must be decomposed to form each C$_2$F$_6$ molecule. This implies that the IRMPD of HFA forms one CF$_3$ and one COCF$_3$
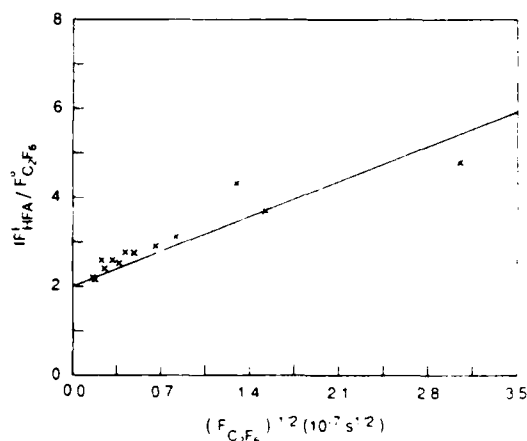

Figure 3. Reciprocal plots for HFA. Data were taken with the large aperture (3 mm). The solid line is the least-squares fit to the data

according to reaction 1 and that COCF$_3$ does not decompose to a significant degree to form CO and CF$_3$. This result is actually expected in view of the known thermal decomposition kinetics of CF$_3$CO, which results in a lifetime of 14 s at 300 K. This CF$_3$CO lifetime is a multiple of the residence time of the average molecule inside our Knudsen cell so that the degree of decomposition of CF$_3$CO should be very small. If the unimolecular decomposition of CF$_3$CO were competitive with its escape out of the cell, the intercept of the straight line in the reciprocal plot should move toward 1, and this is clearly not the case (Figure 3).

In view of the importance of the intercept in relation to the mechanism, we have done two additional tests. The first test involved the careful calibration of the mass spectrometer sensitivity to C$_2$F$_6$. During some of the HFA IRMPD experiments, a small known amount of C$_2$F$_6$ was passed through the reactor, as an internal standard, to ensure that the sensitivity remained constant during the experiment. The second test was to switch the precursor gas to CF$_3$I, for which we know the initial stoichiometry (reaction 9). Using the reciprocal plot analysis, we have analyzed data from the large- and small-aperture reactors. The y intercept was 2, and the rate constants derived from the slope of the line were consistent with the previously measured values.[2] With these tests we are convinced that the intercept of 2 in the IRMPD of HFA is accurate. The only apparent explanation of this intercept is that reaction 2 is unimportant under our conditions.

The slope of the line in Figure 3 can be analyzed to determine the wall loss rate constant, k_w, of the CF$_3$. Using the known k_e and k_e values and forcing the straight line through 2.0, we derive a k_w of 0.23 s^{-1}. This corresponds to a sticking coefficient of 2.2 × 10^{-5}. This means only 1 in 45 000 wall collisions results in the loss of the CF$_3$, and therefore the gold-coated reaction vessels are good reactors for CF$_3$ radical studies.

Back Reaction. Given that the COCF$_3$ is stable in our Knudsen cell, it is important to investigate whether the back reaction 3 to form an HFA occurs under our conditions. The mass spectrometer measurement of the depletion of HFA versus F_{HFA} at constant CO$_2$ laser fluence will reveal if reaction 3 occurs. At constant laser fluence the extent of initial depletion, reaction 1, in the beam of the IR laser scales linearly with the partial pressure of HFA, whereas the average net value of f will depend on the extent of reaction 3. Qualitatively, we expect f to decrease with increasing density of HFA. Figure 4 presents our data on the pressure dependence of the HFA depletion of constant CO$_2$ laser fluence

Figure 4, parts a and b, show the dependence of f for HFA IRMPD in the large- and small-aperture reactors, respectively, for several different data sets. The trend is the same for all the data sets and confirms the qualitative arguments put forth above The flow rate at which the decrease from the low-pressure-limiting value of f is apparent scales approximately with the escape rate constants and therefore with partial pressure. The difference between the observed net depletion and the depletion at low pressure (where there is no recombination) represents the rate
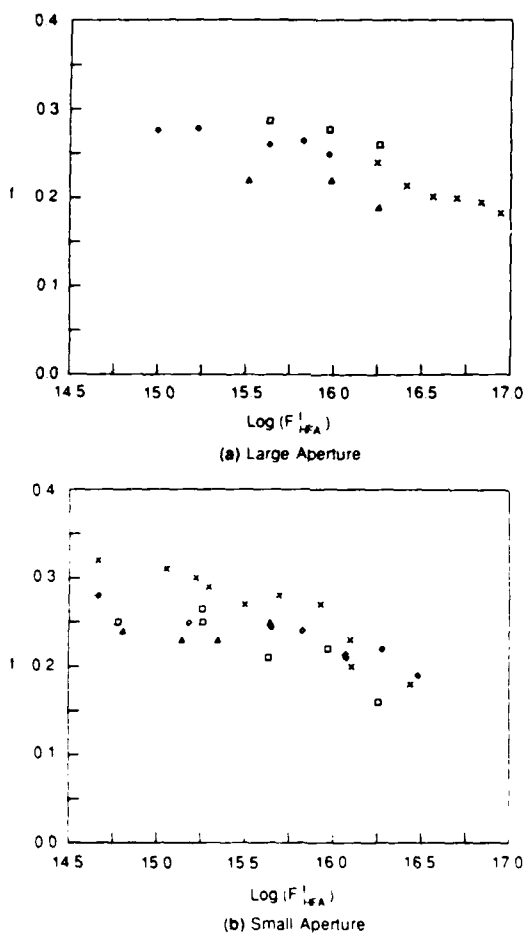
Figure 4. HFA depletion versus logarithm of the input flow for the large aperture. (a) and the small aperture (b). The different symbols represent data taken on different days. The difference in the extent of the depletion on different days is due to changes in the output power of the photolysis laser.
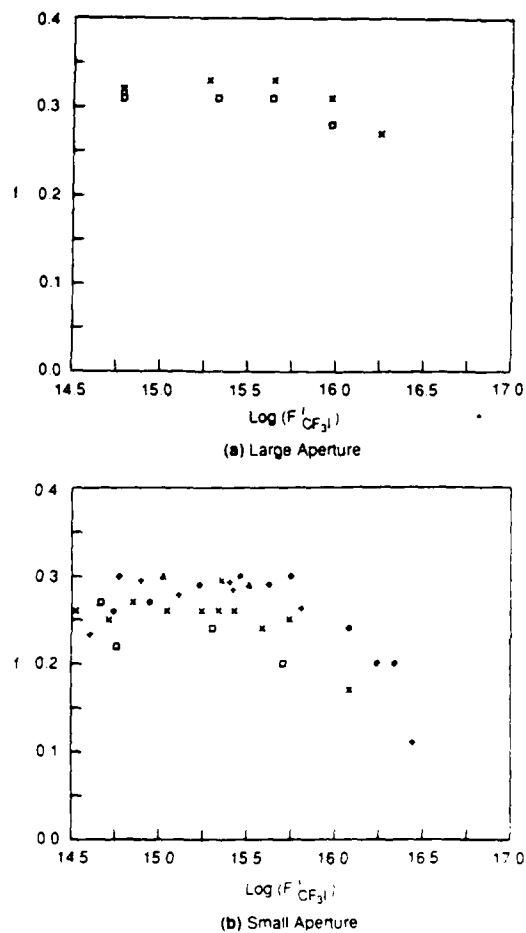

Figure 5. CF_3I depletion versus logarithm of the input flow for the large aperture (a) and the small aperture (b). The different symbols represent data taken on different days. The variation in the extent of depletion on different days is due to variations in the output power of the photolysis laser.

effect due to back recombination. At the highest flows studied, approximately one-third of the HFA that was initially decomposed re-formed.

Figure 5 presents similar data for the f dependence of CF_3I IRMPD that clearly demonstrate that even in this case the reverse of the dissociation has to be taken into account at higher flow rates. In the case of CF_3I the reaction partner of CF_3 radical may be molecular I_2 formed on the walls of the reaction vessel by heterogeneous recombination of the primary photolysis product I. The REMPI results discussed in ref 4 show that atomic I is short lived, so that it is not available as a reaction partner for CF_3. The metathesis reaction, (10), has been shown to occur without activation energy: As ancillary evidence we cite the fact that I_2 can be observed in the reactor in the course of IRMPD of CF_3I.

The comparison between the corresponding sets of data in Figures 4 and 5 reveals the fact that the flow rates at which f significantly departs from its low-pressure-limiting value is approximately the same for both CF_3I and HFA. This implies that the rates for back recombination are approximately equal. We are, however, unable to determine the rate constants for the back reactions because the densities of the reacting species ($COCF_3$ and I_2 for the respective precursor gases) were not measured.

REMPI Data. A single CO_2-laser pulse decomposes a fraction of the HFA in the beam volume. The extent of depletion in the beam volume, f_{beam}, can be calculated from the mass spectrometric measurement of the depletion f, assuming there is no back reaction to reform HFA, and is given by

$$f_{beam} = \frac{V_{cell}k_e t_p}{V_{beam}} \frac{f}{1 - f(1 - k_e t_p/2)} \qquad (5)$$

where t_p is the period between two IR-laser pulses. This expression will underestimate f_{beam} to the extent that the back reaction occurs.

For our typical $f = 0.25$ and $t_p = 0.1$ s, we derive $f_{beam} = 0.44$. For an HFA flow of 1×10^{16} s^{-1} the initial HFA density is 5.1×10^{13} cm^{-3}, and the density of CF_3 formed in the beam volume is 1.7×10^{13} cm^{-3}.

The radicals formed in the beam volume rapidly diffuse at molecular speed to fill the entire cell volume. After a series of wall and gas collisions, the radicals reach a thermalized, uniform density. This process is observed to be completed after approximately 1 ms. The CF_3 density throughout the cell is smaller than the initial density in the beam volume by the ratio of V_{cell}/V_{beam}. For the case above .he CF_3 density after homogeneous mixing amounts to 5.4×10^{11} cm^{-3}. The thermalized radicals will undergo gas and surface reactions, decreasing the radical density even further until the next CO_2-laser pulse generates another burst of hot radicals. If the first-order radical loss rate is fast (for instance if the sticking coefficient for CF_3 on the walls were large), the CF_3 density will drop to zero at some point in time between the two IR-laser pulses, and the time dependence of the CF_3 density over several cycles will be a series of temporal spikes. If the radical loss rate is small (on the order of the escape rate or less), a portion of the CF_3 created by the previous pulse will remain in the reactor as subsequent pulses generate additional radicals. The time dependence of the CF_3 density observed over several cycles will then appear as a sawtooth pattern on a large steady-state background (see the Appendix).

The REMPI signal is linearly proportional to the CF_3 density, so it will have the same temporal characteristics as the CF_3 density, namely, a sawtooth pattern. The time dependence of the REMPI
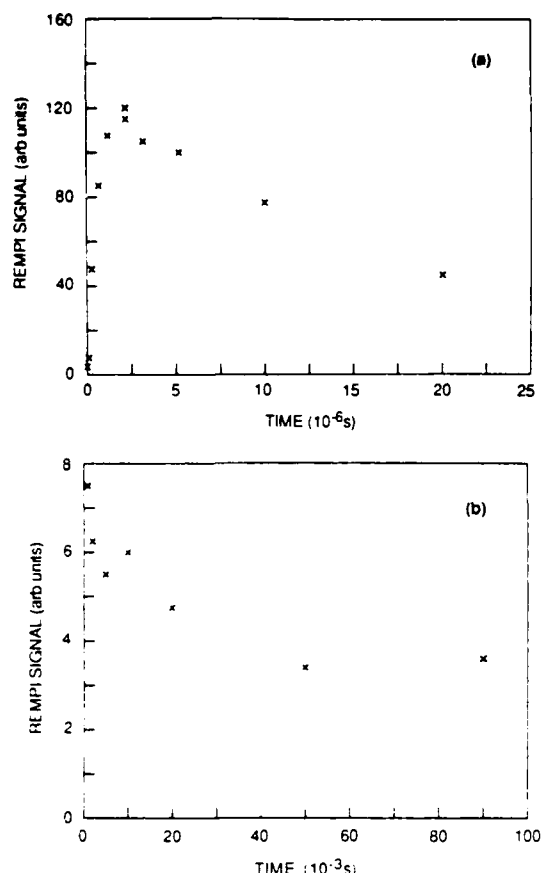
Figure 6. REMPI signal from CF_3 radicals versus time after the photolysis laser has fired. The HFA flow was 1×10^{16} s^{-1}, and the depletion was 22%. The photolysis laser was run at 10 Hz. The signal at early time, (a) is due to CF_3 concentrated in the photolysis beam volume. The signal is smaller at later times (b) because the CF_3 has diffused to fill the entire cell.

signal between consecutive CO_2-laser pulses is shown in Figure 6 for a HFA flow rate of 1×10^{16} molecules s^{-1} and a depletion of 22%. The signal at early time is large (Figure 6a) because the CF_3 is still concentrated in the beam volume before the radicals have the chance to diffuse throughout the cell. The maximum of the signal occurs at approximately 2.5 μs. This time delay to the maximum signal strength may be due either to jitter in the synchronization of the two lasers or more likely to a misalignment of the two lasers. We did not study this effect in detail because we will not make use of this early portion of the REMPI signal to study the kinetics. Shown in Figure 6b is the time dependence of the REMPI signal after the radicals have thermalized and reached a uniform density (i.e., after 1 ms). The signal decreases from a maximum of 7 mV to a steady-state value of 4 mV. The difference represents the incremental increase in CF_3 caused by a single laser pulse. The steady-state signal results from radicals made during the previous laser pulses, and Figure 6b displays the situation of long-lived radicals that are persistent on the time scale of 100 ms, in agreement with the low-sticking coefficient derived from the results presented in the previous section on the mass spectrometric sampling technique (low values for k_w, Figure 3).

The time dependence of the CF_3 REMPI signal at various flow rates is shown in Figure 7 with the CO_2 laser running at 20 Hz. The top curve represents the highest flow of HFA and the highest rate of formation of C_2F_6. The loss rate of CF_3 is significantly faster for higher flow rates, because second-order loss reactions occur in competition with first-order reactions. This situation is representative of many kinetic situations, and therefore it was absolutely imperative to find a way to quantitatively treat the kinetic data in such a mixed situation.

Calibration. The REMPI signal must be calibrated to obtain quantitative kinetic data in our Knudsen cell. To this end both
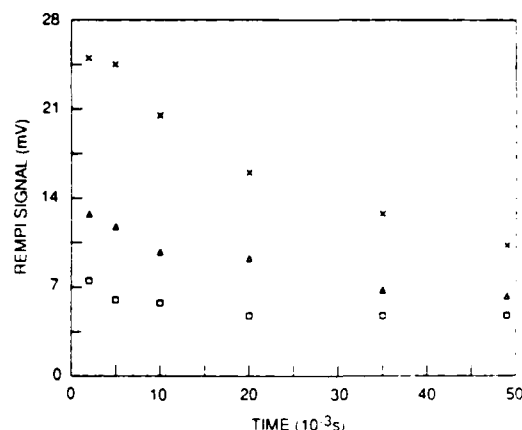

Figure 7. REMPI signal from CF_3 radicals versus delay time for HFA flows (s^{-1}) of 8.80×10^{16} ($\times$), 3.63×10^{16} ($\triangle$) and 1.76×10^{16} ($\square$). The photolysis laser was run at 20 Hz. Data for three other flows are not shown.
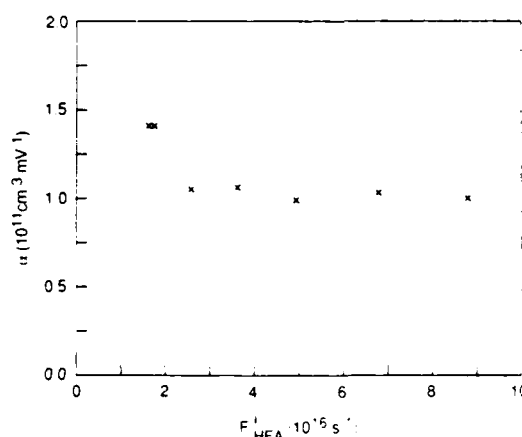

Figure 8. α versus HFA flow. α is the calibration factor to convert the REMPI signals to an absolute density. The values at high flow are incorrect because of the back reaction. The value used to reduce the data is 1.5×10^{11} cm^{-3} mV^{-1}.

the REMPI experiment and the mass spectrometric experiment are performed under identical experimental conditions. The difference REMPI signal is calibrated in terms of an absolute density of CF_3 created per CO_2-laser pulse by observing the depletion of HFA. This mass spectrometric measurement is based on the steady-state value of f under conditions of $F_{HFA} \leq 10^{16}$ molecules s^{-1}, that is, under conditions of negligible back recombination (cf. Figure 4a). The stoichiometric factor of one CF_3 radical per HFA is employed.

We define a calibration factor α as

$$\alpha = \Delta[CF_3]/\Delta(\text{REMPI signal}) \qquad t = 0 \qquad (6)$$

$$\Delta[CF_3] = fF_{HFA}t_p/V_{cell} \qquad (7)$$

Equation 7 relates the observed (steady state) fractional decomposition of HFA to the calculated initial value by using in essence only geometrical parameters and the period of the photolysis laser, t_p, both of which are easily determined. The α values calculated by using expressions 6 and 7 are plotted in Figure 8 as a function of F_{HFA}. These values are flow dependent, whereas we expect the proportionality coefficient (ionization efficiency) of thermalized radicals to be independent of F_{HFA} and f. The reason for the variation in α is that f is not a good representation of f_{beam} when the back reaction occurs. In other words, under steady-state condition f_{beam} decreases to f because the back-recombination reaction, -3, has time to increase the HFA density at the expense of the CF_3 density. To get α without this complicating kinetic effect, we extrapolate α to zero flow, where the back reaction is negligible and where f is directly related to f_{beam}. Figure 8 suggests a value of 1.5×10^{11} CF_3 radicals per millivolt.
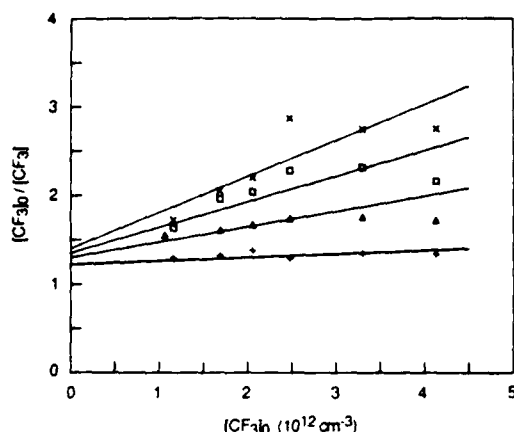
Figure 9. Reciprocal plot for determining the first- and second-order rate constants for the loss of CF_3: 49 ms (×); 35 ms (□); 20 ms (△); 10 ms (+).

Because the flow dependence of α is absorbed entirely in f, the data of Figure 8 correspond in a 1:1 manner to data of Figure 4. This relationship is easily recognized when substituting eq 7 into eq 6. The above value for α will be used to reduce the data at all flow rates.

Reciprocal Plots. Given the absolute calibration of the REMPI signal in terms of the CF_3 density, we can analyze the time dependence of the CF_3 REMPI signal to determine quantitatively the first- and second-order loss rate constants for CF_3 in the Knudsen cell. The differential equation for the rate of change of CF_3 can be integrated in closed form to give a reciprocal type solution if the first-order loss rate constant does not change as a function of flow (eq 8). This is not entirely true for the data displayed in Figure 9. For the family of curves corresponding to the higher flow rates, the back reaction is important (following the data of Figure 5) because the density of $COCF_3$ increases with the product fF_{HFA}. It follows that the relative importance of the rate of the back reaction will increase relative to all other first-order loss processes of CF_3. Although the rate of the back reaction is first order in each component, that is, CF_3 and CF_3CO, the overall rate is somewhere between first and second order due to the dependence of both reaction partners on each other.

The algebra described and linearized in eq 8 absorbs most of this changing contribution of the back-reaction rate with increasing F_{HFA} in an increased value for k_1, the total first-order loss rate constant for CF_3:

$$\frac{[CF_3]_0}{[CF_3]} = \exp(k_1 t) + \frac{2k_r}{k_1}[CF_3]_0(\exp(k_1 t) - 1) \qquad (8)$$

k_1 and k_r can be found using an iterative fitting procedure of data for one flow rate. Alternatively, a graphical solution can be used if data at different flow rates are available. The data for various flow rates at a given delay time, t, will yield a straight line when plotted according to eq 8. Figure 9 presents such a plot. The intercept yields k_1, and the slope k_r. Raw data such as plotted in Figure 7 have been analyzed according to eq 8 for the four delay times of 10, 20, 35, and 49 ms. The average value for k_r was 3.5 × 10^{-12} cm^3 s^{-1}. The expected value from the literature was 3 × 10^{-12} cm^3 s^{-1}, and it is seen that the agreement is excellent, at least within the framework of the foregoing assumption about the back reaction. The average value of k_1 was found as 8 s^{-1}. The escape rate constant is known to be 0.67 s^{-1}, and the wall loss rate constant is approximately 1.4 s^{-1} as measured by the mass spectrometric sampling technique. The difference between the measured number of 8 s^{-1} and the sum of the above-mentioned first-order rate constants (2 s^{-1}) is associated with the back-recombination reaction, (3).

Conclusion

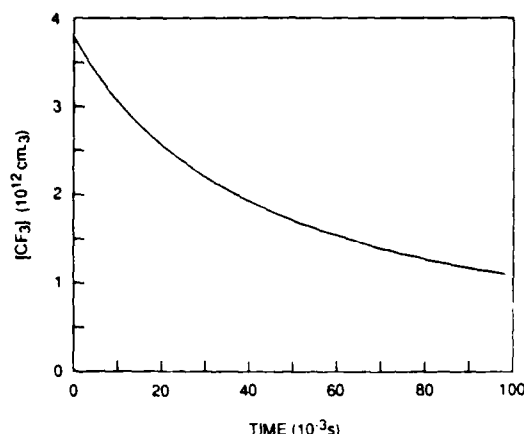This work addresses two subjects: one is the development of a technique with expanded capabilities for detecting the free

Figure 10. CF_3 density (cm^{-3}) versus time between laser pulses (10 Hz): $F_{CF_3I} = 5.0 \times 10^{16}$ s^{-1}; $f = 0.25$; $k_1 = 1.0$ s^{-1}; $k_r = 3.0 \times 10^{-12}$ cm^3 s^{-1}.
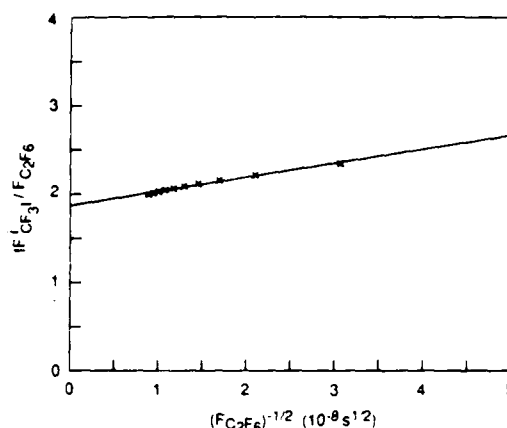

Figure 11. Reciprocal plot for various depletions ($f = 0.05-0.50$). The ordinate is the rate of CF_3 production divided by the rate of C_2F_6 production. The line is a least-squares fit to the data points derived with the time-dependent solution for the CF_3 density. k_1, k_r, and F_{CF_3I} are the same as in Figure 10.

radical reactants as well as their reaction products in fast free radical reactions, and the other investigates the detailed reaction mechanism of CF_3 free radical kinetics in a Knudsen cell with hexafluoroacetone (HFA) as a radical precursor.

We present the comparison of two techniques adapted to studying the kinetics of the CF_3 radical: the first is based on observing the rate of formation of the recombination product, C_2F_6, by the well-documented molecular-beam mass-sampling technique, and the other is the observation of the decay of the radical reactant, CF_3, by resonance-enhanced multiphoton resonance ionization (REMPI). Both techniques yield the same kinetic parameters and thus give us confidence in the application of the REMPI technique for other radicals. In addition, the REMPI technique enables one to study the thermalization of excited free radicals after photolysis generation, after which the chemistry ensues on a slower time scale. Furthermore, the ability to measure absolute radical densities as a function of time in the reaction vessel means that absolute REMPI cross sections or ionization coefficients of free radicals can be obtained. To quantitatively treat competing first- and second-order radical reactions, one needs to know absolute densities; thus this technique can be used to study complex kinetics involving free radicals.

The validation of the technique was demonstrated by using HFA as a precursor to CF_3. The IR-multiphoton decomposition using a collimated laser beam leads to C–C bond breaking, resulting in CF_3 and CF_3CO with both radicals being stable under our conditions. We further demonstrated that the back recombination to HFA of the above radicals occurs only at flow rates above 10^{16} s^{-1}. In the mass spectrometric study the back recombination was unimportant, whereas in the REMPI study the flow
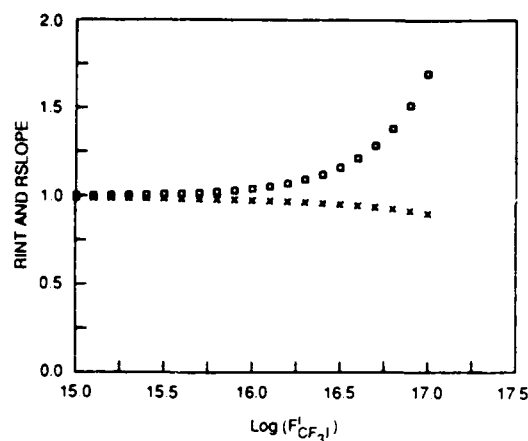
Figure 12. Error analysis of the steady-state assumption. The ×'s represent RINT, the ratio of observed and expected intercepts in the reciprocal plot. The boxes represent RSLOPE, the ratio of observed and expected slopes in the reciprocal plot.
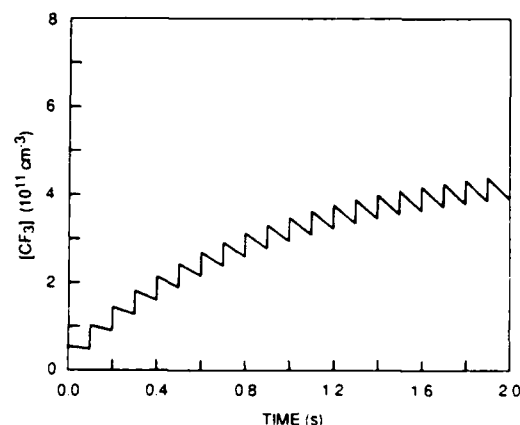

Figure 13. CF₃ density (cm⁻³) versus time for several laser pulses. The laser is first turned on at the zero of time: $F_{CF_3I} = 1.0 \times 10^{15}$ s⁻¹; $f = 0.25$; $k_1 = 1.0$ s⁻¹; $k_r = 3.0 \times 10^{-12}$ cm³ s⁻¹.
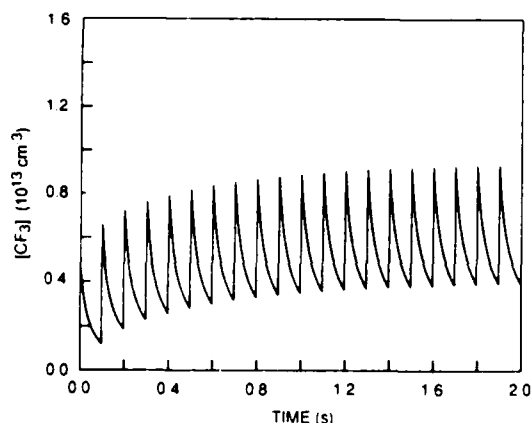

Figure 14. CF₃ density (cm⁻³) versus time for several laser pulses. The laser is first turned on at the zero of time: $F_{CF_3I} = 1.0 \times 10^{17}$ s⁻¹; $f = 0.25$; $k_1 = 1.0$ s⁻¹; $k_r = 3.0 \times 10^{-12}$ cm³ s⁻¹.

rate had to be chosen in a range where the back reaction significantly contributed due to signal/noise considerations. However, this limit will be lowered in further studies.

Appendix: Model Calculation To Verify That the Steady-State Approximation Is Valid for Pulsed-Laser Experiments

The mass spectrometry data analysis for the VLPΦ system has typically been done two ways. One technique[2] is to run the photolysis laser at a low repetition rate (0.25 Hz), where the products escape and precursor gas refills the cell before the laser fires again. In this type of experiment the total yield of the products and the total extent of depletion of the precursor gas from a single laser pulse are measured by integrating the mass spectrometer signal. In the second technique,[1] the photolysis laser is run at a high repetition rate (10 or 20 Hz). Here the products are continuously pumped away, and the precursor gas is continuously replenished by fresh sample. In this type of experiment, the flow of products and precursor gas out of the cell are measured with the mass spectrometer and are observed to be essentially constant.

The first variable to study in the high repetition rate systems is the extent of depletion of the precursor gas. The steady-state depletion, f, is simply the percentage decrease in the flow of precursor gas coming out of the cell when the photolysis laser is turned on, as determined by the mass spectrometer. This variable represents the depletion averaged over several cycles and throughout the cell, whereas the actual depletion, f_{beam}, is the percentage decrease in the density of the precursor in the laser-beam volume when the laser fires. An analytical expression can be derived to relate the density depletion in the beam volume to the flow depletion derived from the mass spectrometry measurement. In the steady-state treatment the rate of depletion is simply the flow of precursor gas times f:

$$R_{depl} = k_e V_{cell} [A]_0 f$$

Where $[A]_0$ is the initial density of the precursor A. k_e is the escape rate constant, and V_{cell} is the volume of the cell. For the time-dependent depletion the rate of depletion is the number of molecules in the beam volume that are decomposed divided by the period of the laser:

$$R_{depl} = f_{beam} [A]_{-\delta t} V_{beam} / t_p$$

Where $[A]_{-\delta t}$ is the actual density in the beam just before the laser fires. The distinction that the precursor density is not actually a constant is included here for completeness. The steady-state density is approximately the average of the density just before and just after the laser fires, $[A]_{+\delta t}$:

$$[A]_{ss} = ([A]_{-\delta t} + [A]_{+\delta t})/2$$

The difference in density just before and after the pulse can be determined from the net flow of the precursor into the cell:

$$[A]_{-\delta t} - [A]_{+\delta t} = k_e [A]_0 t_p f$$

We can now find the relation between f and f_{beam} by equating the two expressions for the rate of depletion and by eliminating $[A]_{-\delta t}$:

$$f = \frac{f_{beam} V_{beam}}{V_{cell} k_e t_p} \frac{1}{1 + (1 - k_e t_p/2) f_{beam} V_{beam}/V_{cell} k_e t_p}$$

This expression is equivalent to eq 5 and can be seen to be reasonable by examining the f for various f_{beam} values and repetition rates. For instance, given that one-half of the molecules in the laser beam are decomposed, $f_{beam} = 0.5$, f equals 0.28, 0.43, and 0.66 for repetition rates of 10, 20, and 50 Hz, respectively. These values were derived by using $V_{cell} = 460$ cm³, $V_{beam} = 15$ cm³, and $k_e = 0.43$ s⁻¹ for HFA with a 3-mm aperture.

For a high repetition rate laser, the kinetic mechanism can be analyzed with the assumption that the reacting species are created continuously and have a steady-state density in the cell. This is, of course, not strictly true because these reactive species are created essentially instantaneously by the pulsed laser, after which they undergo reactions to fractionally (or completely) reduce the density. The time dependence of the density is thus a sawtooth function on top of a constant background density which builds up from reactive species produced in previous laser pulses. The

point of this appendix is to determine the range of conditions for which this steady-state analysis is a valid technique to derive rate constants.

The first system to examine involves only first-order processes, for instance:

$$CF_3I + nh\nu \rightarrow CF_3 + I$$

$$CF_3 + Br_2 \xrightarrow{k_s} CF_3Br + Br$$

$$CF_3 \xrightarrow{k_1} \text{escape or wall loss}$$

$$Br \rightarrow \text{escape or wall loss}$$
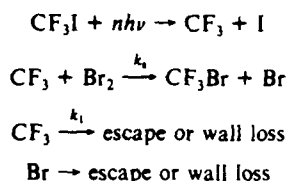
When the Br_2 density is high, no other reactions need to be considered, and the Br_2 density is constant. A steady-state analysis of the system can be done by considering the production rate of CF_3 to be continuous with the value of fF_{CF_3I}. f is the average depletion as measured with the mass spectrometer. F_{CF_3I} is the flow of CF_3I in molecules s^{-1}. The rate equations for this system are trivial and are set equal to zero for the steady-state analysis. We can immediately write down an expression for the CF_3 production divided by the CF_3Br production:

$$\frac{fF_{CF_3I}}{F_{CF_3Br}} = \frac{k_1}{k_s}\frac{1}{[Br_2]} + 1$$

Experimental data for a range of flow and depletion can be plotted in a reciprocal plot, the ratio of production rates versus $1/[Br_2]$. If the steady-state model is correct, the data will form a straight line in this plot with an intercept of unity and the slope equal to k_1/k_s. If k_1 is known, then k_s can be determined immediately.

The time-dependent solution for the CF_3 density between successive laser pulses can be found by solving the differential equation with the two loss terms:

$$[CF_3](t) = [CF_3]_0 \exp(-(k_1 + k_s[Br_2])t)$$

$[CF_3]_0$ is the uniform density immediately after the laser fires. This value can be found from the requirement that the background density of CF_3 is constant, i.e., the amount of CF_3 produced by a single laser shot must equal the amount of CF_3 lost in the period between laser shots:

$$[CF_3]_0 - [CF_3](t=t_p) = fF_{CF_3I}t_p/V_{cell}$$

Substituting in the expression for $[CF_3](t)$, we find

$$[CF_3]_0 = \frac{fR_{CF_3I}t_p}{V_{cell}}\frac{\exp(-(k_1 + k_s[Br_2])t_p)}{1 - \exp(-(k_1 + k_s[Br_2])t_p)}$$

The average production rate of CF_3Br can be found by integrating over the period between laser shots:

$$F_{CF_3Br} = \frac{V_{cell}}{t_p}\int_0^{t_p} k_s[CF_3][Br_2]\,dt =$$

$$\frac{V_{cell}k_s}{t_p}[CF_3]_0[Br_2]\frac{\exp(-(k_1 + k_s[Br_2])t_p)}{k_1 + k_s[Br_2]}$$

The ratio of the production rate of CF_3 divided by the production rate of CF_3Br is exactly the same as was found with the steady-state assumption. There is no error introduced from flow rate, extent of depletion, or repetition rate of the laser. The conclusion for this type of reaction mechanism involving only first-order processes is that the steady-state assumption is valid for determining rate constants.

The next system that we will examine involves second-order losses:

$$CF_3I + nh\nu \rightarrow CF_3 + I$$

$$CF_3 + CF_3 \xrightarrow{k_2} C_2F_6$$

$$CF_3 \xrightarrow{k_1} \text{escape or wall loss}$$
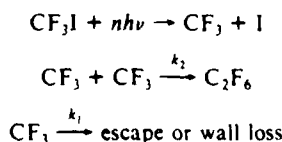
The I atom and I_2 (which is formed by I recombination on walls) are assumed to be nonreactive with the CF_3. This system was studied to determine the recombination rate of two CF_3 radicals.[1] The steady-state solution of this system again assumes that the radicals are created continuously and have a constant density. The rate equations for CF_3, CF_3I, and C_2F_6 are set equal to zero and then rearranged to derive the relationship between the rate of production of CF_3 and the rate of production of C_2F_6:

$$\frac{fF_{CF_3I}}{F_{C_2F_6}} = 2 + k_1(V_{cell}/k_r)^{1/2}F_{C_2F_6}^{-1/2}$$

Experimental data for a range of flow and depletion can again be examined in a reciprocal plot (Brauman plot), the ratio of production rates versus $F_{C_2F_6}^{-1/2}$. If the steady-state model is correct, the data will form a straight line with an intercept of 2 and a slope of $k_1(V_{cell}/k_r)^{1/2}$. If k_1 is known (or can be determined by changing the escape rate from the cell), k_r can be determined immediately. The steady-state density of CF_3 in the cell can also be determined by algebraic rearrangement of the steady-state rate equations:

$$[CF_3]_{ss} = \frac{-k_1 + (k_1^2 + 8k_2 fF_{CF_3I}/V_{cell})^{1/2}}{4k_2}$$

$[CF_3]_{ss}$ is 2.0×10^{12} cm^3 for a typical set of conditions: $k_1 = 1.0$ s^{-1}, $k_r = 3.0 \times 10^{-12}$ cm^3 s^{-1}, $F_{CF_3I} = 5.0 \times 10^{16}$ s^{-1}, and $f = 0.25$.

The time-dependent CF_3 density can be determined for the period between laser pulses by analyzing the differential rate equation with first- and second-order loss terms. This is a Bernoulli-type differential equation and can be solved with a simple transformation. The solution is

$$\frac{[CF_3](t)}{[CF_3]_0} = (\exp(k_1t) + 2k_r[CF_3]_0(\exp(k_1t) - 1)/k_1)^{-1}$$

$[CF_3]_0$ is the density at the zero of time, immediately after the laser fires. This can be determined by requiring that the background density of CF_3 has reached a steady state; in other words, all of the CF_3 produced in a single laser shot must be lost before the next laser shot:

$$[CF_3]_0 - [CF_3](t=t_p) = fF_{CF_3I}t_p/V_{cell}$$

Substituting in the expression for the $[CF_3](t)$ gives a quadratic expression for $[CF_3]_0$ with one positive root. The density of CF_3 between two laser pulses is shown in Figure 10 for the same conditions used to calculate $[CF_3]_{ss}$.

The time-averaged rate of production of C_2F_6, $F_{C_2F_6}$, can be calculated with the expression for CF_3:

$$F_{C_2F_6} = \frac{V_{cell}}{t_p}\int_0^{t_p} k_r([CF_3](t))^2\,dt$$

An analytical solution for the integral is not obvious; therefore, it will be solved numerically:

$$F_{C_2F_6} = \frac{V_{cell}k_r[CF_3]_0^2}{t_p}\sum_n\left(\frac{[CF_3](t)}{[CF_3]_0}\right)^2 \Delta t$$

where the period between laser shots has been divided into n steps, and $\Delta t = t_p/n$. The flow of C_2F_6 can be calculated for a range of depletions ($F_{CF_3I} = 5.0 \times 10^{16}$ s^{-1}, $f = 0.05$–0.50) and then plotted in a reciprocal plot, Figure 11, as discussed above for the steady-state treatment. A least-squares analysis was done to determine the slope and intercept from these artificial data. These can be compared to the expected values; RSLOPE is the slope of the least-squares line divided by the expected slope, $k_1(V_{cell}/k_r)^{1/2}$, and had a value of 1.28. RINT is the intercept of the least-squares line divided by the expected value, 2, and had a value of 0.936. If the steady-state analysis had been valid, then the artificial data would have resulted in ratios of unity. The rate constants that would have been derived from the reciprocal plot would have been wrong to the extent that these ratios were not unity.

These ratios have been calculated for a range of CF_3I flows, Figure 12. At low flow ($<1 \times 10^{16}$ s^{-1}), the errors in the rate

constants that would result from using the steady-state analysis would be small and insignificant. At higher flows the assumption breaks down. (Indeed, in a real experiment at higher flows other secondary reactions may be occurring, so that the simple reaction mechanism is no longer sufficient; for instance, the reaction between CF_3 and I_2 or I could be occurring to a significant extent.) The reason the steady-state assumption is not valid at high flow can be explained by using the density versus time curves in Figures 10, 13, and 14. In Figures 13 and 14 we have plotted the density of CF_3 over several laser pulses, the very first pulse occurring at the zero of time. After many pulses the background density of CF_3 reaches a constant value. At low flow, Figure 13, the ratio of peak to background density is close to unity; the average density over the laser period is not very different from the actual density at any time. The first-order loss, $k_1 = 1.0$ s^{-1}, is comparable to the second-order loss, $k_r[CF_3] = 1.2$ s^{-1}. At high flow, Figure 14, the peak to background density is large, $\simeq^8/_3$, so the average density is substantially different than the density immediately after the pulse. The second-order loss, from 9 to 24 s^{-1}, is very much larger than the first-order loss at these densities. Because it is a second-order process, most of the C_2F_6 production is occurring immediately after the laser pulse, and it is incorrect to average the total production over the entire laser period. The conclusion from these model calculations is that it is valid to use the steady-state assumption under all conditions when only first-order processes are important. When second-order processes are included, the steady-state assumption will break down when the second-order process is dominant.

Registry No. HFA, 684-16-2; CF_3^*, 2264-21-3.

Appendix D

[3+2] RESONANCE ENHANCED MULTIPHOTON IONIZATION OF I AND Br
FORMED FROM THE INFRARED MULTIPHOTON DECOMPOSITION
OF CF_3I AND CF_3Br

[3 + 2] resonance enhanced multiphoton ionization of I and Br formed from the infrared multiphoton decomposition of CF_3I and CF_3Br[a]

Robert M. Robertson,[b] David M. Golden, and Michel J. Rossi[c]

Department of Chemical Kinetics, Chemical Physics Laboratory, SRI International, Menlo Park, California 94025

Resonance enhanced multiphoton ionization (REMPI) has been used to study the products of the infrared multiphoton decomposition (IRMPD) of CF_3I in a very low-pressure photolysis (VLPΦ) cell. The strongest REMPI signals are due to the ground state $I(^2P_{3/2})$ and the spin-orbit excited state $I^*(^2P_{1/2})$. The origins of I and I* were determined from the time and IR laser fluence dependences of the REMPI signal. I* is formed by visible single photon dissociation of vibrationally excited CF_3I and by visible multiphoton dissociation of I_2 and thermal CF_3I. The ionization efficiency of I has been determined relative to NH_3 for our probe laser conditions, and the sticking coefficient of I with gold surfaces has been determined. The REMPI spectra of the products of the IRMPD of CF_3Br is also presented.

INTRODUCTION

Resonance enhanced multiphoton ionization (REMPI) has been used successfully in recent years as a diagnostic tool in kinetic systems, e.g., flames,[1] pyrolysis,[2] photodissociation,[3] plasmas,[4] surface scattering,[5] and gas collisions.[6] REMPI is advantageous in many instances because it provides high selectivity, sensitivity, and temporal resolution. Furthermore, the detection limits using REMPI are frequently lower than for luminescence measurements, and many nonfluorescing molecules can be detected with REMPI.

Recently we have begun to investigate the interaction of atoms and free radicals with surfaces in a very low-pressure photolysis (VLPΦ) cell. The transient species are created by infrared multiphoton decomposition (IRMPD) of an appropriate precursor in a collimated (unfocused) laser beam and are allowed to react with the cell walls or a temperature-controlled sample surface. Modulated molecular-beam mass spectrometry is used to monitor the effluents from the VLPΦ cell, and REMPI is used to monitor the transient species *in situ* and in real time. We are able to calibrate our REMPI signals in terms of absolute densities based on the mass spectrometer measurements of the precursor depletion. Knowledge of the absolute densities of transient species is necessary for the quantitative treatment of competitive first- and second-order kinetic processes inside the reactor.

In this paper the [3 + 2] REMPI spectra of I and I* atoms generated (directly or indirectly) by IRMPD of CF_3I are reported. The time and IR-fluence dependence of the REMPI signals is used to study the origin of the atoms. Due to the low-pressure conditions and the predominance of gas-wall collisions in the Knudsen cell, the I atoms are lost primarily to the vessel walls and the sticking coefficient for this reaction is determined. In the VLPΦ reactor, we are able to determine the absolute density of I formed by the IRMPD of

CF_3I. We use this to determine the ionization efficiency of I relative to a stable gas, NH_3, for our probe laser conditions. The REMPI spectra resulting from the IRMPD of CF_3Br is presented. The [3 + 1] REMPI[7] of CF_3 was not observed from the IRMPD of either of these precursor gases, because of the background signal due to visible laser photodissociation/ionization of the precursors. We will discuss previous studies[8-11] of the REMPI of I and I* generated by the IRMPD of CF_3I. In another study[12] the REMPI spectra of CF_3 have been studied using hexafluoroacetone as the precursor. In these experiments, the gas-phase rate constant for CF_3 recombination was verified, the CF_3 REMPI signal was calibrated, and the etching of silicon by CF_3 radicals was quantitatively studied.

EXPERIMENTAL

The VLPΦ experiments were performed at low pressure ($<2 \times 10^{-3}$ Torr) in a Knudsen reactor equipped with wire electrodes for the collection of ions and electrons. The cell, which has been described previously,[12] is an all stainless-steel six-way cross where four branches are fitted with windows for the crossed IR- and visible-laser beams. One branch is blanked off, and the other branch houses a butterfly valve with an interchangeable exit aperture mounted in the center. The cell walls have been coated with gold by vacuum evaporation in order to minimize CF_3 wall losses.

The ions and electrons created by REMPI were collected on two tantalum wire-loop electrodes that were placed above and below the intersection of the two lasers. The electrodes were biased at plus and minus 90 V for the collection of electrons and ions, respectively. The electrical currents were converted to voltages using a load resistor of $10^7 \, \Omega$, then the electron signal was inverted and added to the ion signal.[13] The time dependence of the total REMPI signals following the dye laser pulse are shown in Fig. 1 for collection voltages of ± 9 and ± 90 V. The total charge was collected for high and low collection voltages. However, the signal amplitude was smaller at the lower collection voltage
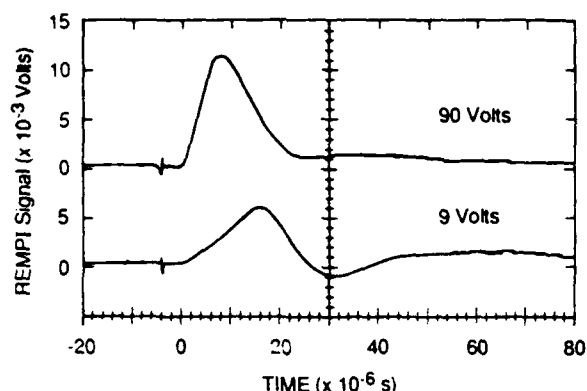
FIG. 1. I-atom REMPI signal at 474.5 nm (averaged over 128 shots) vs time after the probe laser is fired for collection voltages of $\pm$ 9 and $\pm$ 90 V. The conditions were: 4 mJ/pulse $F_{CF_3I} = 4 \times 10^{15}$ s^{-1}, $f = 12\%$, delay between IR and dye laser pulse was 3 μs.
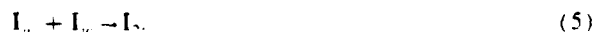
due to the larger collection times. The signals obtained using the larger collection voltages were analyzed with a boxcar integrator (5 μs gate width and delay). The signal from the boxcar was calibrated in terms of the number of ion and electron pairs produced per dye laser pulse based on the amplifier gain and the relationship between the peak height and total area of the time-dependent signal. A boxcar signal of 1 mV represented 4300 ion/electron pairs. Shot-to-shot variations in the pulse energies of both lasers limited our sensitivity to 0.1 mV (S/N = 1).

The visible radiation for the multiphoton ionization process was generated by an excimer laser (Lumonics Hyperex 460 operated at 351 nm) pumped dye laser (Lambda Physik FL2002), generating up to 8 mJ per pulse. The IR radiation was generated by a Tachisto CO_2-TEA laser (model 555) with pulse energies up to 1 J at the $R(12)$ or $R(16)$ line of the 9.6 μm band. Repetition rates were between 10 and 20 pps, and the delay time between the atom generating IR laser and the probe dye laser was varied using a digital delay generator. Scanning of the delay time with respect to the IR laser pulse resulted in the display of the temporal evolution of the REMPI signal. The visible laser focus (70 mm $f.l.$ lens) was positioned in the center of the IR-laser beam (cross sectional area of 1 cm^2).

RESULTS

CF$_3$I

The significant chemical reactions for the IRMPD of CF$_3$I are

$$CF_3I + nh\nu \rightarrow CF_3 + I, \qquad (1)$$

$$CF_3 + CF_3 \rightarrow C_2F_6, \qquad (2)$$

$$CF_3 \rightarrow \text{escape or wall loss}, \qquad (3)$$

$$I \rightarrow \text{escape or wall loss}, \qquad (4)$$

$$I_a + I_a \rightarrow I_2. \qquad (5)$$

I_a is an iodine atom absorbed on a surface. The initial collisionless IRMPD occurs in the irradiated volume ($V_h = 20$ cm^3) on the time scale of the pulse duration. In contrast to previous studies.[9,11] we are able to monitor the I-atom gener-

ation during the IR-laser pulse, as well as after the pulse, because our irradiation conditions ($\leqslant$ 1 J/cm^2) do not lead to ac Stark shifting of the atom REMPI signals. The radical species and hot parent molecules, whose energy content is below the threshold for unimolecular decomposition, then mix throughout the cell volume ($V_c = 620$ cm^3) on a time scale related to the molecular velocity and the dimensions of the cell (see below). Species with high sticking coefficients on the cold cell walls ($>$ 0.1) are lost in this early period. Vibrationally excited species are thermalized after a small number of wall collisions. Thermal accommodation coefficients are typically greater than 0.1. The process of thermalization and mixing to form a uniform density in the cell is complete after several hundred μs. The species then undergo the reactions listed above until the next IR-laser shot occurs in 50 or 100 ms.

In previous[14] modulated molecular-beam mass spectrometry studies of the type represented by Eqs. (1)–(5), only the stable products were monitored, and the key transient densities were inferred from the yields of the stable products. The application of REMPI to the study of these systems under the same reaction conditions is a major refinement of the experimental technique and allows for the direct observation of the reaction intermediates and the confirmation of the assumed reaction scheme.

CF$_3$I spectra and time dependence

The REMPI spectra of CF$_3$I has been studied under a variety of conditions in the wavelength range 460 to 490 nm (coumarin 480 dye). The spectra at 0.8×10^{-3} Torr of CF$_3$I are shown in Fig. 2 for the background (no IR laser) and two delay times. The IR laser was operated at 10 Hz and provided a CF$_3$I steady-state depletion (measured using the mass spectrometer) of 16%. The main difference between these two delay times is that at 0.3 μs the low-intensity tail of the IR pulse is still present and decomposition is still occurring. The species that are present in the probe volume at both of these early times are precursor gas molecules (thermal or vibrationally excited), stable product molecules from previous IR laser shots, and the nascent products of the decomposed CF$_3$I. Also shown in Fig. 2 are the expected wavelengths[1] for the multiphoton ionization of CF$_3$, ground-state iodine [I $5p^5(^2P_{3/2})$], and the spin–orbit excited state [I* $5p^5(^2P_{1/2})$].

In the following sections, the five major peaks in the REMPI spectra are identified by wavelength and temporal behavior. Two of the peaks are identified as resulting from the ionization of I through three-photon resonant states $6s(^2P_{1/2})$ at 474.8 nm and $6s(^4P_{3/2})$ at 485.3 nm. These features were also seen by Hackett et al.,[8] in a focused CO_2-laser IRMPD experiment. Both lines are asymmetric and blue degraded, which is an indication of ac Stark broadening.[16] Also, the 485.3 nm peak shows a spike on the red edge, reminiscent of the sharp features in the REMPI spectra of Ba that have been analyzed in terms of channel interference effects by Kelly, Hessler, and Alber.[17] The narrow width of this peak suggests that it may not simply be the [4 - 1] REMPI feature expected at this wavelength.[11] Both of these features are present in the background spectrum to a lesser
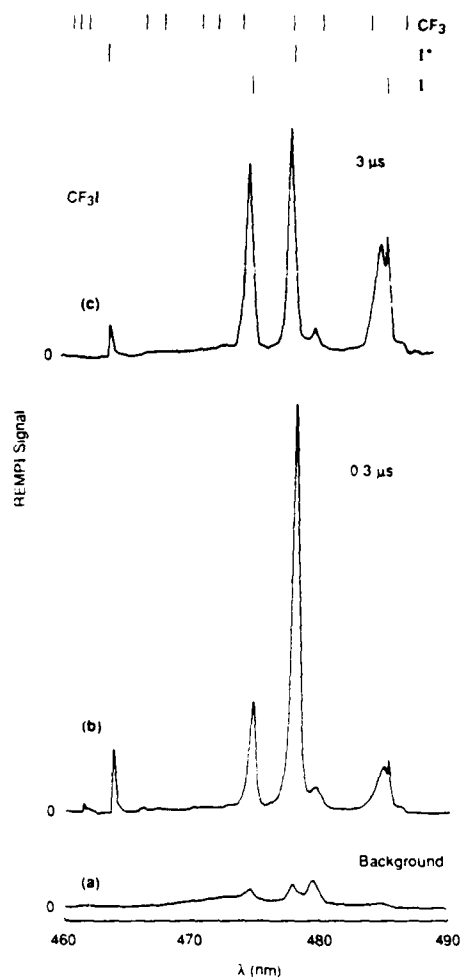
FIG. 2. REMPI spectra of CF_3I: (a) background (IR laser off); (b) IR laser on, probe laser delayed by 0.3 μs; (c) IR laser on, probe laser delayed by 3 μs. $P = 0.8 \times 10^{-1}$ Torr, $f = 16\%$, dye laser energy of 5.5 mJ/pulse.

constant within experimental uncertainty until the next laser pulse. For the two lower fluence cases, the difference signal rises during the first few microseconds and then gradually falls to zero. The constant portion of the signal at late time for the high fluence case is due to a stable product of the IRMPD induced chemistry I_2, whose presence we detect by mass spectrometry. We do not expect REMPI signals due to the molecular ion I_2^- in this wavelength range because all accessible electronic states[21] of I_2 at the two-photon level are predissociative leading to I and I*. At late times, i.e., at several ms, essentially no difference signal is observed for the two lower fluence cases because there is no significant build up of I_2. The REMPI signals at early time, late time, and without the IR laser all show a third-order formal intensity dependence on dye laser pulse energy with a slight turnover toward saturation at 5 to 6 mJ/pulse.

There are two sources of the difference signal at early times before any collisions occur: I generated from IRMPD of CF_3I and I generated by visible single-photon excitation and predissociation of the "hot" CF_3I prepared by IR excitation. The existence of the second mechanism is shown by previous experiments[19,20] that showed a dramatic long wavelength shift in the UV absorption spectra with internal energy. Also, it will be shown below that this second mechanism must be occurring to explain our REMPI observations of I*.

Two peaks in the REMPI spectrum of Fig. 2 arise from the ionization of I* through three-photon resonant states 7 $s(^2P_{3/2})$ at 463.7 nm and 6 $s(^2S_{1/2})$ at 478.1 nm. The more intense peak has the characteristic line shape due to ac Stark broadening. The peak at 463.7 nm is weaker because of probe laser energy limitations in this wavelength range but nevertheless shows the same broadening and temporal dependence as the strong peak at 478.1 nm. In analogy with the ground-state I-atom REMPI signal discussed above, the origin of the REMPI signal corresponding to I* in the CF_3I background spectrum [Fig. 2(a)] is due to two-photon dissociation and subsequent ionization by the probe laser pulse.

In Fig. 3 the time dependence of the REMPI difference signal for I* is shown for three values of the IR–laser fluence. This signal was monitored at 477.8 nm, shifted 0.3 nm due to the Stark effect. At the two low fluences, the REMPI difference signal rises in the first few μs and then gradually decreases to zero in analogy to I atom REMPI discussed above. At the highest laser fluence the signal rises to a maximum at about 0.5 μs then sharply decreases over the next 1 μs. After this early period the signal behaves similarly to the 474.5 nm REMPI signal due to ground state I, decreasing gradually to 1 ms and then remaining constant until the next laser shot. The late time constant signal is due to I_2, as discussed above for I. The origin of the large REMPI difference signal in the collisionless regime (a few μs after IR excitation) is due to I* generated by visible single-photon decomposition of IR-laser excited CF_3I. At the highest IR fluence the 477.8 nm REMPI signal increases during the first 0.5 μs as the average internal energy of CF_3I increases due to IR pumping. The signal then decreases over the next 2 μs as excited CF_3I continues to decompose during the duration of the IR laser pulse. For the lower IR-fluence conditions we only observe an increase in REMPI signal as the CF_3I heats up with very

extent, where they are thought to result from I produced by the visible two-photon excitation of CF_3I into the predissociative molecular state with ensuing rapid decomposition into CF_3 and iodine atoms (I and I*).[18] Single-photon dissociation is unlikely for ground-state CF_3I because of the low absorption of CF_3I in this wavelength range.[19,20] The width of the REMPI lines are broader than the probe laser bandwidth (0.2 cm^{-1}) and are apparently due to ac Stark broadening by the focused dye laser and not by the (unfocused) IR irradiation. This conclusion also follows from a comparison of the peak widths of the REMPI spectrum of CF_3I with and without ("background" spectrum in Fig. 2) IR-laser irradiation.

The difference signal (IR laser on minus IR-laser off) of the I feature at 474.5 nm versus the delay time of the probe laser pulse is shown in Fig. 3 for the three IR laser fluences of 1.34, 0.67, and 0.22 J cm^{-2}, with parent gas depletions of 16%, 4%, and < 1%, respectively. The REMPI signal was taken at the peak of the line with a wavelength of 474.5 nm, 0.3 nm to the blue of the expected wavelength. At the highest fluence, the signal rises during the first few μs, decreases gradually during the next few hundred μs, and then remains
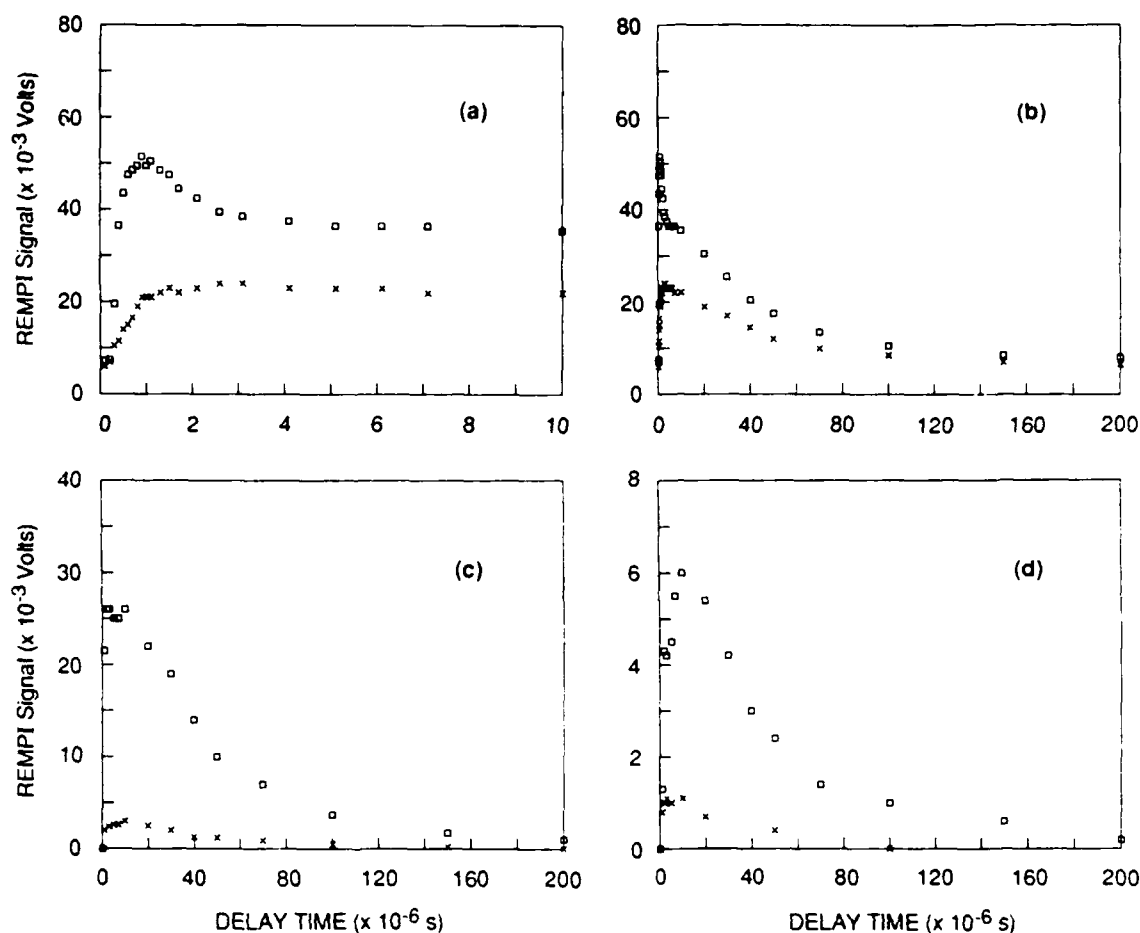
FIG. 3. REMPI difference signals (IR laser on minus IR laser off) for I (474.5 nm, ×) and I* (477.8 nm, boxes) vs probe laser delay. (a) and (b) IR laser fluence Φ_0 of 1.34 J cm^{-2}, $f = 16\%$; (c) Φ_0 of 0.67 J cm^{-2}, $f = 4\%$; (d) Φ_0 of 0.22 J cm^{-2}, $f < 1\%$. $F_{CF_3I} = 4 \times 10^{15}$ s^{-1}, 6 mJ/pulse dye laser energy, 11 pps.

little IRMPD occurring. Contrary to the report by Boriev et al.,[22] we do not believe that I* can be generated from the IRMPD of CF_3I because the threshold energy for this process is significantly higher (by 7600 cm^{-1}) than for I. In agreement with REMPI signals for I, the I* REMPI signal followed a third-order formal intensity law as a function of dye-laser pulse energy under all experimental conditions.

The REMPI signal at 479.6 nm in Fig. 2 is assigned to an unspecified resonance of the CF_3I molecule. Its wavelength position does not correspond to either an I or I* resonance. Furthermore, the signal decreases when the IR laser is turned on, and the short time delay signal is smaller than at long delay times. Thus, this signal cannot be due to CF_3 or any other product formed by IRMPD of CF_3I. We also note that the peak shape is symmetric in contrast to the Stark shifted lines discussed above.

CF_3Br spectra

The REMPI spectrum of CF_3Br has been studied using focused and unfocused CO_2 laser radiation. Focused IR radiation was used to achieve higher degrees of decomposition of the parent gas in the focal volume. Under these circumstances, it was necessary that the focus of the dye laser be

located in the focal volume of the CO_2 laser. The spectra for both conditions are shown in Fig. 4 along with a background spectrum. Also shown in Fig. 4 are the wavelengths[15] where REMPI signals are expected for CF_3, ground-state Br($^2P_{3/2}$) and excited-state Br, Br*($^2P_{1/2}$).

The only strong REMPI signal seen under focused CO_2 laser conditions is identified as the [3 + 2] REMPI of the ground-state Br through the $5s(^4P_{3/2})$ state at 462.3 nm. As for I atom REMPI, the atomic resonance is considerably broadened and Stark shifted.[16] The absence of a peak at 473 nm corresponding to the [3 + 2] REMPI via the resonant $^4P_{5/2}$ state in Br is due to the low probe laser power for the experimental conditions of Fig. 4. In a scan with a different dye (coumarin 480), a weak signal was observed at 473 nm but was not studied in detail. The absence of the REMPI signal at 459.6 nm corresponding to [3 + 2] REMPI of Br in the upper spin state via the resonant $5s$ $^2P_{1/2}$ state can be explained by the fact that the focused IR radiation bleaches the probed volume thus photolyzing all irradiated CF_3Br molecules. In this case, no vibrationally excited CF_3Br molecules remain that could undergo single-photon dissociation with subsequent [3 + 2] REMPI of Br*, in complete analogy to the experimental situation of Hackett and co-workers[4]
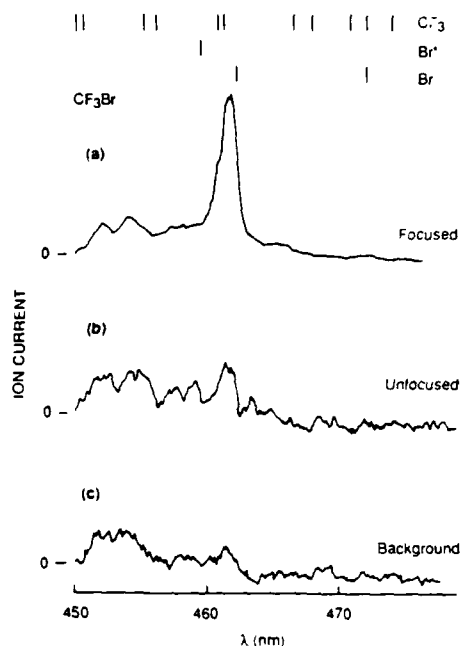
FIG. 4. REMPI spectra of CF_3Br: IR laser off, collimated, and focused. The delay time for the probe laser was 3 μs. The expected line positions for CF_3, Br, and Br* are shown at the top of the figure.

for the case of CF_3I. The absence of strong REMPI signals due to CF_3 free radicals is apparently due to the large background signal from CF_3Br REMPI.

In the spectrum obtained with the collimated IR-laser beam the line at 462.3 nm for Br is weaker because the extent of CF_3Br depletion is smaller. We find a small signal at the wavelength expected for REMPI of Br* under collimated IR-laser conditions. In the background spectrum for CF_3Br, we observe the signal for the ionization of Br and Br* albeit at reduced signal to noise. As in CF_3I, the halogen atoms can also be generated by visible two-photon dissociation of CF_3Br as observed in the background spectrum of Fig. 4.

DISCUSSION

Since we use the REMPI signal at 474.5 nm as a measure of the density of the ground-state I atom, and since we use the time history of this signal to extract both sticking coefficient and ionization efficiency, we begin with the justification of the assignment of the REMPI signals. From the discussion of the IR fluence and time dependence in the previous section, it is apparent that the difference REMPI signal at 474.5 nm monitors the density of I atoms formed by IRMPD: whereas the corresponding signal at 477.8 nm monitors the vibrationally excited parent molecule CF_3I. From the literature, two facts are known with certainty: First, the absorption spectrum of CF_3I strongly shifts towards the red upon internal excitation[19,20] such that IR-multiphoton excited CF_3I decomposes upon single-photon absorption around 475 nm. Second, the quantum yields for I* generation following predissociation via the A state has been measured for a great number of generic alkyliodides with increasing accuracy[21,24] and is 0.92 for CF_3I.[18]

The quantum yield changes with excitation wavelength, e.g., it drops from 1.0 to 0.6 from 300 to 336 nm for C_3F_7I. Although this behavior has not been established for CF_3I, it is very likely that it is similar in light of a recent investigation of the composite nature of the A state in CF_3I by Van Veen.[18] Because the quantum yield of I is small and does not change significantly with excitation wavelength, we interpret the time dependence of the REMPI signal at 474.5 nm during the IR-laser pulse as reflecting the kinetics of formation of I atom from IRMPD of CF_3I with essentially no interference from the complicating contribution of hot CF_3I under high IR-laser fluence conditions. We further justify this conclusion by the fact that the REMPI signal at 474.5 nm and under conditions of high IR-laser fluence, does not show the characteristic rise and fall during the IR-laser pulse exhibited by the REMPI signal at 477.8 nm. This latter originates from a single process, which is photodissociation of vibrationally highly excited CF_3I. On the other hand, the signal at 474.5 nm is a superposition of REMPI signals of ground-state I atoms from both IRMPD of CF_3I and single-photon dissociation[18] of CF_3I^* (~8%). The small contribution from the latter can also be seen when one considers the small REMPI signal amplitude at 474.8 nm when the IR fluence is low and the IRMPD yield is vanishingly small. The ratio of REMPI signals at 477.8 and 474.5 nm further demonstrates the small I atom yield from the single-photon dissociation of CF_3I^* [Figs. 3(c) and 3(d)].

The rise and fall of the REMPI signal at 477.8 nm within the IR-laser pulse is due to the fact that the IR-pumping process generates hot CF_3I and also causes its loss upon further pumping by IRMPD. The temporal behavior of this REMPI signal is thus dependent upon IR-laser fluence. At low fluence, where no decomposition takes place, the signal reaches a constant level, whereas under conditions of significant IRMPD [16%, Fig. 3(a)] the REMPI signal decreases substantially due to depletion of the pool of reacting molecules. It is not straightforward to model the time dependence of this REMPI signal, because it depends not only on the resonant ionization of I, but also on the single-photon dissociation of hot CF_3I that has not been studied in detail. Moreover, there exists the distinct possibility that the branching ratio is dependent on the internal energy of CF_3I which by itself could lead to a time dependence such as presented in Fig. 3 for the 477.8 nm REMPI signal. The reason we give only a qualitative explanation at this point is the fact that REMPI of CF_3I^* (hot) is a complex process which depends on the properties of the hot precursor and its photodissociation product.

Thus far only the short time dependence of the REMPI signal within the IR-laser pulse has been discussed. Both the irradiated (hot) molecules, as well as the photoproducts formed within the irradiated volume up to the end of the collisionless IRMPD expand into the rest of the Knudsen cell, which has a ratio of 31:1 in terms of total volume to irradiated volume. This decrease of the original density of transient species is described by the temporal dependence of the REMPI signal on the time scale of several hundred μs. The decay constant k_d is given by Eq. (6) assuming Maxwellian flow at ambient temperature, which is expected to

hold for the present case of a simple bond fission reaction, under conditions of negligible translational energy release:

$$k_d = (3\langle v \rangle)/4R. \tag{6}$$

$\langle v \rangle$ is the molecular velocity and R is the radius of a sphere of irradiated molecules. This equation also holds[25] for cylindrical geometry of a cylinder of radius R and length $2R$. It is important to describe this relaxation to homogeneous density throughout the reactor in analytical terms in order to separate the heterogeneous interaction from homogeneous mixing. If this separation of kinetic processes cannot be achieved, we would be unable to obtain quantitative results for the heterogeneous interaction of the transients with the cell walls. One of the conditions where this separation would not be possible corresponds to the situation where the sticking coefficient γ is on the order of 0.3, in which case the rate of the heterogeneous reaction is faster or of the same magnitude as the rate of homogeneous mixing. Experimentally, this separation of kinetic processes into two distinctly different time domains manifests itself in a break of a logarithmic plot of the transient density vs time. The faster decay process pertains to k_d, whereas the slower process obtains the rate constant for the heterogeneous interaction, which is the quantity of interest.

Table I presents our data in terms of observed and calculated k_d values with the above justified assumption that the REMPI signal at 474.5 nm and high IR–laser fluence is due to the I atom, whereas all other experimental situations at both 474.5 and 477.8 nm correspond to CF_3I^+ (i.e., $\langle v \rangle$ is calculated using the mass of I or CF_3I). Row (a) in Table I corresponds to high IR–laser fluence with concomitant 16% IRMPD, whereas row (b) corresponds to low IR–laser fluence with essentially no IRMPD, hence no I-atom formation. We note the close agreement between observed and calculated decay rate constants which also supports our contention that the I-atom contribution probed at 474.5 nm in the single-photon dissociation of CF_3I^+ is small. This supports our suggestion regarding the REMPI signal intensity at 474.5 nm at high IR fluence as representative of the I-atom density.

Sticking coefficient

Since Eq. (6) describes the homogeneous mixing process adequately, we will now discuss the I-atom density as a function of time after homogeneous mixing has been achieved. Various chemical and physical processes can take place after this mixing process is completed, and when one compares the REMPI signal at 474.5 vs 477.8 nm, we obtain a first-order loss rate constant k_w for I-atom loss of 77 and 407 s^{-1}, respectively, under two sets of conditions from two separate experiments. These values are approximate because

	k_d^{474}	k_d^{474} (calc)	k_d^{477}	k_d^{477} (calc)
(a)	2.7 ± 0.5	3.0	2.3 ± 0.2	2.4
(b)	2.3 ± 0.3	2.4	2.3 ± 0.3	2.4

the present cell does not have the required sensitivity to measure this quantity with high accuracy due to the small irradiated volume with respect to the total cell volume. The REMPI signal at 477.8 nm representing CF_3I^+ vanishes after several hundred μs indicating that the sticking coefficient for hot CF_3I is $\geqslant 0.3$. We relate our measured quantity k_w to γ by dividing it by the gas-wall collision frequency $\omega = 4240 \times (T/M)^{1/2}$ resulting in values of 1.2×10^{-2} and 6.2×10^{-2}, respectively.

Houston and co-workers have studied the vibrational relaxation of vibrationally excited CO_2 on Ag and other surfaces[26] and have related k_w to the surface deactivation probability γ using Eq. (7):

$$\gamma = 1 - \exp(-k_w d/\langle v' \rangle), \tag{7}$$

where $\langle v \rangle$ is the two-dimensional molecular velocity and d is the cell diameter (6.3 cm). Using Eq. (7), we obtain essentially the same values for γ of I as above.

There is no doubt that k_w corresponds to adsorption of atomic I on the walls of the reaction vessel of which 90% are gold, along with some quartz and KCl windows for laser beam throughput. Even though our surfaces are not well characterized at this point our γ values give a useful range for this important parameter. The reason for attributing k_w to a heterogeneous process is the fact that homogeneous recombination of I at those pressures is very slow. With a third-order (homogeneous) rate constant for I recombination[27] (I_2 as third body) of 8.3×10^{-32} cm^6 s^{-1}, we calculate an effective first-order recombination rate constant of 1.5×10^{-4} s^{-1}, which is five to six orders of magnitude slower than the measured decay rate constant for I disappearance in our cell. It therefore appears reasonable to identify this loss process as a heterogeneous process.

We also observe I_2 in the cell some time after the onset of IRMPD, but we cannot determine the branching ratio for I_2 formation. A hint that not all I atoms adsorbed on the gold surface recombine to I_2 is the fact that we observe CF_3I by mass spectrometry upon IRMPD of hexafluoroacetone in the cell that had been exposed previously to IRMPD of CF_3I, hence to a healthy I-atom flux. This also means that the present surface has the ability to "store" I atoms that recombined with CF_3 radicals in a heterogeneous manner after the cell had been pumped out overnight between the CF_3I and the hexafluoroacetone IRMPD experiment.

Relative ionization efficiency

Relative or absolute ionization efficiencies of I atoms can be determined if the density of I and the REMPI signal intensity are known. The density of I generated in the IR beam volume is given by Eq. (8):

$$[I] = fF_{CF_3I} t_p/V_b, \tag{8}$$

where t_p is the period of the laser, f the fractional decomposition, F_{CF_3I} the flow rate of CF_3I, and V_b the originally irradiated beam volume. For the highest fluence data in Fig. 3(a), we calculate a density of I in the IR beam of 2.9×10^{12} cm^{-3}.

At high IR fluence, the early time increase in the REMPI signal at 474 nm is primarily due to IRMPD. There-
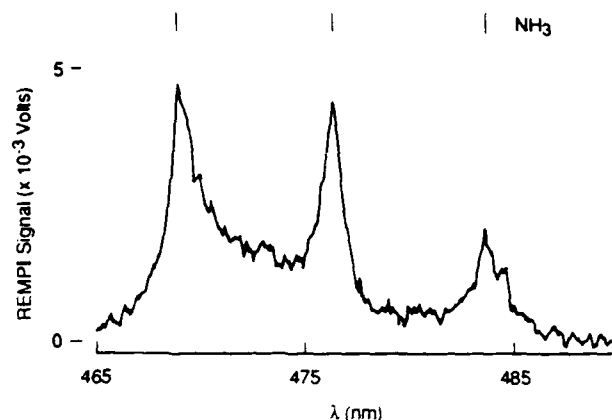
FIG. 5. REMPI spectrum of NH_3 at $0.5 \cdot 10^{-5}$ Torr, 8 mJ/pulse, and 11 pps.

fore, we can assess the amount of signal that is due to I atoms from IRMPD (23–7 mV). We determine the relative ionization probability using NH_3 as a standard that also has [3 + 2] REMPI signals with the same formal intensity law as I,I* in this wavelength region.[28] A REMPI spectrum of NH_3 is shown in Fig. 5. Using the REMPI signal at 476 nm (4.5 mV), the ratio of ionization probabilities is given by Eq. (9):

$$\frac{\text{Prob}(I)^{474.5}}{\text{Prob}(NH_3)^{476}} = \frac{\text{Sig}_{ion}/[I]E_{pulse}^3}{\text{Sig}_{ion}/[NH_3]E_{pulse}^3}. \tag{9}$$

The quantities in this expression are easily determined for our conditions resulting in an I atom ionization probability of 48 at 474.8 nm relative to NH_3 ionization at 476 nm in a [3 + 2] fashion.

[1] K. C. Smyth and P. H. Taylor, Chem. Phys. Lett. 122, 518 (1985).
[2] M.-S. Chou, Chem. Phys. Lett. 114, 279 (1985).

[3] T. A. Spiglanin, R. A. Perry, and D. W. Chandler, J. Chem. Phys. 87, 1568 (1987).
[4] J. H. M. Bonnie, E. H. A. Granneman, and H. J. Hopman, Rev. Sci. Instrum. 58, 1353 (1987).
[5] J. S. Hayden and G. J. Diebold, J. Chem. Phys. 77, 4767 (1982).
[6] E. E. Marinero, C. T. Rettner, and R. N. Zare, J. Chem. Phys. 80, 4142 (1984).
[7] M. T. Duignan, J. W. Hudgens, and J. R. Wyatt, J. Phys. Chem. 86, 4156 (1982).
[8] P. A. Hackett, P. John, M. Mayhew, and D. M. Rayner, Chem. Phys. Lett. 96, 139 (1983).
[9] D. M. Rayner and P. A. Hackett, Chem. Phys. Lett. 110, 482 (1984).
[10] M. Quack, E. Sutcliffe, P. A. Hackett, and D. M. Rayner, Faraday Discuss. Chem. Soc. 82, 229 (1986).
[11] D. M. Rayner and P. A. Hackett, Isr. J. Chem. 24, 232 (1984).
[12] R. M. Robertson, D. M. Golden, and M. J. Rossi, J. Vac. Sci. Technol. A (accepted); J. Phys. Chem. (submitted).
[13] T. E. Adams, R. J. S. Morrison, and E. R. Grant, Rev. Sci. Instrum. 51, 141 (1980).
[14] N. Selamoglu, M. J. Rossi, and D. M. Golden, Chem. Phys. Lett. 124, 68 (1986).
[15] C. E. Moore, Atomic Energy Levels, Natl. Stand. Ref. Data Ser. Natl Bur. Stand. No. 35 (U.S. GPO, Washington, D.C.,1971), Vols. 2 and 3.
[16] V. N. Bagratashvili, S. I. Ionov, G. V. Mishakov, and V. A. Semchin, J. Opt. Soc. Am. 4, 129 (1987).
[17] J. F. Kelly, J. P. Hessler, and G. Alber. Phys. Rev. A 33, 3913 (1986).
[18] G. N. A. Van Veen, T. Baller, A. E. DeVries, and M. Shapiro, Chem. Phys. 93, 277 (1985).
[19] H. Pummer, J. Eggleston, W. K. Bischel, and C. K. Rhodes, Appl. Phys. Lett. 32, 427 (1978).
[20] I. N. Knyazev, Yu. A. Kudryavtsev, N. P. Kuzmina, and V. S. Letokhov, Sov. Phys. JETP 49, 650 (1979).
[21] R. S. Mulliken, J. Chem. Phys. 55, 288 (1971).
[22] I. A. Boriev, A. M. Velichko, E. B. Gordon, A. A. Nadeikin, A. I. Nikitin, and V. L. Talroze, JETP Lett. 37, 259 (1983).
[23] J. E. Smedley and S. R. Leone, J. Chem. Phys. 79, 2687 (1983).
[24] W. P. Hess, S. J. Kohler, H. K. Haugen, and S. R. Leone, J. Chem. Phys. 84, 2143 (1986); W. P. Hess and S. R. Leone, ibid 86, 3773 (1987).
[25] H. Loehmannsroeben, K. Luther, and M. Stuke, J. Phys. Chem. 91, 3499 (1987).
[26] J. Misewich, C. N. Plum, G. Blyholder, P. L. Houston, and R. P. Merrill, J. Chem. Phys. 78, 4245 (1983); J. Misewich, P. L. Houston, and R. P. Merrill, ibid 82, 1577 (1985).
[27] J. Troe, Annu. Rev. Phys. Chem. 29, 223 (1978).
[28] J. H. Glownia, S. J. Riley, S. D. Colson, and G. C. Nieman, J. Chem. Phys. 73, 4296 (1980).

Appendix E

REACTION PROBABILITY FOR THE SPONTANEOUS ETCHING
OF SILICON BY CF_3 FREE RADICALS

Reaction probability for the spontaneous etching of silicon by CF₃ free radicals

Robert M. Robertson,[a] David M. Golden, and Michel J. Rossi
Department of Chemical Kinetics. Chemical Physics Laboratory. SRI International, Menlo Park. California 94025

The spontaneous thermal etching of silicon by CF_3 free radicals has been studied in a very-low-pressure photolysis reactor. The radical is produced by infrared multiphoton dissociation of either hexafluoroacetone or CF_3I, and is allowed to react with a temperature-controlled silicon sample (560–745 K). Mass spectrometry is used to measure the extent of dissociation of the precursor gas and the formation of product molecules, C_2F_6 and SiF_4. The etch rate of the silicon is determined from the SiF_4 production. Resonance-enhanced multiphoton ionization of CF_3 is used to determine the density and time history of the radical in the reactor. The measurements of the etch rate and CF_3 density are combined to derive the reaction probability. CF_3 etches silicon much more slowly than F atoms and at a rate comparable to molecular F_2. A carbon layer, that is deposited on the silicon by the radicals, inhibits, but does not stop, further etching. Experiments on the etching of silicon by F_2 were performed both to validate the reactor design and to prepare the silicon surface for the CF_3 studies.

I. INTRODUCTION

The chemical and physical processes that occur in the fluorocarbon discharges used to etch Si and SiO_2 are very complex. However, general trends and mechanisms have been identified[1] based on many careful empirical and fundamental studies. Since CF_3 is the subject of this paper, we briefly summarize the role CF_x radicals play in these discharges. The CF_x free radicals are formed primarily through electron impact events and are lost by gas or surface reactions. In CF_4/O_2 discharges, the CF_x radicals can react with O and O_2 to produce atomic fluorine and the stable products CO, CO_2, and COF_2. This results in a fluorine-rich discharge and selective etching of Si. In CF_4/H_2 discharges, F atoms are depleted by reactions to form HF, thus, leaving the CF_x radicals to dominate the neutral gas and surface processes. This results in a fluorine-deficient discharge that selectively etches SiO_2. The CF_x radicals can cause buildup of fluorocarbon films on all surfaces in the discharge chamber, the thickness and properties of which depend on the balance of adsorption and desorption processes (recombination or ion bombardment). Fluorocarbon films on Si decrease the etch rate and can contribute to the anisotropy of etching, whereas, on SiO_2 the etch rate does not decrease because the CF_x radicals or film contribute F to remove the silicon and C to remove oxygen.

Mass spectrometry, surface diagnostics,[2,3] and optical diagnostics[4] on discharges support these trends, as do computer simulations.[5] However, our understanding of these complex systems must be considered to be tentative and limited until detailed information on more of the primary processes and reactions are available. This detailed information can be gained from further empirical discharge studies or through isolated studies of individual reactions and processes. In this paper, we report on one such isolated study, the reaction of CF_3 on silicon.

The CF_x radical–surface reactions are also important in laser-enhanced etching processes. Steinfeld et al.[6] observed the etching of SiO_2 by CF_3Br, illuminated by an IR laser parallel to the surface and argued that the CF_3 radical was causing the etching. Loper and Tabat[7,8] used a UV laser incident to the surface to study the etching induced by several gases. Fluorine atoms generated from COF_2 etched Si but not SiO_2. CF_2 formed from CCl_2F_2 etched SiO_2, but CF_3 produced from hexafluoroacetone, CF_3I, CF_3Br, and CF_3NO did not. In a similar study using UV-laser radiation incident to the surface, Brannon[9] concluded that CF_2 etches glass and CF_3 does not. Using 193-nm laser radiation, CF_3Br did etch silicon, while the radicals produced from CF_2Cl_2 did not. These studies, while less complex than discharges, have not yet been carried out in sufficient detail for basic kinetic information to be gained. Information on elementary reaction steps will help to explain these systems as well.

More direct surface experiments have also been done that do provide basic information on the CF_x surface reactions. Winters[10] determined that CF_x radicals have large sticking coefficients on clean silicon. Roop et al.[11] determined that CF_3 is strongly adsorbed on Si and at least partially dissociates. In a follow-up study, Joyce et al.[12] further investigated CF_3 on Si and SiO_2, finding that CF_3 adsorbs less and does not dissociate on SiO_2. Thoman et al.[13] measured the sticking coefficient of CF_2 on silicon (2×10^{-2}). McFeely and Yarmoff[14] used synchrotron photoemission to study CF_3 on Si and SiO_2 and observed CF_3 reacting strongly on the former and weakly on the latter.

In this paper, we present results on the etching of Si by CF_3 free radicals. We operate the experiments in the param-
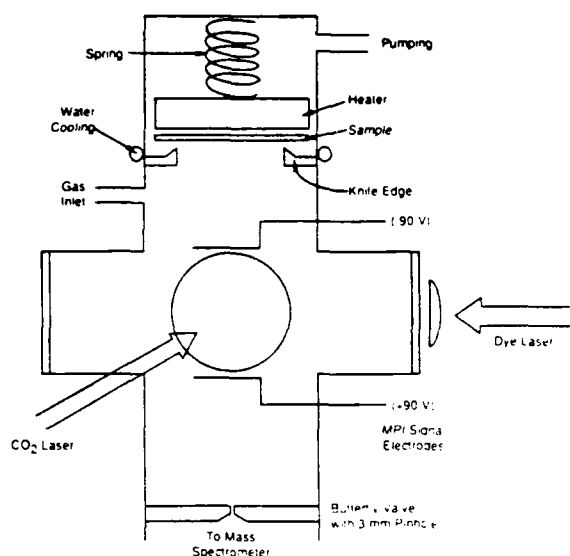
FIG. 1. Diagram of the VLPΦ reactor used to measure the etching of silicon by CF₃ free radicals. The reactor is a six-way stainless-steel cross. The top and bottom arms have 2½-in. inside diameters (4½-in. conflat), and the four side arms have 1½-in. diameters (2¾-in. conflat) The gas flows out of the reactor through the 3-mm aperture, and the back side of the sample is pumped separately

eter regime where measurable rates of etching occur and in which the kinetics of the CF_3 can be completely determined. In these very-low-pressure photolysis (VLPΦ) experiments, CF_3 radicals are created by the infrared-multiphoton dissociation (IRMPD) of hexafluoroacetone (HFA) or CF_3I and are allowed to react with a temperature-controlled silicon sample. Mass spectrometry is used to study the stable gas products that effuse from the cell, and resonance-enhanced multiphoton ionization (REMPI) is used to determine the density of CF_3 in the cell in real time. Results from previous VLPΦ experiments[15,16] with these precursor gases, but without a hot sample surface, are referenced in this paper.

II. EXPERIMENTAL

The reactor utilized in this series of experiments (Fig. 1) is a variation on the VLPΦ reactors that have been used in this laboratory for many years[17] to study gas reaction rates. It is a six-way stainless-steel cross that has been coated on the inside with gold by vacuum evaporation. The top and bottom arms are 2½-in. tubes (4½-in. conflat) and the four sidearms are 1½-in. tubes (2¾-in. conflat). Four sidearms hold the sapphire and KCl windows for the crossed visible and infrared laser beams, respectively. The bottom arm of the cell has a butterfly valve with an interchangeable aperture mounted in the center. With the butterfly valve fully open the reactor can be evacuated to a pressure of 2×10^{-7} Torr. With the butterfly valve closed, the aperture (3-mm diameter) controls the escape rate constant of the reactor and forms an effusive beam for the mass spectrometer. Also

attached to the reactor are two electrical feedthroughs for collection of the REMPI signal and two ¼-in. tubes for the gas-inlet flow and capacitance manometer pressure measurement.

The top arm of the reactor holds the high-temperature sample. In this arrangement, the sample is pressed down against a circular knife edge by a spring. The heater and thermocouple temperature sensors are located on the back side of the sample, which is evacuated separately. The knife edge and supporting flange are water cooled, so that the only hot surface that is exposed to the reactant gases is the sample. The leak rate of gases out of the main part of the reactor at the knife edge is small compared to the escape rate of gases through the exit aperture; we know this by monitoring the gas pressure on the back side and in the main reactor during the experiment. Also, we observe a distinct pattern of etching on the exposed part of the sample; after very long exposure the sample took on a nonreflecting gray color and had a noticeable edge where the knife edge pressed against the sample. There was no apparent etching on the parts of the sample that were outside of the knife edge. The samples used for this set of experiments were 2-in.-diam n-type silicon wafers with (100) orientation.

The volume of the reactor V_c was 620 cm³, the total cold wall surface area A_w was 720 cm², and the hot sample surface area A_s was 14.3 cm². With the 3-mm exit aperture, the measured escape rate constant was $k_e(M) = 0.24 \cdot (T/M)^{1/2}$, where T is the temperature in degrees Kelvin, and M is the atomic mass of a given species. The sample surface collision rate constant k_s is given by $1/4 v_{th} A_s / V_c = 84 \cdot (T/M)^{1/2}$. The cold wall collision rate constant, defined similarly, is $4330 \times (T/M)^{1/2}$. Because the sample surface is a small fraction of the total surface area the gas temperature and thermal velocity v_{th} will be determined by the cold wall temperature which was taken to be 300 K.

The IR radiation for the IRMPD of HFA was generated with a Tachisto CO_2 transversely excited atmosphere (TEA) laser, model 555. The $R(12)$ line of the 10.6-μm band was used for the HFA, and the $R(16)$ line of the 9.6-μm band was used for the CF_3I. The beam was reflected back through the cell to double the fluence and increase the extent of decomposition of the precursor gas. The pulse energy could be varied up to 1 J at repetition rates of 10 pps. The IR beam had a cross-sectional area of 1 cm² and a beam volume V_b in the reactor of 20 cm³. The visible radiation for the REMPI was generated by an excimer (Lumonics Hyperex 360, XeF at 351 nm) pumped-dye laser (Lambda Physik FL 2002). Pulse energies up to 20 mJ were available; however, the power was kept lower for the experiments in order to reduce photodecomposition of parent molecules. A 70-mm lens was used to place the visible laser focus in the IR-beam volume.

The REMPI signals were collected on two tantulum-wire loop electrodes located above and below the intersection of the two laser beams. The electrodes were held at a bias potential of ± 90 V for the collection of electrons and ions, respectively. The collected currents were amplified with a gain of 10⁷, then the signal from the electrons was inverted and added to the ion signal.[18] The total signal was then averaged with

a boxcar integrator and recorded on chart paper. The details of the REMPI system and ionization efficiencies have been discussed elsewhere.[15,16] For this experiment we only rely on the REMPI signals being linear in the gas density of the species to be ionized.

The effusive beam that is formed by the cell aperture passes through a differentially pumped section (14 cm) before reaching an aperture (0.7 cm) to the mass spectrometer chamber. Immediately behind this aperture is a 150-Hz tuning fork modulator. The modulated beam then travels an additional 4 cm to the ionizer of the quadrupole mass spectrometer (Balzers 311). Phase-sensitive detection is used to separate the background signal from the signal due to beam gases. Mass spectrometer signals at masses 38, 147, and 196 were used to monitor the precursor gases F_2, HFA, and CF_3I, respectively. The primary products, SiF_4 and C_2F_6, were monitored at mass peaks 85 and 119, respectively, and were calibrated with authentic samples. The SiF_4 isotope peaks at masses 86 and 87 were observed for etching with F_2 and CF_3 from the IRMPD of HFA.

III. RESULTS

Before discussing the results from CF_3 etching, we will present results from an experiment on silicon etching by F_2. This experiment was carrried out for two reasons. First, because this reaction has been studied previously,[19-21] we could test our apparatus and abilities to measure flows and temperatures accurately. Second was to prepare a consistent surface for the CF_3 experiments. The F_2 etching leaves behind a surface that is free of contaminants or of an oxide layer, the remaining surface will be a fluorinated silicon surface.[22]

A. F_2 etching of silicon

Figure 2 depicts the mass spectrometrically measured flows of F_2 and SiF_4 out of the reactor as a function of the temperature of the silicon sample. In these experiments, we use a mixture of 10% F_2 in He as our source of fluorine, and
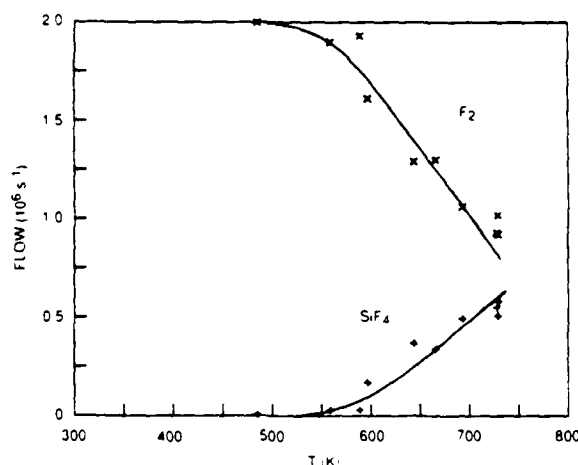
in the case shown, the pressure in the cell was 6.2×10^{-3} Torr. At increasing temperatures, the fluorine is being depleted and the rate of SiF_4 production increases. The etching of silicon by F or F_2 primarily produces SiF_4, so that the SiF_4 is an accurate measure of the amount of etching that has occurred. (SiF_2 is a minor product[20,23] and will react[24] with F_2 to form SiF_4 under our conditions.) Due to conservation of the total flow of fluorine through the cell, we expect that the decrease in the F_2 flow should be twice the increase in the SiF_4 flow, and this is observed.

In Fig. 3, the etch rate (in $Å$ min^{-1} $Torr^{-1}$ of F_2 initially present) is plotted versus the inverse temperature;

$$\text{etch rate} = F_{SiF_4} 6 \times 10^9 / A_i n_{Si} P_{F_2},$$

n_{Si} is the density of silicon 5×10^{22} cm^{-3}, and the factor of 6×10^9 is to convert the units. For a total pressure of 6.2×10^{-3} Torr the initial pressure of F_2 (P_F), was 1.58×10^{-3} Torr. The etch rate can be converted to monolayer $(ML) min^{-1} Torr^{-1}$ by dividing by the thickness of one monolayer (3.2 $Å$). The $\times$'s represent the data determined from the mass spectrometric determination of SiF_4 flow. The solid line represents data from Selamoglu et al.[19] Data from two other studies fall considerably below[20] and above[21] this line. Considering the unresolved discrepancies in the previously reported etch rates and the uncertainty of our data (especially at the three lowest temperatures), we consider our etch rate to be in good agreement with the previous studies. This agreement and the observed conservation of fluorine atom flow demonstrate that the reactor is performing as designed and that the mass spectrometer and temperature sensors are accurately calibrated.

Inhibition of Si etching by F_2 was observed under two conditions. Compared to the steady-state etch rate, a substantially smaller rate was observed when a Si wafer was initially placed in the reactor. This lower rate persisted until many monolayers of Si had been removed (as observed by monitoring SiF_4 flow from the reactor). This effect is due to

FIG. 2 The flow rates of F_2 and SiF_4 out of the reactor vs temperature of the Si sample. The F_2 was supplied as a 10% mixture in He, and the pressure in the reactor at 300 K was 6.2×10^{-3} Torr.
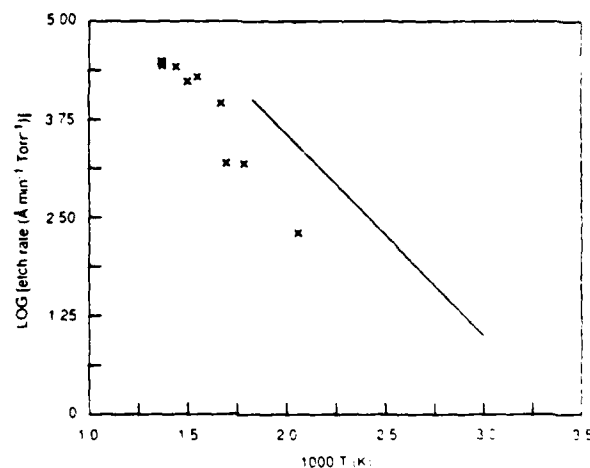
FIG. 3 The etch rate of Si by F_2 vs the inverse temperature of the Si sample. The etch rate is determined from the mass spectrometer measurement of the flow of SiF_4 out of the reactor. The etch rate reported by Selamoglu et al (Ref. 19) is shown for comparison (solid line)

a native oxide layer on the new sample. A smaller inhibition of the etch rate occurs when the wafer has been previously exposed to HFA. This is a minor effect, that disappears after a 20-min exposure to several mTorr of F_2. During this inhibition period, we observe fluorocarbon species (for instance, mass peak 69) coming out of the reactor, and we conclude that the effect is due to the buildup of a carbon layer during the exposure of the sample to HFA. We have not attempted to quantify the amounts of carbon that are left on the surface during the HFA experiments, but it is not surprising that one or several monolayers would be present, depending on the length of exposure. In one case, the etch rate by F_2 was decreased by more than a factor of 4 by the fluorocarbon film. This effect will be discussed below because it is also observed during the HFA IRMPD experiments.
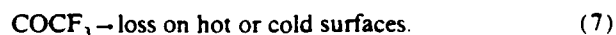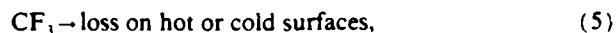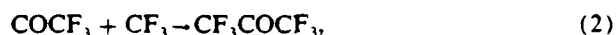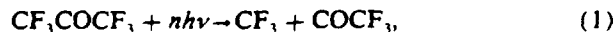
B. IRMPD and chemistry of HFA

The model of the pulsed-laser IRMPD in a flowing gas VLPΦ reactor has been discussed in detail in previous publications[15-17] and can be explained briefly with reference to the time scales involved. The IR-laser pulse has an initial intense spike that lasts for 200 ns followed by a low-intensity tail that decays in 2 μs. During the pulse, the precursor gas absorbs energy and undergoes collisionless unimolecular decomposition. Immediately after the pulse, the precursor and product molecules (in various states of vibrational excitation) are located within the volume defined by the laser beam. These species next diffuse out of the beam volume on a time scale (100 μs) determined by the thermal velocities of the molecules. Because the pressures are low, the mean free path for a gas–gas collision is longer than the dimensions of the reactor, and the molecules will experience more wall collisions than gas collisions. After several collisions (< 2 ms), the precursor and product molecules will have lost any of their initial vibrational excitation and will form a thermalized, uniform density in the reactor. For the remainder of the time until the next IR-laser pulse (100 ms) the thermalized precursor and product molecules undergo gas and surface reactions or escape from the reactor through the exit aperture. At the time of the next IR-laser pulse, the beam volume will primarily contain fresh precursor gas and smaller densities of stable and radical product molecules (that usually do not absorb the IR). The resulting time dependence of the gas densities appears as a sawtooth pattern.

The chemistry of HFA in the VLPΦ reactor at moderate IR fluences (< 2 J cm^{-2}) has been discussed in a previous paper[15] and is summarized in the following reactions:

$$CF_3COCF_3 + nh\nu \rightarrow CF_3 + COCF_3, \quad (1)$$

$$COCF_3 + CF_3 \rightarrow CF_3COCF_3, \quad (2)$$

$$CF_3 + CF_3 \rightarrow C_2F_6, \quad (3)$$

$$CF_3 \rightarrow escape, \quad (4)$$

$$CF_3 \rightarrow loss\ on\ hot\ or\ cold\ surfaces, \quad (5)$$

$$COCF_3 \rightarrow escape, \quad (6)$$

$$COCF_3 \rightarrow loss\ on\ hot\ or\ cold\ surfaces. \quad (7)$$

The initiating reaction [Eq. (1)] is the IRMPD of HFA, a simple bond scission process. The COCF$_3$ can react with

CF$_3$ [Eq. (2)], to reform the HFA or it will be lost in the first-order reactions of escape from the reactor or loss on hot or cold surfaces. The CF$_3$ radical can undergo the first-order losses k_1 of escape or loss on hot or cold walls. The other first-order loss of CF$_3$ is the reaction with COCF$_3$ [Eq. (2)]. The only other reaction of CF$_3$ is the second-order self-reaction to form C_2F_6. This reaction rate constant k_r has been studied[17] in this laboratory using VLPΦ, as well as by others. (Secondary reactions are not expected to occur under our conditions,[15] e.g., CF$_3$ + HFA.)

In previous IR and UV photolysis studies (for instance, Refs. 25 and 26 and references therein), the breakup of the perfluoroacetyl radical has been concluded to proceed rapidly by thermal or photoexcitation. Under our moderate IR fluence, the COCF$_3$ is stable and can recombine with a CF$_3$ [Eq. (2)]. The evidence for the stability of this radical comes from two mass spectrometer studies and has been discussed in a previous paper.[15] The yield of C_2F_6 per decomposed HFA is 1/2 (independent of the surface temperature) at the high-pressure limit where the second-order reaction [Eq. (3)] is dominant. In other words, two HFA molecules must be dissociated to produce the two CF$_3$ molecules that form C_2F_6. The second mass spectrometric test demonstrated that the net depletion of HFA [Eq. (1) minus Eq. (2)] decreases at high pressures and constant IR fluence. At constant fluence, we expect the rate of Eq. (1) to be proportional to the HFA pressure over our range of pressures. Thus, the decrease in net depletion must be due to the back reaction [Eq. (2)], which is only significant if the COCF$_3$ is stable. Also, the COCF$_3$ is not expected to decompose following the IRMPD of the HFA because there is a modest barrier.[27,28]

C. CF$_3$ etching of silicon

In this section, we will present the mass spectrometric measurements of the SiF$_4$ production as a function of time, pressure, and temperature. In these experiments, we examine the SiF$_4$ produced with the IR laser on and off. The SiF$_4$ produced when the laser is off is due to the dark reaction of HFA and will be discussed below. The difference between the SiF$_4$ produced with IR laser on and off is due to transient species produced by the IRMPD of the HFA and is the subject of this section.

The time dependence of the etching reaction is shown in Fig. 4. Here the mass spectrometer signal at mass peak 85 is shown versus time in minutes. The flow of HFA for Fig. 4(a) was 6×10^{16} s^{-1}, the extent of decomposition was 10%, and the sample temperature was 710 K. Prior to taking this time scan, the surface was etched with F_2, and the reactor was evacuated. In this time scan, we first turned on the IR laser, followed ~ 1 min later by the introduction of the HFA gas flow. We observe that SiF$_4$ is produced immediately after the gas is introduced into the cell. The SiF$_4$ gas flow rises to an initial high flow rate (corresponding to an etch rate of 0.35 ML/min) and then falls to a near-steady value (0.15 ML/min). After the IR laser is turned off, there is a small amount of SiF$_4$ produced by the thermal decomposition of the HFA.

In another time scan of this type, we first introduced HFA and then turned on the IR laser. For this situation, the slow
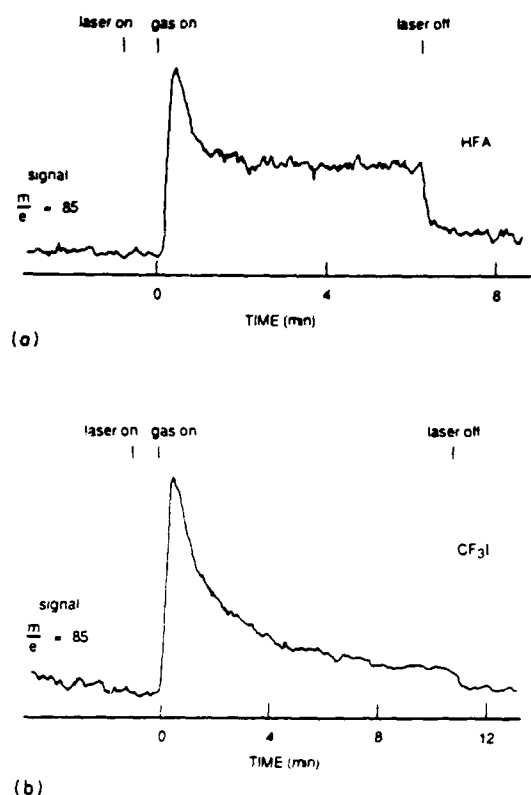
(a)

(b)

FIG. 4. The time dependence of the mass spectrometer signal at $m/e = 85$, representing the flow of SiF_4 out of the reactor: (a) the precursor gas was HFA and (b) CF_3I.

FIG. 5. SiF_4 production vs $f F'_{HFA}$. The flow of HFA was varied and the depletion was constant at 15%. The temperature of the sample was 718 K. The data fall along two lines depending on whether the surface had been exposed for long (~ 90 min) or short times (~ 20 min).

etching by the HFA alone began when the gas was introduced, and the rapid etching began after the IR laser was introduced. The time dependence after the IR laser was turned on was similar to that shown in Fig. 4. We conclude that the large increase in etching when the HFA and IR laser radiation are both present is due to a product of the IRMPD of the HFA. Second, we conclude that the observed time dependence is due to a variation in the character of the surface because the gas chemistry stabilizes within 30 s after the HFA and IR radiation are both present. This is demonstrated by the mass spectrometric measurements of HFA depletion and C_2F_6 formation.

In Fig. 4(b), we have displayed a similar time scan of the etching caused by IRMPD of CF_3I. The gas-phase kinetics of this system have been studied previously[16,17] and are well understood. The flow of CF_3I was 8×10^{15} s^{-1}, the extent of decomposition was 12%, and the sample temperature was 730 K. After both the gas and IR-laser radiation are present, the etching rate rises to an initial high value (0.30 ML/min) and then falls off to a near steady-state value (0.03 ML/ min). With the IR laser blocked, there is no etching from the CF_3I gas alone. The time dependence of the decrease in the etch rate using the CF_3I is markedly different than for the HFA. We do not have an explanation for this effect because not enough experiments have been done to isolate the cause. When we reversed the order in which the IR radiation and
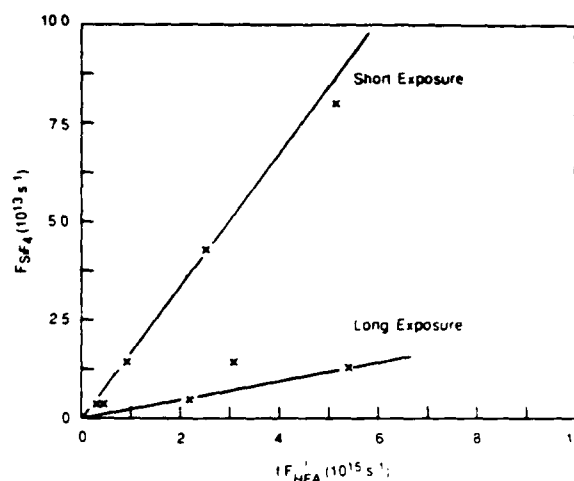
CF_3I gas flow were introduced, we observed, as with HFA, that both must be present for etching to occur. We again conclude that a product of the IRMPD of CF_3I is causing the etching and that the late time dependence is caused by changes in the surface rather than changes in the gas densities of the etching species.

Because the CF_3 radical is present in the IRMPD of both precursor gases and the initial etch efficiencies (see below) are comparable, we conclude that the CF_3 radical is primarily responsible for the etching. The decrease in etch rate with exposure time is an inhibition effect that we also observed with F_2 after HFA exposure, and we propose that it is caused by a carbon buildup on the surface.

A short-time inhibition effect is seen in Fig. 4. In Fig. 5, we see a long-time inhibition effect. In this figure, the increased SiF_4 flow (IR laser on minus IR laser off) is plotted versus the product of fractional depletion f and HFA flow F_{HFA}. This product represents the amount of CF_3 initially produced. The data fall along two lines depending on the extent of exposure of the sample. The short exposure data were taken after ~ 20 min. The long exposure data were taken after ~ 90 min. The factor of 6 between the two lines is attributed to a gradual increase in the inhibition effect from the build up of the carbon layer on the surface.

The temperature dependence of the increased SiF_4 production (IR laser on minus IR laser off) is shown in an Arrhenius plot in Fig. 6 for a HFA flow of 2.4×10^{16} s^{-1} and a depletion of 13%. These data were taken after a long exposure time when the inhibition effect had stabilized and the data had good reproducibility. The activation energy for the line is 8 kcal mol^{-1}.

In this set of mass spectrometric experiments, we have observed that the etching reaction behaves as a simple first-order reaction of a product of the IRMPD of the HFA (linear in $f \times F_{HFA}$ and exponential in temperature) and that there is an inhibition effect that increases with exposure
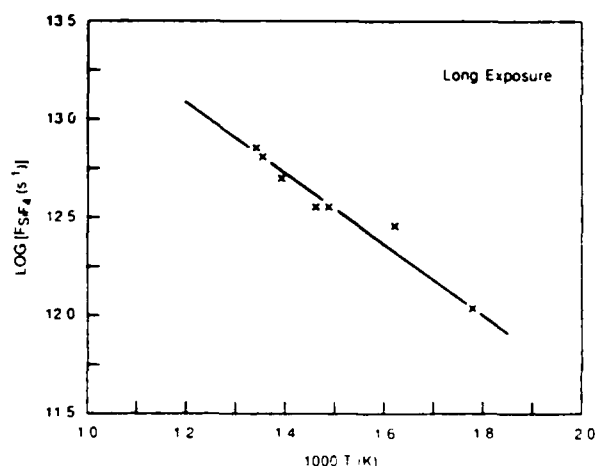
FIG. 6. Arrhenius plot for the production of SiF$_4$ from the IRMPD of HFA. The flow of HFA was 2.4 × 10^{16} s^{-1}, the depletion was 13%, and the pressure in the cell was 3.5 × 10^{-3} Torr. The silicon sample had been exposed to the HFA for a long time (∼ 90 min) before these data were taken.

FIG. 7. The REMPI spectra for HFA with the IR laser off (background) and on (with probe laser delay of 10 ms). The difference between these two spectra is a series of lines that match the expected lines (indicated by the lines across the top of the figure) reported by Duignan et al. (Ref. 29) for the REMPI of CF$_3$. The probe laser wavelength is set at 455 nm for the determination of CF$_3$ kinetics

time. We have concluded that the inhibition is due to the buildup of carbon on the surface, based on the F$_2$ experiments done after exposure of the surface to the HFA. We have also identified CF$_3$ as the radical primarily responsible for the etching, because it is the only species that is produced from both of the precursor gases that were used. Given that the CF$_3$ is responsible for the etching, we would like to know the density of the radical, so that we can derive an absolute etching efficiency. The REMPI determination of the CF$_3$ density, toward that end, will be presented in the next section.

D. REMPI measurements

The REMPI of CF$_3$ has been studied in detail by Duignan et al.[29] using mass spectrometry to detect the ions that are produced. They determined that the ionization of CF$_3$ was a [3 + 1] REMPI in the wavelength region 450–490 nm and explained the observed wavelength dependence in terms of the molecular structure of the radical. We will use those results to understand our experiment where we did not have mass sensitive ion collection. An example of the MPI spectra of HFA is shown in Fig. 7. The bottom curve was taken with the IR laser blocked. The top curve was taken with the IR laser on and a time delay of 10 ms before firing the probe laser. The difference between these two curves (the difference signal) is a series of broad lines that closely match the lines reported by Duignan et al. as being due to CF$_3$ REMPI. For the data below, we have set the probe laser wavelength at the strongest feature in this wavelength range, at 455 nm, and we have identified the difference signal as being proportional to the CF$_3$ density.

In Fig. 8, the REMPI spectra is shown for a short delay time (2 μs) between the IR and probe lasers. At this very early time, the gas in the focus of the probe laser includes

HFA and CF$_3$ that are vibrationally hot. The lines that would be expected from the CF$_3$ are not obvious because they are broadened. Also, because the radicals are concentrated in the beam volume at this early time, the signal is 30 times stronger than at later times when the radicals have diffused throughout the cell. The radicals lose the initial vibrational excitation through wall and gas collisions and dif-
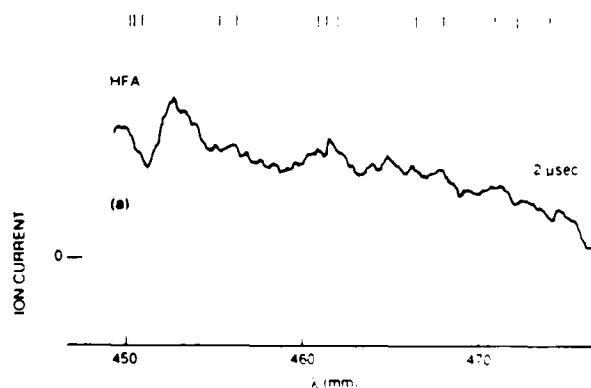

FIG. 8. The REMPI spectra of HFA with the IR laser on and the probe laser delayed by 2 μs. The expected CF$_3$ REMPI features for CF$_3$ are marked along the top of the figure

fuse throughout the cell within 2 ms. After this time, the REMPI spectra appears as shown in Fig. 7, and the REMPI signal is proportional to the CF_3 density throughout the cell. We assume that any chemistry that occurs within this first 2 ms does not proceed any faster than the chemistry at late time, and we will use the late-time data to extrapolate to the zero of time. This assumes that the vibrational excitation does not enhance gas or surface reactions. Also, we assume that the initially high density of CF_3 in the beam volume immediately after the IR pulse is not forming any C_2F_6. These are reasonable assumptions because we are at low pressures and gas–wall collisions dominate over gas–gas collisions.

In order to determine the absolute density and the kinetics of the CF_3 radical, we need to examine the temporal behavior of the REMPI difference signal (IR laser on minus IR laser off) after the radicals have diffused throughout the reactor. This type of data (already calibrated) is shown in Fig. 9 versus the delay time between firing the IR laser and firing the probe laser. The data shown here were taken with the IR laser running at 10 pps, so that we have displayed the time dependence between two IR laser shots. The flow of HFA was 1.33×10^{16} s^{-1}, and the extent of depletion was $f = 0.08$. The time dependence for two silicon sample temperatures are shown, 365 and 730 K, and within the experimental uncertainty the signals were the same. The uncertainty in these measurements results primarily from fluctuations in the pulse energies from the IR and probe lasers, and it has been reduced as much as possible through averaging.

The REMPI data in Fig. 9 have been calibrated in terms of absolute density by using information from the mass spectrometer. We measure the steady-state depletion of the HFA (s^{-1}), therefore, we can determine the number of HFA molecules dissociated per IR pulse, which equals the number of CF_3 molecules created:

$$\Delta[CF_3] = fF_{HFA} t_p/V_c.$$

t_p is the period of the laser, and we have divided by the cell volume V_c to convert to density. This expression assumes the stoichiometry of one CF_3 per decomposed HFA, as determined in our previous studies.[15] The calibration of our collected REMPI signal follows immediately from identifying this calculated change in CF_3 density with the measured change in the REMPI signal, i.e., the difference in the signals at 99 and 1 ms.

We can verify this calibration by calculating the amount of C_2F_6 that would be expected to be formed and comparing it to the measured value. Taking an average $[CF_3] = 4.4 \times 10^{11}$ cm^{-3}, squaring and multiplying by k_r (Ref. 17) and V_c, we find a rate of C_2F_6 formation of 3.6×10^{14} s^{-1}. This is in good agreement with the measured rate of 2.7×10^{14} s^{-1}. Using this average value, we can immediately calculate the other loss yields for CF_3; 51% goes to C_2F_6, 12% escapes from the reactor, and the remainder is lost on either hot or cold walls. The total first-order loss of CF_3 is 1.9 s^{-1}. The observation that the CF_3 density did not decrease at high temperature indicates that the CF_3 loss on the hot silicon sample is still a minor loss channel. The SiF_4 production at 365 K was not measurable. The rate at 730 K was 2×10^{13} s^{-1}. This rate can be accounted for by 2.5% of the CF_3 loss rate.

From these REMPI measurements we conclude that the proposed reaction scheme is valid, and thus we can use a steady-state analytical solution of the model to determine a steady-state radical density in the experiments where only mass spectrometer measurements were taken:

$$[CF_3]_{ss} = \frac{-(k_1) + [(k_1)^2 + 8k_r fF_{HFA} V_c]^{1/2}}{4k_r}.$$

k_r is the recombination rate constant, and k_1 is the first-order loss rate for escape plus hot or cold wall loss. The steady-state density calculated for the conditions above is 4.0×10^{11} cm^{-3}, compared to the REMPI determination of an average of 4.4×10^{11} cm^{-3}.

E. Dark reaction of HFA

In Fig. 4, it was observed that HFA did etch silicon when the IR laser was blocked. HFA was also observed to etch silicon under the conditions used to take the data in Figs. 5 and 6. We did not determine all of the kinetics of this dark reaction; however, we can make some observations on the data taken in the course of studying the CF_3 etching reaction.

At a constant temperature of 718 K, i.e., the conditions of Fig. 5, the flow of SiF_4 out of the reactor varied roughly linearly between 1×10^{13} and 3×10^{13} s^{-1} for a range of HFA flows of 2×10^{15} to 3.9×10^{16} s^{-1}. This is a weak pressure dependence, and an extrapolation of the data to zero HFA flow does not go to zero SiF_4 flow. Thus, the reaction is not a simple first-order reaction in the HFA pressure, it is a more complicated mechanism. Also, the SiF_4 production from the HFA dark reaction did not decrease for the range of exposure times that were present in Fig. 5, as was observed for the CF_3 reaction.
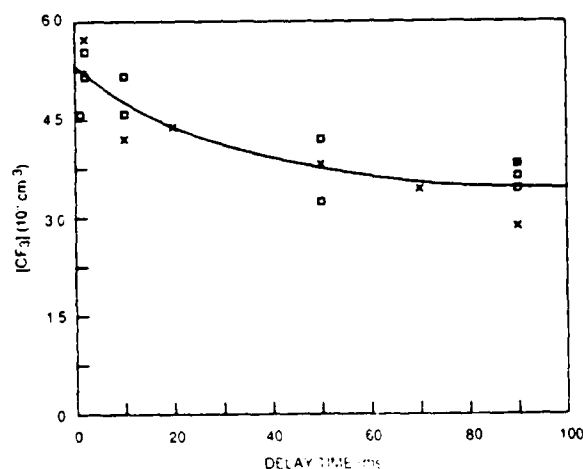

FIG. 9. CF_3 density vs time between IR laser shots. The density is proportional to the REMPI difference signal at 455 nm, and the calibration is discussed in the text. The data at the two temperatures ($\square$ 730 and $\times$ 365 K) are the same within the experimental scatter.

At a constant HFA flow of 2.4×10^{16} s^{-1}, i.e., the conditions of Fig. 6, the SiF$_4$ production had an activation energy of 10 kcal mol^{-1}. This is comparable to the activation energy for the CF$_3$ etching, though the pressure dependences of these two reactions are very different. It is also important to note that the loss of HFA due to this surface reaction is small and does not appreciably change the density of HFA in the gas.

IV. DISCUSSION

The measurements of the SiF$_4$ production and the density of CF$_3$ in the reactor can be combined to determine the reaction probability ϵ, which is defined as four times the flow of SiF$_4$ coming off the surface divided by three times the collision frequency of CF$_3$ with the surface:

$$\epsilon = \frac{4}{3} \frac{F_{\text{SiF}_4}}{v_{\text{th}} A_s [CF_3]/4}.$$

The factor of $\frac{4}{3}$ is included so that the maximum reaction probability is unity. The reaction probability for CF$_3$ is plotted in Fig. 10 along with the values reported[19,23] for F and F$_2$. The $\times$'s represent the temperature dependent data from Fig. 6. These data were taken on a surface that had been exposed to HFA for a long period, so that the surface had a carbon film and the etching was inhibited. The boxes represent the time scan data with HFA from Fig. 4. The top point is the reaction probability immediately after introducing the HFA when the surface was fresh (that is after F$_2$ etching). The bottom point is for the end of the time scan after inhibition had set in. The time scan and temperature data together give the range of reaction probabilities from fresh to fully inhibited surface. The triangles in Fig. 10 represent the time scan data with CF$_3$I, again showing the initial and inhibited reaction probabilities.

The sticking probability of CF$_3$ on the silicon sample was not determined. However, we can make an estimate of an

FIG. 10. The reaction probability for the etching of silicon ϵ vs inverse temperature. The triangles represent $\epsilon(CF_3)$ data from Fig. 4 for CF$_3$I, and the boxes represent $\epsilon(CF_3)$ data from Fig. 4 for HFA. The $\times$'s represent the data $\epsilon(CF_3)$ from Fig. 6 for HFA and a surface that had been exposed for a long period. ϵ for F (Ref. 23) and F$_2$ (Ref. 19) are shown for comparison.

upper limit. The total first-order wall loss k_w of CF$_3$ was determined from the REMPI data to be 1.4 s^{-1}, and the wall collision frequency for CF$_3$ is 9030 s^{-1}. Thus, the average sticking coefficient in the reactor is $\gamma = 1.6 \times 10^{-4}$. The sensitivity of our REMPI measurement limits our determination of changes in k_w to values larger than 0.2 s^{-1}. In order for the hot silicon sample to produce this magnitude of a change in the total k_w, the sticking coefficient on the hot sample would have to be larger than $0.2/k_c$, or larger than 10^{-3}. Because we did not observe changes in k_w, this value is an upper limit.

We can now make some comparisons to the reaction probabilities of F and F$_2$. The reaction probability of CF$_3$ (and F$_2$) is much smaller than for F atoms which do not require high temperatures to enable the etching. The reaction probability of CF$_3$ on a fresh, fluorinated silicon surface at high temperatures is comparable to that of F$_2$ (also on a fluorinated surface). The activation energy for $\epsilon(CF_3)$ on fresh silicon was not measured, but it is most likely comparable to the activation energy on the carbon film (8 kcal mol^{-1})and to the activation energy for $\epsilon(F_2)$ (12.9 , 9.2, and 8 kcal mol^{-1} from Refs. 19, 20, and 21, respectively). Thus, on a fresh surface F$_2$ and CF$_3$ have comparable reaction probabilities. For a surface with a fluorocarbon film $\epsilon(CF_3)$ is reduced by a factor of 20 to 40. We also observed that the etching by F$_2$ was inhibited by the carbon film, though quantitative studies were not performed. In one case that was recorded, an inhibition factor larger than 4 was observed, and it is not unreasonable to assume that the carbon film inhibited the F$_2$ etch to extents comparable to that of CF$_3$. Therefore, a general conclusion can be reached: F$_2$ and CF$_3$ have comparable ϵ, independent of the surface character.

Because we interrogate exclusively the gas phase and thus have no information on the condition of the surface, we are not able to derive a detailed model for the etching mechanism of CF$_3$. However, we can assert the following. We observe that the SiF$_4$ production rate is linear in the CF$_3$ production rate and thus does not reach a limiting rate at the higher CF$_3$ densities. Thus, in a Langmuir–Hinshelwood adsorption–reaction model, the adsorption step would be in the linear regime, or not limited by the availability of surface reaction sites. This means that, under our conditions with a fluorocarbon film, the surface reaction that creates reaction sites is faster than the adsorption step that consumes them. Other models are also possible in which the adsorption step does not consume a reaction site.

Flamm and Donnelly[1] describe a model of etching SiO$_2$ through a thick fluorocarbon film that includes various steps. Oehrlein and Williams[3] reported the silicon etch rate dependence on the thickness of the film and briefly mention a model, in which the etch rate is controlled by the diffusion of F to the silicon–fluorocarbon interface and diffusion of volatile products. A model of this type may be appropriate to explain our observed etch rate kinetics and the inhibition effect. The addition of surface diagnostics and improvement in the REMPI sensitivity would enable us to set up a more detailed surface reaction model on the CF$_3$ etching mechanism.
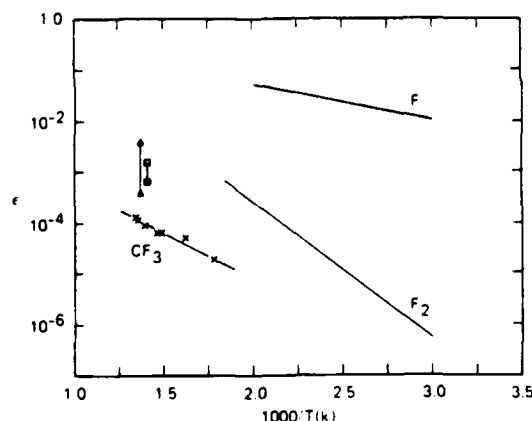
The reaction probability for HFA to etch silicon can be determined with an expression analogous to that for CF_3 radicals. The result is that HFA has an $\epsilon \sim 60$ times smaller than CF_3 on a fluorocarbon coated silicon surface; that is relative to the data in Fig. 6. The corresponding HFA-etching rate constant is smaller, but the etch rate is comparable to the etch rate by CF_3 because the HFA density is much larger than the CF_3 density. Based on the time-dependent data in Fig. 4, we conclude that the dark reaction of HFA is occurring in parallel with, and independent of, the etching by CF_3. The HFA is not causing any specific changes in the surface that would change the etch rate by CF_3 alone.

We are now in a position to make some general comments on the mechanism of the "dark" (etching) reaction of HFA. The observed weak dependence of the SiF_4 rate of formation on HFA pressure suggests that the reaction rate is close to saturation. This means that it is limited by the availability of reactive surface sites. The reactive surface site required for a HFA to react is likely to be very different than sites involved in CF_3 adsorption. The activation energy for the overall mechanism applies to the rate limiting step, which may be the initial bond-breaking step into $CF_3 + CF_3CO$ preceded by adsorption or any of the subsequent steps. The initial bond-breaking step can have an activation energy significantly less than the gas-phase bond energy (80 kcal mol^{-1}) if it leads to the formation of new bonds in the bond scission products. A possible adsorption–reaction step is the reaction of the HFA with a carbon dangling bond on the surface, leading to an adsorbed CF_3 and a desorbing $COCF_3$. This type of reaction would be consistent with the observed kinetics. The activation barrier for the dissociative adsorption step could be low, and the weak pressure dependence could result from the low surface density of the dangling bond sites, which are easily saturated.

V. CONCLUSION

We have presented quantitative, temperature-dependent, rate measurements for the reaction of CF_3 radicals with silicon surfaces. The absolute reaction probability is low compared to F atoms, and comparable to F_2. The VLPΦ reactor with REMPI and mass spectrometric diagnostics has proven successful for the study of radical–surface reactions.

ACKNOWLEDGMENT

*) Postdoctoral Research Associate.

[1] D. L. Flamm, V. M. Donnelly, and D. E. Ibbotson, VLSI Electron Microstructure Sci. 8, 190 (1984).

[2] J. W. Coburn, J. Appl. Phys. 50, 5210 (1979).

[3] G. S. Oehrlein and H. L. Williams, J. Appl. Phys. 62, 662 (1987).

[4] J. P. Booth, G. Hancock, and N. D. Perry, Appl. Phys. Lett. 50, 318 (1987).

[5] I. C. Plumb and K. R. Ryan, Plasma Chem. Plasma Proc. 6, 205 (1986).

[6] J. I. Steinfeld, T. G. Anderson, C. Reiser, D. R. Denison, L. D. Hartsough, and J. R. Hollahan, J. Electrochem. Soc. 127, 514 (1980).

[7] G. L. Loper and M. D. Tabat, Proc. SPIE 459, 121 (1984).

[8] G. L. Loper and M. D. Tabat, Appl. Phys. Lett. 46, 654 (1985).

[9] J. H. Brannon, J. Phys. Chem. 90, 1784 (1986).

[10] H. F. Winters, J. Appl. Phys. 49, 5165 (1978).

[11] B. Roop, S. Joyce, J. C. Schultz, and J. I. Steinfeld. J. Chem. Phys. 83, 6012 (1985).

[12] S. Joyce, J. G. Langan, and J. I. Steinfeld, J. Chem. Phys. 88, 2027 (1988).

[13] J. W. Thoman, Jr., K. Suzuki, S. H. Kable, and J. I. Steinfeld, J. Appl. Phys. 60, 2775 (1986).

[14] F. R. McFeely and J. A. Yarmoff, Paper JS1-TuM8 in the Final Program of the 34th National Symposium of the AVS, 1987, p 108

[15] R. M. Robertson, D. M. Golden, and M. J. Rossi, J. Phys. Chem. (to be published).

[16] R. M. Robertson, D. M. Golden, and M. J. Rossi, J. Chem. Phys. (to be published).

[17] N. Selamoglu, M. J. Rossi, and D. M. Golden, Chem. Phys. Lett. 124, 68 (1986).

[18] T. E. Adams, R. J. S. Morrison, and E. R. Grant, Rev. Sci. Instrum. 51, 141 (1980).

[19] N. Selamoglu, J. A. Mucha, D. L. Flamm, and D. E. Ibbotson, J. Appl. Phys. 62, 1049 (1987).

[20] J. A. Mucha, V. M. Donnelly, D. L. Flamm, and L. M. Webb, J. Phys. Chem. 85, 3529 (1981).

[21] M. Chen, V. J. Minkiewicz, and K. Lee, J. Electrochem. Soc. 126, 1946 (1979).

[22] F. R. McFeely, J. F. Morar, and F. J. Himpsel, Surf. Sci. 165, 277 (1986).

[23] M. J. Vasile and F. A. Stevie, J. Appl. Phys. 53, 3799 (1982).

[24] A. Freedman, K. E. McCurdy, J. Wormhoudt, and P. P. Gaspar, Chem. Phys. Lett. 142, 255 (1987).

[25] P. A. Hackett, C. Willis, and M. Gauthier, J. Chem. Phys. 71, 2682 (1979).

[26] G. G. A. Perkins, E. R. Austin, and F. W. Lampe, J. Chem. Phys. 68, 4357 (1978).

[27] J. C. Amphlett and E. Whittle, Trans. Faraday Soc. 63, 80 (1967).

[28] J. A. Kerr and J. P. Wright, J. Chem. Soc. Faraday Trans. 1 81, 1471 (1985).

[29] M. T. Duignan, J. W. Hudgens, and J. R. Wyatt, J. Phys. Chem. 86, 4156 (1982).

Appendix F

ATOM- AND RADICAL-SURFACE STICKING COEFFICIENTS MEASURED USING RESONANCE-ENHANCED MULTIPHOTON IONIZATION (REMPI)

ATOM- AND RADICAL-SURFACE STICKING COEFFICIENTS MEASURED USING RESONANCE ENHANCED MULTIPHOTON IONIZATION (REMPI)

ROBERT M. ROBERTSON* AND MICHEL J. ROSSI**
*Present Address: Applied Materials Corporation, Santa Clara CA 95054
**Department of Chemical Kinetics, SRI International, Menlo Park CA 94025

ABSTRACT

Sticking coefficients γ of neutral transient species at ambient temperature were measured using in situ Resonance Enhanced Multiphoton Ionization (REMPI) of the transients in a Knudsen cell. γ for I and $CF_3I^\ddagger$ on a stainless steel surface were 0.16 and >0.5, respectively, whereas γ for CF_3 on the same surface was measured to <0.01; γ of SiH_2 on a growing carbon containing amorphous silicon surface was 0.11; this value increased to 0.15 for interaction of SiH_2 with a "pure" growing silicon-hydrogen surface, and γ of $SiH_2^\ddagger$ on both types of surfaces was found to be >0.5.

INTRODUCTION

Due to the ever shrinking dimensions of thin film devices and VLSI chips, it is essential to control the different processes involved in VLSI chip production. In order to achieve control over these processes, fundamental understanding in terms of elementary reactions occurring in the gas phase and on the solid substrate is required. Our approach involves selective generation of one and only one atomic or molecular species using photolytic methods and to investigate its interaction in situ with a given surface under experimental conditions that come as close as possible to process conditions.

In this paper we present results on the sticking coefficients of several atomic and molecular species on surfaces of practical interest. The use of the term "sticking" is ambiguous in the case of wall deactivation of vibrationally excited species, because the process may not correspond to mass accomodation but rather to energy transfer or energy accomodation. We use this term only to describe the disappearance of the detected species due to heterogeneous interaction with the surface of interest.

EXPERIMENTAL

The experimental apparatus has been described in detail elsewhere [1], so that only a brief description will be given here. The Very Low Pressure Photolysis (VLPΦ) reactor is a Knudsen cell, which is part of a flowing gas experiment. The pressure inside the VLPΦ reactor is in the mTorr range (give or take a decade), so that the molecules undergo predominantly gas-wall collisions. The molecules of interest are generated from appropriate precursors either via IR-MPD using a pulsed CO_2 TEA laser or via single photon UV photolysis using a pulsed excimer laser.

The measurement principle rests on the fact, that one compares the rate of the process of interest with the rate of a "reference" process. By calibrating this "reference" process for the atom or free radical of interest, one can then put this relative comparison of rates on an absolute basis. The Knudsen cell used in our investigations uses the gas-wall collision rate as a reference process for decay processes on the tens of μs time scale, whereas slow decay processes are measured against the effusion of the species out of the Knudsen cell. Consequently, fast transient decay

processes are monitored in situ using time dependent resonance enhanced multiphoton ionization (REMPI) detection of the atom or free radical, whereas slow processes are followed either in steady state or in a time resolved (ms) manner using quadrupole mass spectrometry.

The Knudsen cell is displayed schematically in Figure 1. It is a stainless steel six-way cross coated with gold on the inside. The cell is equipped with an inner tube that is oriented coaxially to the beam of the laser photolysis. The pulsed laser generates the neutral transients initially in a fraction of the volume of the inner tube in a collisionless manner. Subsequently, the transient species fill the volume of the inner tube homogeneously by molecular diffusion on a μs time scale (Table I). This process of diffusion is followed by gas-wall collisions taking place on a longer time scale (see Table I). The decay of the REMPI signal (k/s^{-1}) of the transient is compared to the gas-wall collision frequency ω, hence a sticking coefficient γ is calculated ($\gamma = k/\omega$), which describes the number of wall collisions required to remove the transient species irreversibly from the gas-phase.

The subsequent fate of the radical is to escape from the inner tube into the plenum of the Knudsen cell, and finally escape into the vacuum chamber on a progressively longer time scale (Table I). In experiments with CF_3 radical, the inner tube was removed. In this case mass spectrometric observation of the loss of reactant and build-up of stable product molecules was used to determine an accurate numerical value of γ [2].
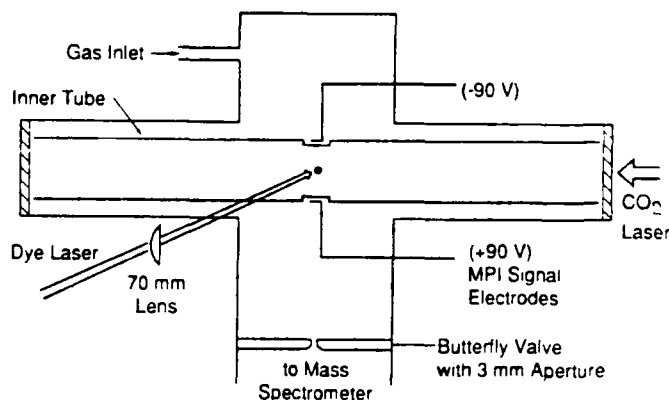
Figure 1

The stainless steel VLPΦ reactor for measurement of sticking coefficients.

RESULTS AND DISCUSSION

The sticking coefficient of I atoms and highly vibrationally excited CF_3I molecules on stainless steel at ambient temperature was determined using the following generation scheme:

$$CF_3I + nh\nu \rightarrow CF_3 + I \qquad (1)$$
$$\rightarrow CF_3I^{\ddagger} \qquad (2)$$

At fluences below 2 J cm^{-2}, IR-multiphoton excitation causes only partial decomposition of CF_3I with a sizable fraction of the irradiated CF_3I in

TABLE I

CHARACTERISTIC RATE CONSTANTS FOR THE VLPΦ/REMPI EXPERIMENT
T/K, M/amu, $v_{th}/cm\ s^{-1}$, r_B/cm, A/cm^2, V/cm^3

Process		Rate Constant (s^{-1})		Time Constant (for SiH_2)
Production				$2\mu s$
Dilution	k_d	$-v_{th}/r_B$	$30000(T/M)^{1/2}$	$10\mu s$
Wall collision	ω	$v_{th}A_T/4V_T$	$9000(T/M)^{1/2}$	$35\mu s$
Escape tube	k_{eT}	$v_{th}A_{eT}/4V_T$	$135(T/M)^{1/2}$	2.3 ms
Escape reactor	k_{eR}	$v_{th}A_{eR}/4V_R$	$0.24(T/M)^{1/2}$	1.3 s

high lying vibrational states. The REMPI spectrum of IR-multiphoton excited CF_3I in the range of 460 to 490 nm shows sharp resonances due to both I in the ground state ($5p^5\ ^2P_{3/2}$) and I in the upper excited spin state ($^2P_{1/2}$), that is I^* [3]. The origin of I^* can be traced back to the presence of highly excited CF_3I, that is $CF_3I^{\ddagger}$, which undergoes single photon dissociation to $CF_3 + I^*$ in high quantum yield [4]. IR-MPD of CF_3I cannot lead to excited I in the upper spin state. Both I and I^* are ionized through a [3 + 1] REMPI process, and thermochemical arguments confer a lower limit of 5900 cm^{-1} of internal energy to $CF_3I^{\ddagger}$, roughly corresponding to one quantum of vibrational energy in each of the normal modes of CF_3I [3].

The time dependence of the REMPI signals for I monitored at 474.5 nm and for $CF_3I^{\ddagger}$ (via REMPI of I^*) monitored at 477.8 nm is displayed in Figure 2. The rapid decay of the REMPI signal in the first 30 μs corresponds to homogeneous filling of the inner tube by I or $CF_3I^{\ddagger}$ with a rate constant given in Table I.
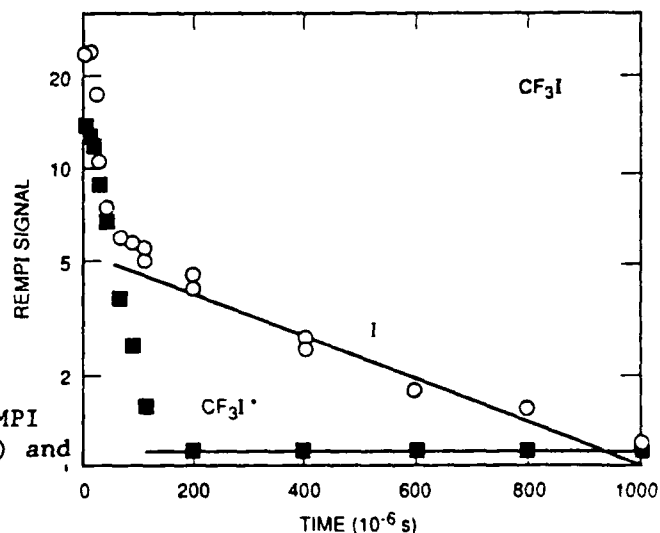
Figure 2

Time dependence of the total REMPI signals at 474.5 nm (I, circles) and 477.8 nm ($CF_3I^{\ddagger}$ squares).

RA-M-1227-42A

The I REMPI signal decays with a unimolecular rate constant of 2.2×10^3 s^{-1} leading to a sticking coefficient $\gamma=0.16$ with ω from Table I. The relevant surface is the inner surface of the stainless steel tube that was exposed to CF_3I, CF_3 and I. The decay of the REMPI signal monitoring the time dependent density of $CF_3I^{\ddagger}$ is merged with the molecular diffusion of that species within the inner tube, so that the two time scales can not be

separated. This situation is presented in Figure 2, where the REMPI signal at 477.8 nm rapidly falls to a constant level with a unimolecular rate constant of 2.2×10^4 s^{-1}, thus yielding a lower limit of 0.5 for γ.

Kinetic data on wall deactivation of atoms and free radicals are sparse, and even more so for vibrationally excited species. The sticking coefficient for atomic oxygen on single crystal silicon has been found to be essentially unity [6], whereas atomic bromine and chlorine hardly interact at all with a Teflon or halocarbon wax surface [7]. The present data indicate a rapid deactivation of I on an oxidized metal surface, which is perhaps surprising in view of the expected weak bonding of I on an oxide surface. Highly vibrationally excited CF_3I with approximately 5900 cm^{-1} of excess energy transfers energy upon essentially every collision, a finding that is not unexpected for those internal energies. Similarly, the fate of I after a deactivating collision with the VLPΦ vessel wall is not addressed in the present experiments. We observe molecular I_2 by mass spectrometry as a result of I interaction with the vessel walls and subsequent wall catalyzed atom recombination.

The sticking coefficient of CF_3 free radical was measured on the stainless steel surface of the inner tube of the VLPΦ vessel using hexafluoroacetone, CF_3COCF_3, as a precursor. The IR-MPD of CF_3COCF_3 has been discussed before [1] and is briefly presented in equations (3):

$$CF_3COCF_3 + nh\nu \rightarrow CF_3 + COCF_3 \qquad (3)$$

The REMPI spectrum of CF_3 was studied in detail by Duignan et al. [8]. It is due to [3+1] ionization in the wavelength range of 420 to 490 nm. The time dependence of the REMPI signal was monitored at 455.6 nm and is presented in Figure 3. The REMPI signal decreases rapidly in the first 100 μs and reaches a constant level thereafter. On a much longer time scale (90 ms), Figure 3 shows a slight decrease of the REMPI signal (filled circle). Due to the negligible CF_3 decay on the time scale of a ms, we conclude that γ must be smaller than 0.01. In fact, from other experiments [1], we found γ for CF_3 to be 2.2×10^{-5} on a gold surface. CF_3 free radical seems to be an example of an inert radical in relation to wall collisions with gold, stainless steel and SiO_2 up to temperatures of 720K [3]. It is so inert, that its deactivation rate has to be measured against its effusion out of the Knudsen cell and the technique presented above for I becomes inapplicable. In contrast,
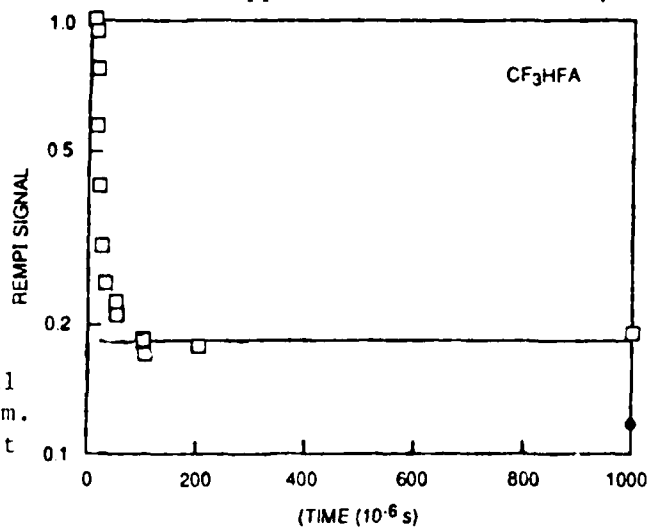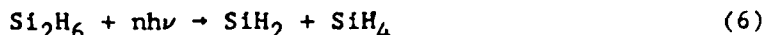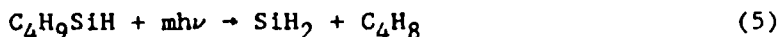
Figure 3

Time dependence of the total CF_3 REMPI signal at 455.6 nm. The solid point on the right ordinate corresponds to the REMPI signal at 90 ms.

RA 1227 29

Winters finds γ to be between 0.08 and 0.75 for CF_3 on clean silicon under UHV conditions [9]. This is almost certainly the consequence of the presence of dangling bonds on the Si surface, which become saturated through the interaction with CF_3 free radical.
The sticking coefficient of SiH_2 and $SiH_2^\ddagger$ on an amorphous silicon surface was studied using n-$C_4H_9SiH_3$ and Si_2H_6 as precursors in IR-MPD schemes presented in equations (4), (5) and (6):

$$C_4H_9SiH_3 + nh\nu \rightarrow C_4H_9SiH + H_2 \tag{4}$$

$$C_4H_9SiH + mh\nu \rightarrow SiH_2 + C_4H_8 \tag{5}$$

$$Si_2H_6 + nh\nu \rightarrow SiH_2 + SiH_4 \tag{6}$$

The REMPI spectrum of SiH_2 was not known prior to our study, so that we had to confirm the presence of SiH_2 and the assignment of the resulting REMPI spectrum by using different precursors. Pertinent details are discussed in [10]. Briefly, the REMPI spectrum of SiH_2 consists of two kinds of transitions: one consists of a series of congested lines corresponding to [3+1] REMPI via molecular Rydberg states of SiH_2, and the other consists of single intense sharp peaks corresponding to [2+1] REMPI $Si(^1D_2)$. This excited silicon state is generated by single photon dissociation of highly vibrationally excited $SiH_2^\ddagger$ to the molecular A state of SiH_2, which predissociates into $Si(^1D_2)$ + H_2. The REMPI signal at 487.9 nm probes $SiH_2^\ddagger$ with an internal energy content of approximately 7000 cm^{-1}, whereas similar sharp lines in the REMPI spectrum around 363 to 366 nm probe the ground state of SiH_2.

Figure 4 presents the time dependent REMPI signal for SiH_2 monitored at 500 nm and for $SiH_2^\ddagger$ monitored at 487.9 nm. The sticking coefficient for SiH_2 on an Si-C surface was measured to be 0.11, whereas γ for $SiH_2^\ddagger$ is larger than 0.5, in analogy to the results for $CF_3I^\ddagger$ discussed above. We note the excellent dynamic range of the REMPI signal over almost four decades of signal strength. Due to the overlap of the REMPI spectrum via the atomic resonance in $Si(^1D_2)$ and via molecular Rydberg states in SiH_2, the REMPI signal at 487.9 nm has a slower decay component that corresponds to the decay rate constant of the REMPI signal at 500 nm. At this wavelength of 487.9 nm the REMPI signal probes both the fast decaying $SiH_2^\ddagger$ as well as the slower decaying ground state of SiH_2.
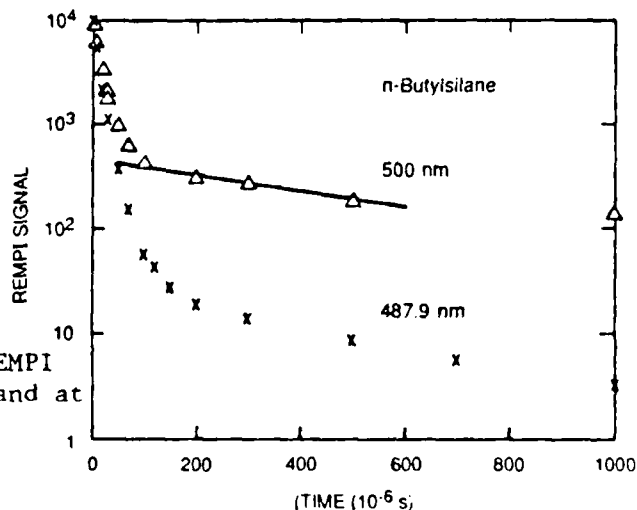
Figure 4

Time dependence of the total REMPI signals at 487.9 nm ($SiH_2^\ddagger$, x) and at 500.0 nm SiH_2 (triangles).

RA 320522 171B

The sticking coefficient for SiH_2 on a silicon surface containing carbon (by virtue of using n-butylsilane as the SiH_2 precursor) is 0.1, whereas γ for a "pure" silicon surface using disilane as the SiH_2 precursor is approximately 50% larger, on the order of 0.15. This value seems low in view of the fact that modeling efforts "require" values on the order of 0.7 to 1.0. However, these modeling efforts relate to deposition conditions, for surface temperatures between 150 to 250 C. The present results. however, refer to a surface at ambient temperature. For comparison purposes we note that the sticking coefficient for the closely related SiH_3 is on the order of 0.1 for a surface at higher temperature [11], whereas the sticking coefficient for SiH_4 is negligible in comparison, even at high temperatures [12,13].

ACKNOWLEDGEMENT

REFERENCES.

1. R. M. Robertson, D. M. Golden and M. J. Rossi, J. Phys. Chem., 92, 5338 (1988); J. Vac. Sci. Technol. A5, 3351 (1987).

2. N. Selamoglu, M. J. Rossi and D. M. Golden, J. Chem. Phys. 84, 2400 (1986).

3. R. M. Robertson, D. M. Golden and M. J. Rossi, J. Chem. Phys. 89, 2925 (1988).

4. W. P. Hess, S. C. Kohler, H. K. Haugen, and S. R. Leone, J. Chem. Phys. 84, 2143 (1986); W. P. Hess and S. R. Leone, ibid., 86, 3773 (1987).

5. S. C. Saxena and R. K. Joshi, in Thermal Accomodation and Adsorption Coefficients of Gases, McGraw-Hill/CINDAS Data Series on Material Properties, Vol. II-1, McGraw-Hill Book Co., 1981.

6. J. R. Engstrom, M. M. Nelson and T. Engel, This Symposium (E: Chemical Perspectives of Electronic Materials).

7. S. W. Benson, O. Kondo and R. M. Marshall, Int. J. Chem. Kinet., 19, 829 (1987).

8. M. T. Duignan, J. W. Hudgens and J. R. Wyatt, J. Phys. Chem. 86, 4156 (1982).

9. H. F. Winters, J. Appl. Phys. 49, 5165 (1978).

10. R. M. Robertson and M. J. Rossi, submitted to J. Chem. Phys.

11. J. Perrin and T. Broekhuizen, Appl. Phys. Lett. 50, 433 (1987).

12. R. Buss, P. Ho, W. G. Breiland and M. E. Coltrin, J. Appl. Phys. 63, 2808 (1988).

13. S. M. Gates, Surf. Sci. 195, 307 (1988).

Appendix G

STICKING COEFFICIENTS OF THE SIH_2 FREE RADICAL
ON A HYDROGENATED SILICON-CARBON SURFACE

Sticking coefficient of the SiH_2 free radical on a hydrogenated silicon-carbon surface

Robert M. Robertson and Michel J. Rossi

Department of Chemical Kinetics, SRI International, Menlo Park, California 94025

The sticking coefficient of SiH_2 on a hydrogenated silicon-carbon surface is measured in a low-pressure pulsed-photolysis experiment. Thermal and vibrationally excited SiH_2 are created by infrared multiphoton decomposition of n-butylsilane. The first-order wall loss rates of the radicals are determined from the time dependence of the resonance-enhanced multiphoton ionization signal. The sticking coefficients of SiH_2 (~ 0.1) and vibrationally hot SiH_2 (> 0.5) are determined from the measured first-order loss rate constants and the calculated wall collision rate constant.

The SiH_2 radical has attracted much attention in recent years because of the importance of silicon deposition from silanes. While great progress has resulted on the gas phase reactivity of this species, little is known about the reactivity at surfaces. In some thermal and plasma deposition models[1,2] it is assumed to have a surface sticking coefficient γ of unity on amorphous silicon surfaces. This assumption is supported by the fast gas phase insertion rate constants[3,4] of SiH_2 in silanes. However, it is important to measure γ for reactive intermediates under a variety of surface conditions to improve understanding and control of the deposition process.

We are studying radical-surface reactions in a low-pressure photolysis reactor using infrared multiphoton decomposition (IRMPD) to selectively create radicals from an appropriate precursor gas. Mass spectrometry is used to monitor the precursor and stable product species effusing from the cell, and resonance-enhanced multiphoton ionization (REMPI) is used to monitor the time dependence of a specific species in the reactor. Typical pressures for these experiments are 1×10^{-3} Torr. Thus we are in the molecular flow regime, and gas-wall collisions are more frequent than gas-gas collisions. Our first use of this technique[5,6] was for the quantitative measurement of silicon etching by the CF_3 radical. In this experiment the radical had a low surface sticking coefficient ($\gamma \sim 10^{-4}$) on the reactor walls and the hot silicon wafer. We have now adapted the VLPΦ reactor, Fig. 1, to have good sensitivity for the measurement of γ for radicals that have rapid wall losses ($\gamma = 0.5$–0.01). The inner tube has the function of supporting the reactive surface and preventing the radicals from diffusing throughout the volume of the reactor (see below). In this letter we demonstrate the capability of this technique by examining SiH_2 produced from the IRMPD of n-butylsilane. The active surface is the thin-film coating produced by the photolysis of n-butylsilane which is nominally a hydrogenated silicon and carbon amorphous alloy.

The model of this pulsed laser experiment can be explained by reference to the time scales involved. The precursor gas undergoes collisionless unimolecular decomposition during the ~ 2-μs-long infrared (IR) laser pulse. The products are initially located in the IR beam volume and disperse to fill the inner tube on a time scale determined by the ther-

mal velocity of the molecules, v_{th}. The density of the transient species in the REMPI probe volume (which is in the IR beam volume) decreases, with a molecular-flow dilution rate constant k_d. After this dilution time (0.1 ms) the transient species will have formed a uniform density in the inner tube. Between 0.1 and 1 ms the molecules undergo wall and gas collisions inside the inner tube. The wall collision frequency ω is given by $v_{th} A_I /4 V_I$. A_I (113 cm^2) and V_I (45.4 cm^3) are the surface area and volume inside the tube, respectively, and $\omega = 9000(T/M)^{1/2}$, where T is the temperature in kelvin and M is the molecular mass in atomic units. The loss rate constant in this time period, k_1, is the parameter of primary interest in this letter and is used to determine γ, defined as k_1 /ω.

On the time scale of 1–10 ms stable molecules escape the inner tube with a rate constant given by $k_{eT} = v_{th} A_I /4 V_I$. A_{eT} is the area through which the molecules can escape from the tube (1.7 cm^2), so that $k_{eT} = 135(T/M)^{1/2}$ s^{-1}. On the time scale of 10–90 ms the molecules escape from the main reactor through the exit aperture with a measured rate constant $k_{ec} = 0.24(T/M)^{1/2}$ s^{-1}. Fresh precursor gas enters the reactor on this same time scale.

The IRMPD of n-butylsilane has been studied,[7] and two mechanisms are able to explain the primary products.

$$C_4H_9SiH_3 + nh\nu \rightarrow C_4H_x + SiH_3. \tag{1}$$

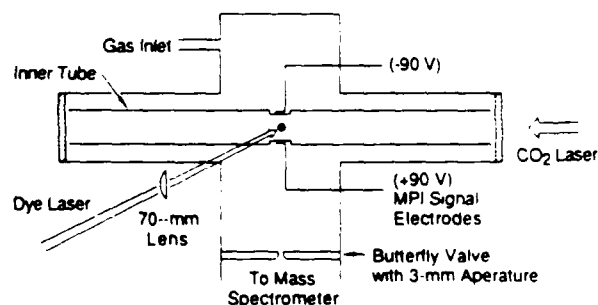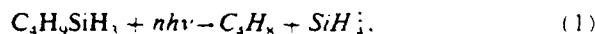$$SiH_3 + nh\nu \rightarrow SiH_2 + H_2. \tag{2}$$

FIG. 1. VLPΦ reactor (drawn approximately to scale) is a six-way stainless-steel cross. The inner tube has an inside diameter of 16.5 mm and length of 210 mm.
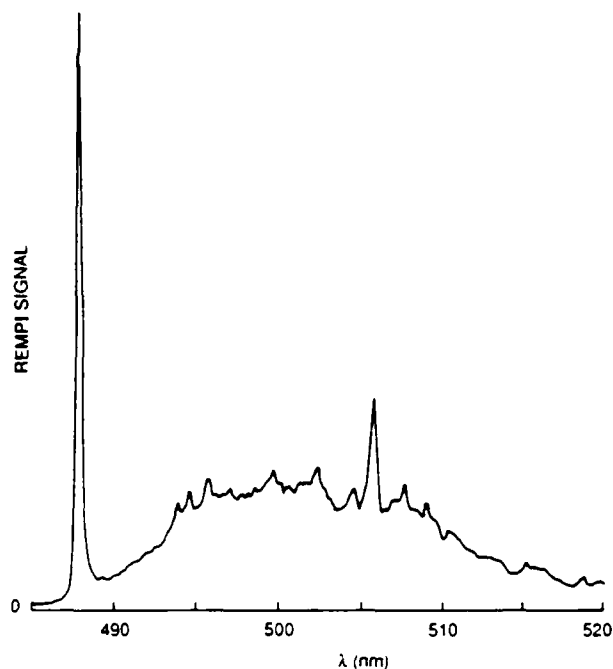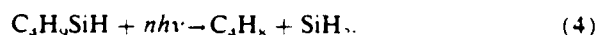
FIG. 2. REMPI spectra in n-butylsilane 20 μs after the IR laser has fired. The pressure was 0.16 × 10⁻⁵ Torr and the extent of depletion was 12%. The spectra are strongly influenced by the dye laser power curve. At 500 nm the dye laser pulse energy was 2.6 mJ, and at 487.9 nm the pulse energy had fallen to 0.8 mJ.

$$C_4H_9SiH_3 + nh\nu \rightarrow C_4H_9SiH + H_2,$$ (3)

$$C_4H_9SiH + nh\nu \rightarrow C_4H_x + SiH_2.$$ (4)

The first mechanism [Eqs. (1) and (2)] was favored by Francisco et al.,[7] whereas a mechanism following Eqs. (3) and (4) was deduced for the thermal decomposition[x] of n-butylsilane. It is not critical to our results which mechanism is dominant. It is only important that SiH₂ is produced by the IR pulse, as was confirmed with laser-induced fluorescence detection by Thoman and Steinfeld.[9] Francisco et al.[7] reported the composition of the films formed from the IRMPD of phenylsilane to be rich in carbon. It is likely that similar carbon-rich films are produced from the IRMPD of n-butylsilane.

The REMPI spectrum of SiH₂ has not been reported, so we must deduce which REPMI features in our total ion detection are due to SiH₂. The REMPI spectrum, Fig. 2, taken 20 μs after the IR pulse, is primarily due to transient species with only a small contribution from the precursor and stable products. An identical, though weaker, spectrum results from the IRMPD of Si₂H₆, so that the transient species responsible for this spectrum must be common to both precursor gases. The transient species are SiH₂ and SiH₃⁺, and we discuss the origins of the features below. The only other species that are common to both precursor gases are SiH₄ and SiH₃⁺. Based on the low signals produced by REMPI of an authentic sample of SiH₄, we conclude that this spectrum is not due to thermal SiH₄. It is highly unlikely that the vibrational excitation of SiH₄ would sufficiently increase the ionization efficiency to account for the observed transient signal strengths.

The sharp feature at 487.9 nm results from vibrationally hot SiH₂ through a sequence of (visible) photoexcitations. The hot radical is decomposed by the absorption of a single visible photon to form H₂ and Si ($^1D_2$).[10] The silicon atom is next ionized in a [2 + 2] REMPI process. The two-photon resonance to the $4p$ $^1P_1$ state is expected[11] at a wavelength of 487.98 nm. The dye laser pulse energy dependence of the signal at 487.9 nm is linear. The rate-limiting step is therefore assigned to the production of the silicon atom from the hot silylene, and the signal is proportional to the density of this radical.

The broad feature around 500 nm is due to SiH₂ via a [3 + 1] REMPI. The intermediate resonance is expected to be a Rydberg level that is broadened due to overlapping vibrational levels. The ionization potential of SiH₂ is 9.01 eV,[12] so that the long wavelength limit for a [3 + 1] ionization is 550 nm. The Rydberg levels of SiH₂ are not known, but can be estimated with assumptions about the quantum defects δ. Assuming δ = 0, the n = 3 level would be expected around the energy of three 495 nm photons. Using the δ values discussed by Olbrich[13] for SiH₃ we estimate levels for the 4d state at 511 nm and the 5s state at 495 nm. The broad feature has a maximum near 500 nm primarily because of the power curve for coumarin 500 dye.

The time dependence of the total REMPI signals at these two wavelengths is shown in a semilog plot in Fig. 3. The dilution rate constants are determined from the total signal after subtracting the signal (at a delay of 90 ms) due to the precursor and stable products. The observed k_d are 6.3 × 10⁴ and 5.8 × 10⁴ s⁻¹ for 487.9 and 500 nm, respectively. The agreement between these two values suggests that the species responsible for these signals have the same mass; however, k_d can be larger if the species are formed with significant amounts of kinetic energy. The extent of decrease of
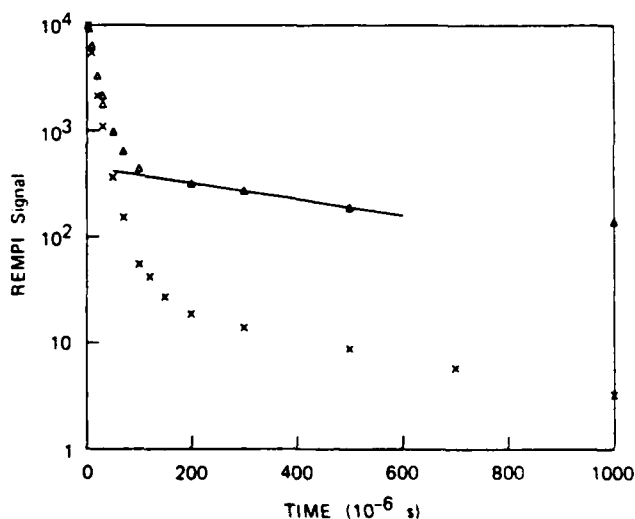
FIG. 3. Time dependence of the normalized total REMPI signals at 487.9 nm (boxes) and 500 nm (circles). The solid line is drawn through the portion of the data used to determine γ. The pressure was 1.3 × 10⁻⁵ Torr and the extent of depletion was 10%. The dye laser pulse energy was 2.3 mJ for the 500 nm data. For the 487.9 nm data the dye laser pulse energy was 0.1 mJ for the early time data and 1.5 mJ for the late time data. These separate data sets were then normalized at 100 μs.

the signal in this early time period also contains valuable information. If the IR beam were uniform and the radicals had a low γ, then the extent of decrease of this signal would be entirely due to the dilution effect. The value would then be the ratio of the IR beam volume to the volume of the inner tube. This ratio is approximately 5 for our conditions. The fact that the extent of decrease of the signal at 500 nm is larger (factor of 20), suggests that the IR beam is not uniform. There are hot spots in the IR beam, so that the effective beam volume is somewhat smaller than expected. The fact that the 487.9 nm signal decreases by a factor of 500 in this early time must be explained by a rapid wall loss of the hot SiH_2. The hot radical may be lost on the wall or it may lose energy and be returned to the gas. For this second situation the appropriate parameter is the energy accommodation coefficient. In either case we conclude that γ is greater than 0.5 for SiH_2.

The first-order loss during the period 0.1–1 ms is determined from the total signal after subtracting the slowly decreasing contribution from the precursor and stable products. This correction is determined by extrapolating back the signal between 2 and 5 ms. The corrected data (for $0.1 < t < 1$ ms) gives a straight line in a semilog plot. The data at 0.1 ms is too high because of a contribution from the dilution effect, and the data at 1 ms is uncertain because of the subtraction. The first-order loss rate constants for the 487.9 and 500 nm features are 2.7×10^3 and $3.2 \times 10^3 s^{-1}$, respectively. At this time the signals at both wavelengths are due to thermal SiH_2 through $[3 + 1]$ REMPI.

We interpret these loss rate constants as being due to wall reactions and can calculate the sticking coefficients, $\gamma = 0.09$ and 0.11 for the 487.9 and 500 nm signals, respectively. The gas phase insertion reaction is expected to be slower than the observed loss rates because the reaction will be in the pressure fall-off regime. In order to verify this assumption it will be necessary to perform pressure-dependent experiments to measure the insertion rate constant. The de-

rived sticking coefficient will be reduced by the extent to which the insertion reaction is occurring.

The average γ value of 0.1 for thermal SiH_2 is smaller than expected for an amorphous silicon surface, but is reasonable for a silicon-carbon surface. The insertion of a SiH_2 into a C—H bond in the gas phase is much slower than the insertion into an Si—H bond. γ will certainly vary with the chemical nature of the surface, the temperature, and the presence of bombardment by ions, electrons, or photons. This experiment has demonstrated the ability to directly measure radical sticking coefficients. The technique can be expanded to study other radicals and other surfaces. The reactivity with the surface during deposition conditions can be simulated by appropriate preconditioning or simultaneous conditioning of the surface for the IRMPD/REMPI experiment.

[1] M. E. Coltrin, R. J. Kee, and J. A. Miller, J. Electrochem. Soc. 133, 1206 (1986).

[2] M. J. Kushner, J. Appl. Phys. 63, 2532 (1988).

[3] J. M. Jasinski, B. S. Meyerson, and B. A. Scott, Annu. Rev. Phys. Chem. 38, 109 (1987).

[4] J. M. Jasinski and J. O. Chu, J. Chem. Phys. 88, 1678 (1988).

[5] R. M. Robertson, D. M. Golden, and M. J. Rossi, J. Vac. Sci. Technol. A 6, 1407 (1988).

[6] R. M. Robertson, D. M. Golden, and M. J. Rossi, J. Vac. Sci. Technol. B 6, 1632 (1988).

[7] J. S. Francisco, S. A. Joyce, J. I. Steinfeld, and F. Walsh, J. Phys. Chem. 88, 3098 (1984).

[8] B. A. Sawrey, H. E. O'Neal, and M. A. Ring, Organometallics 6, 720 (1987).

[9] J. W. Thoman and J. I. Steinfeld, Chem. Phys. Lett. 124, 35 (1986).

[10] J. S. Francisco, R. Barnes, and J. W. Thoman, J. Chem. Phys. 88, 2334 (1988).

[11] C. E. Moore, Selected Tables of Atomic Spectra (National Bureau of Standards, Washington, DC, 1967), NSRDS-NBS 3, Sec. 2.

[12] J. Berkowitz, J. P. Green, H. Cho, and B. Ruscic, J. Chem. Phys. 86, 1235 (1987).

[13] G. Olbrich, Chem. Phys. 101, 381 (1986).

Appendix H

ATOM- AND RADICAL-SURFACE STICKING COEFFICIENTS MEASURED
USING RESONANCE ENHANCED MULTIPHOTON IONIZATION (REMPI)

Submitted to J. Phys. Chem. (1989)

ATOM- AND RADICAL-SURFACE STICKING COEFFICIENTS MEASURED USING RESONANCE-ENHANCED MULTIPHOTON IONIZATION (REMPI)

Robert M. Robertson[†] and Michel J. Rossi[*]
Department of Chemical Kinetics
SRI International
333 Ravenswood Avenue, Menlo Park, CA 94025-3493

ABSTRACT

Sticking coefficients, γ, of neutral transient species at ambient temperature were measured using _in situ_ resonance enhanced multiphoton ionization (REMPI) of the transients in a low pressure reactor at mTorr pressure. The value of γ for I on a stainless steel surface was 0.16, whereas γ for CF_3 free radical was <0.01. The REMPI spectrum of SiH_2 was observed for the first time, and by the use of different REMPI transitions a value of 0.10 was found for $\gamma(SiH_2)$ on a growing carbon-containing hydrogenated silicon surface at ambient temperature. This value increased to 0.15 for interaction of SiH_2 with a growing surface containing exclusively Si and H. A lower limit for γ of >0.5 was found for highly vibrationally excited CF_3 containing 5900 cm^{-1} of internal energy and for SiH_2 containing 7000 cm^{-1} of internal energy. The surface was stainless steel in the former case and a carbon-containing Si and H in the latter case.

[†]Recent address: Applied Materials, Santa Clara, CA.

I. INTRODUCTION

The ever-shrinking dimensions of thin film devices and VLSI chips make control over the processes involved in VLSI chip production essential. Fundamental understanding of elementary reactions occurring in the gas phase and on the solid substrate is required to achieve this control. In both etching and deposition processes, energetic neutrals assume a leading role in homogeneous (gas phase) and heterogeneous (surface) reactions, even though the presence of ions often seems essential, for instance, in directional etching. The relative abundance of many of these energetic neutrals, such as atoms, free radicals, electronically excited metastable atoms and molecules, and vibrationally excited and other energetic species, may vary greatly according to their method of generation in such processes as chemical vapor deposition (CVD), physical and chemical sputtering, plasma-assisted deposition and etching, and various implantation methods. Consequently, understanding of these complex processes from a fundamental point of view will result from the study of "elementary" reactions that make up the complex reaction sequence and their subsequent incorporation into a chemical kinetics model.

Fundamental information on surface reactions has been determined from a variety of experiments. At one extreme are ultrahigh vacuum (UHV) experiments, in which atomically clean single crystal surfaces are exposed to reactive gases.[1,2,3] These experiments usually provide direct mechanistic insight into the rates and mechanisms of surface reactions, albeit at very low surface coverages, and the information derived from such UHV experiments may not be directly transferable to the applications of material processing because of the very different character of the

1

surface. At the other extreme is analysis of complex physico-chemical systems, in which neither the gas species nor the nature of the surface is accessed by direct observation.[4,5] In this case, a multitude of elementary reactions are assumed and the relevant rate parameters estimated in order to fit a macroscopic observable, such as film growth rate or etch depth, using a computer model. This approach is successful at optimizing a given process, but the results are not necessarily transferable to other similar processes. Between the two extremes are experiments conducted using practical surfaces with well-defined selected gas species.[6] These experiments, among which we include our efforts,[7-11] provide quantitative rates for specific processes that make up the input parameters for complex computer modeling calculations simulating the macroscopic process of interest.

Our contribution is in the field of elementary gas-surface processes of neutral transient species. Our approach has been to selectively generate a single atomic or molecular species using laser photolytic methods and to investigate its interaction with a given surface under experimental conditions that approach process conditions.

In this paper, we present results on the sticking coefficients of several atomic and molecular species on surfaces of practical interest. The term "sticking" is ambiguous in the case of wall deactivation of vibrationally excited species, because the process may correspond to energy rather than to mass accommodation. We use this term to describe the disappearance of the detected species owing to heterogeneous interaction with the surface of interest. Our emphasis is on the generation of a single atomic or molecular species by laser photolytic

2

methods and on _in situ_ real-time detection of the neutral transient species. We use a very low pressure photolysis (VLPΦ) reactor with mass spectrometry and resonance enhanced multiphoton ionization (REMPI) as diagnostic methods. REMPI provides real-time information on the density and loss rates of the transient species, and mass spectrometry of stable gases effusing from the reactor provides data on the loss of the precursor and formation of products of gas and surface reactions. The "active" surface for the reaction can be installed in the reactor in several ways depending on the requirements of the experiments; reactions can be studied on heated samples, as-grown samples, and technologically important materials, such as stainless steel, gold, or Teflon.

As an example of an atom-surface sticking coefficient, we chose I atom generated from CF_3I via IR-multiphoton decomposition (IR-MPD), whose loss on a stainless steel surface was monitored as a function of time. The behavior of I atom contrasted significantly with the heterogeneous deactivation kinetics of CF_3 on the same surface. As an example of a free radical surface sticking coefficient, we generated CF_3 by IR-MPD of hexafluoroacetone (HFA). Silylene, SiH_2, is thought to be an important species in polycrystalline and amorphous hydrogenated silicon (a-Si:H) deposition schemes. We generated SiH_2 via IR-MPD of n-butylsilane (n-$C_4H_9SiH_3$) and disilane (Si_2H_6) and studied its deposition kinetics on a growing silicon containing surface. Finally, we studied the heterogeneous deactivation kinetics of vibrationally highly excited CF_3I and SiH_2 in order to provide an example of contrasting behavior to that of ground-state molecular species.

3

II. EXPERIMENTAL

A. Apparatus

The photolysis reactor (Fig. 1) is made from a stainless steel six-way cross with a volume, V_R, of 620 cm^3. One axis is used for the IR photolysis laser and the other for the tunable REMPI (visible) laser. The bottom arm of the cross holds a butterfly valve with an interchangeable aperture mounted in the center. With the butterfly valve open, the reactor can be pumped down to a background pressure of 3×10^{-7} Torr. With the butterfly valve closed, the aperture (3 mm in diameter) determines the escape rate constant of the molecular species and forms an effusive beam for mass spectrometric sampling. The two REMPI electrodes, usually two wire loops made out of copper, are mounted on two electrical feedthroughs. Two 1/4-inch tubes are welded laterally to provide feedthroughs for the gas inlet and pressure measurement by means of a capacitance manometer.

A stainless steel tube coaxial to the IR photolysis laser beam supports the active surface for the sticking coefficient measurement and optimizes the REMPI sensitivity (see below). The tube has two holes in the center (1.5 mm) for the focused visible laser to enter and exit. In the center at 90 degrees to the REMPI laser beam, two slits (3 × 10 mm) have been cut to accommodate the REMPI electrodes, which protrude into the tube by about 1 mm. The inner diameter of the tube is 16.5 mm and its length is 210 mm, leaving a gap at the KCl windows of 1-2 mm. This gap was reduced in some experiments by placing sliding cylinders of shim stainless steel at the ends of the tube. The gap at the window was subsequently reduced to less than 1 mm. The area, A_{eT}, through which gas

could escape from inside the tube to fill the main reactor is 1.7 cm^2 without the shims and 0.7 cm^2 with the shims in place. The volume, V_T, and surface area, A_T, of the tube are 45.4 cm^3 and 113 cm^2, respectively.

The IR-MPD of the precursor gases is accomplished using a pulsed CO_2 laser (Tachisto model 555, TEA). The beam was collimated using reflective optics and sent through the VLPΦ reactor, resulting in a cross-sectional area of ~0.5 cm^2 and path length of 21 cm. The available pulse energy depended on the wavelength and was typically 1 J per pulse. CF_3I was decomposed using the 9.4-μm (R12) line with the beam traversing through the cell in single pass. HFA was decomposed using the 10.4-μm (R12) line with the beam retroreflected through the cell to achieve a fluence sufficient to decompose significant quantities of the precursor. n-Butylsilane and disilane were decomposed using the 10.4-μm (P20) line using single pass and double pass of the IR beam, respectively.

REMPI was accomplished using an excimer (Lumonics Hyperex 460, XeCl at 308 nm) pumped dye laser (Lambda Physik FL2002). Various dyes were used to study REMPI of different radicals and to scan different wavelength regions of a specific radical (coumarin 500, coumarin 503, coumarin 470, BBQ, DMQ, and p-terphenyl). Typical pulse energies are presented together with the data in the illustrations. The laser beam was focused into the inner tube by a 70-mm focal length lens. The ions and electrons were collected[9] on wire electrodes with bias potentials of minus and plus 90 V, respectively. These currents were amplified and differentially added before averaging using a box car. The time delay between the IR photolysis laser and the visible REMPI laser constituted the independent

5

variable in the sticking coefficient measurements and was controlled by a digital delay generator.

The mass spectrometer was used primarily to monitor the extent of depletion, f, of the precursor gases by IR-MPD. In one experiment, a product species, n-butyldisilane, was observed at the parent ion mass. However, since an authentic sample was not available, we were not able to obtain absolute rate data.

B. Model of VLPΦ

The VLPΦ/REMPI experiment is a low pressure, flowing-gas experiment in which we use the pump-and-probe technique to study the decay kinetics of gas-phase species. The repetition rate of the pulsed lasers, 10 or 11 Hz, is a compromise between slow pulse repetition rates (which allow fresh precursor gas to fill the cell and stable product species to escape between laser pulses) and fast rates (high duty cycle). The characteristic rate constants within a pulse period are discussed below and summarized in Table I.

The precursor gas undergoes collisionless IR-MPD during the $\sim 2/\mu s$ laser pulse. Immediately following generation of the transient species within the irradiated cross section (beam volume) of the inner tube, the transient undergoes free molecular flow to fill the inner tube volume. The density of a transient in the IR beam beam volume decreases with a rate constant, k_d, determined by the thermal velocity, υ, of the transient and the geometry of the irradiated volume. After several dilution lifetimes (~ 0.1 ms), the species reachs a uniform density in the inner tube. The extent of density decrease in the IR beam volume on this time

6

scale is defined as the dilution factor, C_d. For species without gas or wall reactions on this time scale, the value of C_d is the ratio of the effective IR beam volume to the volume of the inner tube. An important function of the inner tube is to minimize C_d and thus increase the REMPI sensitivity.

On the 0.1- to ~10-ms time scale, the transient species undergo wall and gas reactions. The wall collision frequency, ω, given by the expression in Table I is larger than or comparable to the gas-gas collision frequency for our low pressure conditions. The loss rate constant, k_1, of the transient species in this time period is the parameter of primary interest here and is used to determine the sticking coefficient, γ,

$$\gamma = k_1 \, / \, \omega \qquad\qquad (1)$$

The sticking coefficient is a phenomenological quantity representing any mechanism that irreversibly removes a species from the gas.

On the time scale of 1- to 10-ms, molecules escape the inner tube with the rate constant k_{eT} and fill the main reactor volume (Table I). On the time scale of seconds, the molecules escape from the main reactor through the exit aperture with the rate constant k_{eC}. On this same time scale, fresh precursor gas enters the reactor.
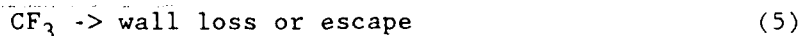
REMPI is used to monitor the time-dependent density of a specific transient species in the reactor. Because the focus of the visible laser is located in the IR beam volume, we can observe the density of the transient species during and immediately after the IR pulse as well as

monitor the decrease in density due to the dilution effect. After the dilution has occurred, REMPI monitors the time dependence of the uniform density in the inner tube. The total REMPI signal has contributions from the precursor and stable product molecules, so that to make corrections, must be made before the signal can be used to describe the kinetics of the transient species. Stable species generally have small cross sections for multiphoton ionization; however, they can contribute significantly to the signal because of their large densities. The amount of signal from the precursor and stable products can be determined from the total signal immediately before the IR pulse (at 90 ms) or after the transient species are expected to have disappeared (2-5 ms). The signal contribution from stable products can be minimized by operating at low pressures and low degrees of depletion.

III. RESULTS

A. I and $CF_3I^{\ddagger}$

Ground-state I atoms and $CF_3I^{\ddagger}$ are generated[9] using IRMPD of CF_3I. The important reactions in this system are listed in equations (2) through (7):

$$CF_3I + nh\nu \rightarrow CF_3 + I \tag{2}$$

$$\rightarrow CF_3I^{\ddagger} \tag{3}$$

$$CF_3 + CF_3 \rightarrow C_2F_6 \tag{4}$$

$$CF_3 \rightarrow \text{wall loss or escape} \tag{5}$$

$$I \rightarrow \text{wall loss} \tag{6}$$

$$CF_3I^\ddagger \rightarrow CF_3I \text{ (gas or wall collisions)} \qquad (7)$$
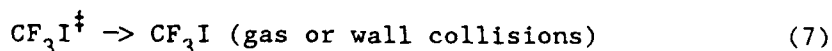
$I^*(p^5\ ^2P_{1/2})$, the upper spin state of I, is not generated directly by IRMPD, and there are no fast gas-phase reactions of I.

We discuss two transitions that are characteristic of I and $CF_3I^\ddagger$. The transition at 474.5 nm results from [3+2] REMPI of I generated directly by IRMPD of the CF_3I [Eq. (2)]. The resonant process is the three-photon excitation from the ground state of $I(5p^5\ ^2P_{3/2})$ to the excited state, $I^{**}(6s\ ^2P_{1/2})$ [Fig. 2(a)]. The peak of the observed transition is slightly blue-shifted from the expected resonance wavelength,[12] 474.8 nm, presumably owing to Stark broadening. The transition at 477.8 nm results from prior single-photon dissociation of $CF_3I^\ddagger$ generated according to Eq. (3). According to Fig. 2(b), the first step in the resonant excitation is the visible-photon-induced decomposition of $CF_3I^\ddagger$ to generate the spin-orbit excited iodine atom, I^*. I^* is subsequently ionized via [3+1] REMPI starting from the $5p^5\ ^2P_{1/2}$ level to the resonant $6s\ ^2S_{1/2}$ level. Again, the peak of the observed transition is presumably Stark-shifted from the expected resonance,[12] 478.1 nm. This signal is proportionate to the density of vibrationally hot $CF_3I^\ddagger$ that has sufficient internal energy (> 5900 cm^{-1}) to allow the formation of I^* with the absorption of a single visible photon. We correct for the contributions to the signals at both wavelengths from the parent gas and I_2.

The time dependence of the total REMPI signal at these two wavelengths is shown in Fig. 3 for the first millisecond after the IR laser

9

pulse. The initial CF_3I pressure was 1.1×10^{-3} Torr, the depletion was approximately 2% (measured using the mass spectrometer), and the laser pulse rate was 11 Hz. Because no significant secondary reactions destroy or re-form CF_3I, we use the extent of depletion to calculate the initial density of I formed in the IR beam volume, 1.1×10^{12} cm^{-3}. The signal at 474.5 nm falls rapidly during the first 100 μs as the I atoms move out of the IR beam volume. The dilution rate constant, k_d, and dilution factor, C_d, shown in Table II, are derived from the total signal after subtracting the background signal from the precursor and molecular iodine. This correction can be approximated by the signal that is present immediately before the IR laser fires, i.e., the signal at a delay time of 90 ms; k_d is in reasonable agreement with the approximate expression in Table I. The C_d of 4.2 is in agreement with the value expected if the IR-MPD is occurring in the entire IR beam volume.

Between 0.1 and 1 ms, the signal decreases owing to the first-order loss of I on the walls. The rate constant is derived from the total signal after subtracting the background at 2 ms. Using k_1, we calculate a sticking coefficient of 0.16 for I according to Eq. (1). The active surface for this measurement was stainless steel, possibly with the some adsorbed atomic or molecular iodine, and a fluorocarbon polymer $(CF_x)_y$. In our previous experiment with this precursor, we estimated values for γ of 1.2×10^{-2} and 6.2×10^{-2} using a less sensitive technique. This result is in contrast to results[13] in a low pressure reactor for a different halogen atom, Br, on PTFE (polytetrafluoroethylene), where γ is reportedly very small and the wall loss is negligible relative to gas-phase reactions.

The time dependence of the total REMPI signal at 477.8 nm is qualitatively different from that at 474.5 nm (Fig. 3). It decreases rapidly to a constant level; k_d and C_d are derived as discussed above, and the resulting values are shown in Table II. The C_d value of 8 is larger than observed for the 474.5-nm signal and is consistent with the rapid loss of the $CF_3I^{\ddagger}$ due to wall collisions. The wall loss rate is comparable to the dilution rate, and this technique cannot differentiate extremely rapid chemical loss from molecular flow diffusion. It is thus not possible to measure an accurate value for γ of $CF_3I^{\ddagger}$, except to estimate a lower bound of 0.5. A large γ (corresponding to energy accommodation) is expected for molecules with this extent of vibrational excitation and with relatively closely spaced vibrational levels. The internal energy content of $CF_3I^{\ddagger}$ approximately corresponds to the excitation of every normal mode by one quantum. This quenching behavior is analogous to that exhibited in the heterogeneous deactivation of highly vibrationally excited azulene ($C_{10}H_8^{\ddagger}$) on quartz (SiO_2) walls.[14,15] Similarly to the present case, the internal energy content of $C_{10}H_8^{\ddagger}$ was about one quantum of vibrational energy per vibrational degree of freedom.

B. CF_3 Free Radical

We used hexafluoroacetone (HFA) as the precursor for CF_3 radicals instead of CF_3I because of the large REMPI signal contribution from the parent CF_3I molecule. The chemistry of the low pressure IR-MPD of HFA has been discussed previously[10] and is summarized in the following reactions:

$$HFA + nh\nu \rightarrow CF_3 + COCF_3 \qquad (8)$$

$$CF_3 + CF_3 \rightarrow C_2F_6 \qquad\qquad (9)$$

$$CF_3 + COCF_3 \rightarrow HFA \qquad\qquad (10)$$

$$CF_3 \rightarrow escape \ or \ wall \ loss \qquad\qquad (11)$$

$$COCF_3 \rightarrow escape \ or \ wall \ loss \qquad\qquad (12)$$

The REMPI spectrum of CF_3 was studied in detail by Duignan et al.[16] The process is a [3+1] REMPI in the 420- to 490-nm wavelength region, as depicted in Fig. 2(c). To study the heterogeneous kinetics of this species, we set the wavelength of the tunable dye laser to the peak of the REMPI transition at 455.6 nm. The small signal contribution from the precursor and stable products (signal without the photolysis laser) has been measured and used to determine the signal from CF_3.

The time dependence of the total REMPI signal is shown in Fig. 4 for an experiment with 1.1×10^{-3} Torr of HFA and a depletion of 10% at the laser pulse rate of 11 Hz. At low pressure, reaction (10) is slow, so the depletion can be used to calculate the initial density of CF_3 formed in the IR beam volume. Assuming that the entire IR beam volume is active, the initial CF_3 density was 6.1×10^{12} cm^{-3}. The REMPI signal decreases rapidly in the first 100 μs and then reaches a constant level; k_d and C_d are derived from the total signal after the background signal at 90 ms is subtracted. The C_d value of 14 is smaller than that observed for I but is still attributed to the dilution effect because the effective IR beam

volume is expected to be smaller when the IR beam is retroreflected through the reactor and when the reaction is more endothermic. The constant signal up to 1 ms is interpreted in terms of a low γ, too small to be determined quantitatively in the present experiment, which yields only an upper limit of $\gamma \leq 0.01$. The active surface for this experiment is stainless steel, again with the likely presence of an adsorbed fluoro-carbon polymer adhering to the metal oxide surface. We had determined that γ for CF_3 was 1.6×10^{-4} in the CF_3 etching experiment[8] and 2.2×10^{-5} in the HFA gas-phase kinetics experiment.[10] We conclude that CF_3 free radical is a very inert species at ambient temperature on quartz and metal and semiconductor surfaces.
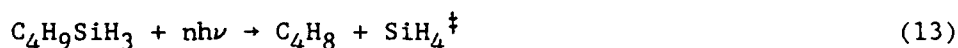
C. SiH_2 and $SiH_2^{\ddagger}$

We discuss the sticking coefficients of SiH_2 and $SiH_2^{\ddagger}$ produced from n-butylsilane and Si_2H_6. First, we discuss the IR-MPD-driven gas-phase chemistry and the REMPI transitions characteristic of the species; then we discuss the observed first-order loss rate constants in the n-butylsilane system at several REMPI wavelengths and as a function of pressure. In this system, the surface is a growing amorphous hydrogenated silicon-carbon alloy. Finally, we present results on the SiH_2 losses with disilane as a precursor, which gives rise to an amorphous silicon surface.

1. Gas-Phase Chemistry

The IR-MPD[17] of n-butylsilane (n-$C_4H_9SiH_3$) has been investigated previously, and two initiating mechanisms are used to explain the observed stable products. Eq. (13) represents the four-center elimination of

13

vibrationally excited silane, which decomposes according to Eq. (14) upon further absorption of IR radiation. Eq. (15) represents the 1,2- or 1,1-H_2 elimination, which is followed by the secondary IR-MPD of n-butylsilylene, Eq. (16).

$$C_4H_9SiH_3 + nh\nu \rightarrow C_4H_8 + SiH_4^{\ddagger} \qquad (13)$$

$$SiH_4^{\ddagger} + nh\nu \rightarrow SiH_2 + H_2 \qquad (14)$$

$$C_4H_9SiH_3 + nh\nu \rightarrow C_4H_9SiH + H_2 \qquad (15)$$

$$C_4H_9SiH + nh\nu \rightarrow C_4H_8 + SiH_2 \qquad (16)$$

$$C_4H_8SiH_3 + SiH_2 \rightarrow C_4H_8Si_2H_5 \qquad (17)$$

$$\rightarrow C_4H_9Si_2H_3 + H_2 \qquad (18)$$

$$SiH_2 \rightarrow wall\ loss \qquad (19)$$

Francisco et al[17] favored the first initiating mechanism for the decomposition of the organosilane [Eq. (13) and (14)], whereas Sawry et al.[18] favored the thermal decomposition mechanism analogous to Eqs. (14) and (16) based on the results of their shock tube study. In some thermal and IR-MPD studies of other alkylsilanes,[19-21], mechanisms analogous to Eqs. (15) and (16) were favored. Which initiating mechanism is dominant is not critical to our results as long as the secondary photolysis takes

14

place within the IR laser pulse. The important point is that SiH_2 is an intermediate, as was confirmed for n-butylsilane by Thoman and Steinfeld.[22] The silylene radical can undergo a gas phase insertion reaction with the precursor to form n-butyldisilane (Eq. (17)] and possibly n-butyldisilylene Eq. (18)]. The insertion rate constants of silylene into several types of chemical bonds[23-25] have been studied at high pressure (in the Torr range), and the rate constant for n-butylsilane is expected to be comparable to that for phenylsilane,[23] 1.1×10^{-10} cm^3 s^{-1}. The rate constant may be somewhat slower under our conditions because of the unimolecular fall-off effect operating at low pressure. The other primary loss reaction of silylene is the wall reaction, Eq. (19). These two loss reactions are fast, so silylene is not expected to survive long enough to escape the reactor or to undergo secondary gas-phase reactions with minor gas phase products.

No detailed studies of the IR-MPD of disilane, Si_2H_6, have been performed, although there have been reports of thin film deposition[26, 21] by this process. IR absorption studies[28] show absorption in the 10.6-μm band. Detailed studies of IR decomposition [29] of SiH_4 have demonstrated enhancement by collisions (rotational hole burning). Disilane decomposition is probably similar, being slow in the collisionless regime. The primary reaction is expected to be identical to the thermal decomposition,[30] namely, elimination of SiH_2.

$$Si_2H_6 + nh\nu \rightarrow SiH_4 + SiH_2 \qquad (20)$$

$$SiH_2 + Si_2H_6 \rightarrow Si_3H_8 \qquad (21)$$

15
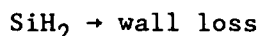
$$SiH_2 \rightarrow \text{wall loss} \qquad\qquad\qquad\qquad (22)$$

The wall reaction, [Eq. (22)] is expected to be fast in analogously to the insertion reaction, [Eq. (21)] because SiH_2 is expected to insert into Si-H bonds on the surface.

2. REMPI Spectra

We investigated the REMPI spectrum of SiH_2 in our total ion collection system because it had not been reported in the literature. Assignment of the origin of the REMPI transitions is based on examining different precursor gases that generate the SiH_2 species and scanning different wavelength regions and is significantly different from the assignment for SiH_3.[31]

The REMPI spectrum from n-butylsilane around 500 nm and recorded 20 μs after the IR pulse is displayed in Fig. 5. It is primarily due to a transient species with only a small contribution from the precursor and stable molecules. Nearly identical but weaker spectrum results from the IR-MPD of disilane (Fig. 6). We conclude that the transient species responsible for this REMPI spectrum must be common to both gases. The transient species are SiH_2 and $SiH_2^{\ddagger}$, and we discuss the origin of the REMPI transitions below. The only other species likely to be generated from both these precursors are SiH_4 and $SiH_4^{\ddagger}$. Because the signals produced from an authentic sample of SiH_4 are small, we conclude that the large transient signals are not due to SiH_4. It is highly unlikely that the vibrational excitation of the SiH_4 would sufficiently increase the

16

ionization efficiency to account for the observed transient signal strengths. SiH_3 is neither expected to be a product of the IR-MPD of n-butylsilane or disilane nor has it been observed or inferred from such experiments.

The sharp peak in the REMPI spectrum at 487.9 nm is due to vibrationally excited SiH_2, i.e., $SiH_2^{\ddagger}$, whose internal energy is equal to or greater than 7000 cm^{-1} that is excited through a sequence of visible photon excitations displayed in Fig. 7. The hot radical is formed in the collisionless IRMPD process and decomposes as a result of the absorption of a single visible photon to form H_2 and $Si(^1D_2)$[32,33] from predissociation out of the A state of SiH_2. The excited silicon atom is subsequently ionized via a [2+2] REMPI process. The two-photon resonant state in $Si(^1D_2)$ is the $4p^1P_1$ state and is expected[12] at a wavelength of 487.98 nm. The REMPI signal at 487.9 nm is linear in dye laser pulse energy, an unusual situation in view of the many photons required to ionize $SiH_2^{\ddagger}$. We conclude that the rate-limiting step in the overall REMPI process corresponds to the generation of the silicon ($^1D_2$) through predissociation of the A state of $SiH_2^{\ddagger}$, with the REMPI signal proportionate to the density of $SiH_2^{\ddagger}$.

The broad feature in the REMPI spectrum around 500 nm is due to [3+1] REMPI of SiH_2. The resonant state is most likely a Rydberg state broadened by overlapping vibrational levels. The ionization potential of SiH_2 is 9.01 eV,[34] so that the long wavelength limit for a [3+1] ionization is 550 nm. The Rydberg states of SiH_2 have not been studied in detail, but their energies can be estimated from the Rydberg formula assuming a certain size for the quantum defect, δ. Assuming $\delta = 0$, the n

- 3 level is expected at an energy equivalent to three 495-nm photons (see also the δ values discussed by Olbrich[35] for SiH_3). The broad transition in this wavelength range has a maximum near 500 nm as shown in Fig. 5, primarily because of the power curve of the coumarin 500 dye. The maximum of the REMPI signal in Fig. 6 is shifted slightly with respect to Fig. 5 because of the use of a different dye with its associated slight shift in the power curve.

Figs. 8 and 9 display REMPI spectra in the wavelength regions 335 to 345 nm and 345 to 370 nm, respectively, using n-butylsilane as a precursor. Spectra from disilane are qualitatively similar in both wavelength ranges. The spectra are due to SiH_2 and result from excitation mechanisms analogous to those displayed in Fig. 7. The sharp transitions observed between 360 and 367 nm are due to [2+1] REMPI of $Si(^1D_2)$ atoms formed by single UV photon dissociation of SiH_2. The resonant states are thought to correspond to 5f and 6p atomic states.[12] In this wavelength range, the first UV photon samples ground-state SiH_2 because single-photon excitation at these shorter wavelengths provides sufficient energy for predissociation of the ground state. An expanded view of the signal at 363.5 nm reveals four transitions in keeping with expectation from atomic level energies and symmetries.[12] Furthermore, this REMPI signal was linear with the dye laser pulse energy, just as the 487.9-nm feature, so that the rate-limiting step in the overall REMPI process is attributed to the single-photon predissociation from $SiH_2(A)$. The other transitions and the broad background are due to [3+1] REMPI of SiH_2 through molecular Rydberg states, since the long wavelength limit for the [2+1] REMPI is 412 nm and the limit for [1+1] REMPI is 275 nm. The signals at 340 and

18

349.3 nm increased quadratically with the dye laser pulse energy, consistent with two-photon absorption to the resonant state.

3. Interaction of SiH_2 With the Silicon-Carbon Surface

We describe the measurement of heterogeneous loss rate constants for SiH_2 and $SiH_2^{\ddagger}$ produced by IR-MPD of n-butylsilane by analyzing the time dependence of REMPI transitions characteristic of these species. The surface of the inner tube during these experiments was not characterized in detail but was probably a hydrogenated silicon-carbon alloy, similar to that formed by IR-MPD of phenylsilane.[17]

The time dependence of the total REMPI signals at 487.9 and 500 nm are shown in Fig. 10 for a pressure of 1.2×10^{-3} Torr and a depletion of ~1-10% at 11 Hz. Assuming that each decomposed n-butylsilane molecule generates one silylene radical and no significant secondary reactions destroy (however, see below under Pressure Dependence) or regenerate the precursor, we calculate an initial silylene density of 9×10^{12} cm^{-3}. We have assumed that the entire IR beam volume was effective for IR-MPD, and we therefore view the above quoted number as an upper limit (see below). The initial rapid decrease in signal is due to the transient species dispersing from the IR beam volume to fill the inner tube. The k_d and C_d values in Table II are determined from the total REMPI signal after the signal contribution from the precursor and stable products have been substracted. This correction was determined from the total REMPI signal at a delay time of 90 ms with no transient species remaining. The agreement in the k_d values (6.3×10^4 and 5.8×10^4 s^{-1} for $SiH_2^{\ddagger}$ and SiH_2, respectively) suggests that the signals are due to species of equal

mass, barring any translational energy release as a result of IR-MPD.

The dilution factors, C_d, for these two species are very different. The C_d value of 20 for SiH_2 is larger than that observed for I but comparable to that observed for CF_3. The numerical value is associated with the ease with which the precursor undergoes IR-MPD. The quantitative expression for this case is the yield versus fluence curve of the precursor, which varies widely according to the nature of the precursor and the irradiation parameters. The effective IR beam radius (or volume) is expected to be smaller than the total IR beam volume because the generation of SiH_2 by IR-MPD of n-butylsilane is a multistep process. Only the most intense portions of the IR beam will cause SiH_2 generation. The much larger C_d value of 200 for $SiH_2^{\ddagger}$ must be explained by the fact that the time scales of molecular diffusion and ensuing rapid wall loss for this species cannot be separated, similarly to the situation for $CF_3I^{\ddagger}$. This rapid wall loss can be due to adsorption (mass accommodation) or energy transfer (energy accommodation). The data for this expanded time scale therefore do not show a distinct break between dilution and wall loss. Thus we are only able to give an upper limit for γ of 0.5.

The first-order loss rates during the period 0.1 to 1 ms are determined from the total REMPI signal after the slowly decreasing contribution from the precursor and stable products has been substracted. This correction is determined by back-extrapolating the signal recorded between 2 and 5 ms. The rate constant for the slowly decreasing REMPI signal after 2 ms was 200 s^{-1}, the source of which was not thoroughly investigated for these experiments. The corrected data

20

from Fig. 10 and for other experimental conditions discussed below fall on straight lines in a semilog plot. The data point at 0.1 ms is slightly too high because of incomplete dilution at this time. The data point at 1 ms may be somewhat uncertain because of the subtraction procedure. The k_1 values derived for this part of the REMPI signal decay at both 500 nm and 487.9 nm are displayed in Table II and are comparable because the signals at both wavelengths are due to the heterogeneous reaction of thermal SiH_2 monitored through [3+1] REMPI. On the time scale of 0.1 to 1 ms, $SiH_2^{\ddagger}$ has already decayed to zero, and the residual REMPI signal monitors thermalized (ground-state) SiH_2 via REMPI of the molecular Rydberg state similarly to REMPI at 500 nm (triangles in Fig. 10).

We interpret these k_1 values in the next section, where the pressure dependence of k_1 is presented. We take k_1 determined at the lowest presssure, assuming that the loss described by k_1 is due entirely to wall collisions, and we find sticking coefficients, γ, of 0.09 and 0.11 when using the 487.9 and 500 nm REMPI signals, respectively. In calculating γ, we compare k_1 from Table II to ω from Table I, which acts as the internal clock for heterogeneous interaction. Few chemical processes can compete on this time scale, so we are certain that the pressure-independent component of k_1 can be interpreted as a purely heterogeneous interaction.

The time dependence of SiH_2 REMPI transitions at other wavelengths (340, 349.3, and 363.5 nm) were analyzed in the same manner, and the results are listed in Table II. The total time-dependent REMPI signal at one of these wavelengths (349.3 nm) is shown in Fig. 11. We note the good consistency in the results for k_1 at these different wavelengths, taking into account the different REMPI mechanisms (predissociation via SiH_2

21

A-state versus molecular Rydberg excitation) in that wavelength range and probing the same (ground-state) SiH_2 species. We recall that REMPI at 363.5 nm probes the SiH_2 ground state owing to the increased photon energy with respect to REMPI at 487.9 nm. All these experiments were performed at pressures near 1×10^{-3} Torr, which was a good compromise between signal strength and minimal gas-phase reactions.

Two additional tests were performed to verify that k_1 was due to a heterogeneous reaction with the vessel walls. In one experiment, the inner tube was coated with graphite (Aerodag) to change the character of the surface and the SiH_2 sticking coefficient. However, the silicon-carbon thin film formed rapidly enough that the surface was no longer graphitic when the REMPI data were taken. For instance, at a pressure of 1×10^{-3} Torr, a depletion of 10% and, assuming one surface site is covered for each precursor molecule decomposed, less than 100 seconds are required to form a monolayer of fresh film over the entire inside surface of the inner tube. This effect prevented us from studying different surfaces in this series of experiments. In the second test, k_{eT} was decreased by reducing the gap between the cell windows and the inner tube. No change in k_1 was observed, thus eliminating the possibility that k_1 corresponded to an escape rate constant rather than referred to a heterogeneous rate constant. Thus, we are certain that k_1 describes a chemical (sticking) rather than a physical (escape) process.

4. Pressure Dependence of k_1

We studied the pressure dependence of k_1 to determine the relative contributions of homogeneous and heterogeneous reactions. A set of k_1

22

rate constants measured at 495 nm and at depletion levels below 5% are plotted versus pressure in Fig. 12(a). The same variation in k_1 was observed for data at 349.3 nm and 495 nm. The apparent decrease in k_1 is caused by the increasing contribution of the REMPI signal of the insertion product that results from the insertion of SiH_2 into n-$C_4H_9SiH_3$ on this time scale. The product may be the stable n-butyldisilane, which is expected to have a small REMPI probability, or n-butyldisilene formed in a chemical activation reaction, which is expected to have a large REMPI probability. Despite this complication, the zero pressure intercept still represents the wall loss rate constant. Because the change in k_1 between 1 and 2×10^{-3} Torr is small, we interpret the data near 1×10^{-3} Torr as representing the zero pressure intercept and use it to derive γ.

At higher pressures, k_1 shows a positive slope, which normally is used to derive the rate constant for the insertion reaction of SiH_2 into the precursor. The value derived from this data, 4×10^{-12} cm^3s^{-1}, is much lower than typical rate constants measured at higher pressures. The unimolecular fall-off effect may not fully reconcile the absolute magnitude of this rate constant, so these REMPI data cannot be used to derive an insertion rate constant because of the REMPI signal contribution from the insertion product.

We performed two mass spectrometry experiments to gain qualitative information on the insertion reaction. The formation of the stable insertion product, n-$C_4H_9Si_2H_5$, was verified by observing a signal at the parent mass, m/e - 118 displayed in Fig. 13. The second experiment consisted of monitoring the mass peak at m/e - 88 versus n-$C_4H_9SiH_3$ pressure at constant IR laser fluence. The results are shown in Fig.

23

12(b) as the ratio of the signal with the IR laser "on" to the signal with the IR laser "off". In this pressure range, we verified that the absorption of the IR laser radiation is negligible, and thus we can assume that the extent of the IR-MPD of the precursor was constant. At low pressure (≤ 1 mTorr), the relative signal can be used to determine the extent of IR-MPD of $n\text{-}C_4H_9SiH_3$ (~15%) because the rate of secondary reactions destroying or regenerating the precursor is slow. As the pressure increases, the normalized signal at $m/e = 88$ increases owing to a contribution from the electron impact-induced dissociative ionization of heavier mass product species, such as $n\text{-}C_4H_9SiH_3$. These two experiments confirm that the insertion reaction occurrs under our experimental conditions.

5. Sticking Coefficient of SiH_2 on a Silicon Surface

To study the sticking coefficients of SiH_2 and $SiH_2^\ddagger$ on a silicon surface, we had to use a precursor gas that does not contain carbon. We chose disilane, Si_2H_6, because it produces hydrogenated amorphous silicon thin films by IR-MPD. Although the surface produced from this precursor is more relevant to CVD processes, it had been studied less thoroughly than the surface produced from decomposition of $n\text{-}C_4H_9SiH_3$ because IR-MPD of Si_2H_6 resulted in lower yields of SiH_2. We had to retroreflect the IR beam back through the cell to achieve sufficient fluence for decomposition, which was less than ~2%. The retroreflection setup posed experimental difficulties because the IR fluence reached the damage threshhold for the KCl windows (~2 J cm^{-2}) and the beam alignment had to

be near-perfect to avoid interaction between scattered IR radiation and the REMPI electrodes.

Results for SiH_2 and $SiH_2^{\ddagger}$ are shown in Fig. 14 and Table II for 2.6 mTorr of Si_2H_6. The early-time kinetics for $SiH_2^{\ddagger}$ are derived from the total REMPI signal at 487.9 nm, without corrections for the background signals from the precursor and stable products, since both REMPI signals are insignificant. The k_d and C_d values are comparable to the values observed using $n\text{-}C_4H_9SiH_3$. The large C_d value of 500 is due to the large γ for $SiH_2^{\ddagger}$ on amorphous silicon, similar to results using $n\text{-}C_4H_9SiH_3$. As for the n-butylsilane precursor, we assign a lower limit of 0.5 to γ. The fast time scale kinetics of SiH_2 are determined from the total REMPI signal at 495 nm after subtracting the background signal present at 90 ms. The resulting values for k_d and C_d are reasonable (Table II).

The k_1 for SiH_2 is derived from the total REMPI signal at 495 nm and the REMPI signal at 487.9 nm after the fast component due to $SiH_2^{\ddagger}$ decayed and after the signal from the precursor and stable products as represented by the signal at 90 ms was subtracted. This correction procedure is less rigorous than for $n\text{-}C_4H_9SiH_3$ but necessary because of the smaller signals. Using the data between 200 and 500 μs, we derive k_1 values of 4900 and 3400 s^{-1} for monitoring wavelengths of 495 and 487.9 nm, respectively. The discrepancy between these two values reflects the uncertainty in the experimental measurement for Si_2H_6 as a precursor of SiH_2. In Table II, the value of k_1 for Si_2H_6 is higher by 50% than that for the $n\text{-}C_4H_9SiH_3$ precursor. We attribute this increase in the sticking coefficient to the changed nature of the surface, which contains only Si-H bonds rather than both C-H and Si-H bonds.

Additional data were taken at 495 nm for various Si_2H_6 pressures. At 1.2×10^{-3} Torr, the REMPI signal decayed to the background level after 300 μs and a k_1 value could not be measured. The k_1 values of 4800, 3400, 2100, and 1400 s^{-1} were derived for pressures of 2.0, 3.0, 4.3, and 6.8 $\times$ 10^{-3} Torr, respectively. The values for the two lowest pressures are consistent with the data at 2.6×10^{-3} Torr. The values at higher pressure decrease significantly. The downward trend of the k_1 values with increasing precursor pressure may be due to a REMPI signal contribution from an insertion product, just as for $n-C_4H_9SiH_3$. However, the significance of these results should not be overemphasized, because of the possibility of a systematic error in the inherently smaller signals and because of the increasing importance of the correction with increasing pressure of the precursor. Using the low pressure k_1 values, we derive an average γ value of approximately 0.15 for SiH_2 on the surface formed by the IR-MPD of disilane that nominally corresponds to hydrogenated amorphous silicon.

6. Discussion of SiH_2 Results

Information on the sticking coefficient of SiH_2 (and the other simple silicon hydride radicals such as SiH_3 and SiH) is important for understanding the deposition mechanism of silicon-containing thin films, including amorphous or crystalline silicon, and the carbon, nitrogen, oxygen, and metal alloys of silicon. In recent years, the gas-phase reactivity of SiH_2 has been studied in detail, but there is no direct evidence of its surface reactivity. In some thermal and plasma deposition models,[36,37] SiH_2 has been assumed to have γ = unity on hydrogenated

26

amorphous silicon surfaces. In a classical trajectory model calculation,[38] γ of SiH_2 on a bare crystal silicon surface corresponding to atomically clean Si was found to be unity.

Our results, however, indicate that SiH_2 has a significantly lower value for γ on both hydrogenated silicon and silicon-carbon surfaces. Because of the lack of direct measurements and a theoretical model, we discuss these results in regard to the gas-phase reactivity of SiH_2. The assumption of unit γ on hydrogenated amorphous silicon was in part based on the following type of chemical intuition: SiH_2 is known to insert rapidly into Si-H bonds in the gas phase, so we expect it to insert rapidly into surface Si-H bonds as well. SiH_2 is known to insert slowly into alkanes in the gas phase, so we expect it to insert slowly into surface C-H bonds. Furthermore, our results are obtained for a surface at ambient temperature, whereas many modeling calculations refer to deposition conditions at higher temperatures, on the order of 150° to 300°C. A decrease in γ by a factor of 10 for the carbon-containing amorphous silicon surface or of 6 for the "pure" hydrogenated silicon surface in relation to the theoretical maximum value of 1.0 implies a small barrier to insertion of 1.4 and 1.1 kcal/mol, respectively. Such small barriers are very difficult to measure at higher temperatures, especially when the γ values are derived from modeling calculations based on macroscopic observables such as film growth rate. Thus, our results for silicon-carbon and pure silicon surfaces seem reasonable, albeit somewhat unexpected. The smaller value of γ in the case of the carbon-containing silicon surface may simply reflect the presence of C-H bonds with their associated lower reactivity toward SiH_2.

27

Our results for the pure silicon surface are not readily rationalized by these simple arguments. We would expect γ to be significantly larger than for a silicon-carbon surface, as assumed in the modeling studies. While the quality of the data using Si_2H_6 is not as good as that using $n\text{-}C_4H_9SiH_3$, we cannot explain our observed signals with a model other than one in which SiH_2 has a low γ. This result applies to our surface conditions only. High γ values may be valid under other conditions, such as higher surface temperatures and different surface compositions. High γ values should not be assumed for all surface conditions. Further experimental studies covering a wider range of conditions are needed.

IV. CONCLUSION

We introduced and validated an _in situ_ measurement technique for sticking coefficients of neutral transient species based on their real-time detection in a low pressure Knudsen cell. Advantages of this method are the absence of sampling artifacts and excellent spatial and temporal resolution, such as laser-excited fluorescence (LEF). The REMPI detection has the added convenience of being almost pressure independent and more generally applicable than LEF, especially for monitoring polyatomic species. However, it is intrusive in the sense that current collection electrodes are needed. Like LEF, it has excellent dynamic range, often as much as four orders of magnitude in signal. Results can be quantified easily by cross calibration using a quadrupole mass spectrometer. This procedure can also lead to the measurement of absorption cross sections of atoms, free radicals, and other energetic transient polyatomic species. This aspect of our technique could lead to a data bank of REMPI cross

28

sections and associated detection schemes for important transient species that are relevant under given processing conditions. Even rather complex kinetic situations consisting of competing first- and second-order reactions can be quantitated.

The surfaces of interest can be mounted easily in the low pressure reactor, and measurements can be performed even under film deposition conditions. Furthermore, we have demonstrated the possibility of measuring the kinetics of highly vibrationally excited transient species under reaction conditions and have presented results for excited radicals ($SiH_2^{\ddagger}$) and closed-shell species ($CF_3I^{\ddagger}$). The technique also has the capability of selecting a subset of excited molecular species with variable amounts of internal energy and of studying the dynamics of those species upon gas-wall and gas-gas collisions.

[1] S. Joyce, J. G. Langan, and J. I. Steinfeld, J. Chem. Phys. 88(3), 2027 (1988), and references therein.

[2] R. Buss, P. Ho, W. G. Breiland, and M. E. Coltrin, J. Appl. Phys. 63, 2808 (1988).

[3] S. M. Gates, Surf. Sci. 195, 307 (1988).

[4] J. Perrin and T. Broekhuizen, Appl. Phys. Lett. 50, 433 (1987).

[5]B. A. Scott, R. D. Estes, and J. M. Jasinski, J. Chem. Phys. $\underline{89}$(4), 2544 (1988); B. S. Meyerson, B. A. Scott, and R. Tsui, Chemtronics, $\underline{1}$, 150 (1986).

[6]Y. J. Chabal, Surf. Sci. $\underline{168}$, 594 (1986); V. A. Burrows, Y. J. Chabal, G. S. Higashi, K. Raghavachari, and S. B. Christman, Appl. Phys. Lett. $\underline{53}$(11), 998 (1988).

[7]R. M. Robertson, D. M. Golden, and M. J. Rossi, J. Vac. Sci. Technol. A $\underline{6}$, 1407 (1988).

[8]R. M. Robertson, D. M. Golden, and M. J. Rossi, J. Vac. Sci. Technol. B $\underline{6}$,1632 (1988).

[9]R. M. Robertson, D. M. Golden, and M. J. Rossi, J. Chem. Phys. $\underline{89}$, 2925 (1988).

[10]R. M. Robertson, D. M. Golden, and M. J. Rossi, J. Phys. Chem. $\underline{92}$, 5338 (1988).

[11]R. M. Robertson and M. J. Rossi, Appl. Phys. Lett., $\underline{54}$(2), 185 (1989).

[12]C. E. Moore, "Atomic Energy Levels," Natl. Stand. Ref. Data Ser., Natl. Bur. Stand. No. 35, Vols. 2 and 3 (US GPO, Washington, D. C., 1971).

[13]S. W. Benson, O. Kondo, and R. M. Marshall, Int. J. Chem. Kinet. $\underline{19}$, 829 (1987).

[14]M. J. Rossi, J. R. Pladziewicz, and J. R. Barker, J. Chem. Phys. $\underline{78}$, 6695 (1983).

[15]J. R. Barker and R. E. Golden, J. Phys. Chem. $\underline{88}$, 1012 (1984).

[16]M. T. Duignan, J. W. Hudgens, and J. R. Wyatt, J. Phys. Chem. $\underline{86}$, 4156 (1982).

[17]J. S. Francisco, S. A. Joyce, J. I. Steinfeld, and F. Walsh, J. Phys. Chem. $\underline{88}$, 3098 (1984).

[18]B. A. Sawrey, H. E. O'Neal, and M. A. Ring, Organometallics $\underline{6}$, 720 (1987).

[19]B. A. Sawrey, H. E. O'Neal, M. A. Ring, and D. Coffey, Jr., Int. J. Chem. Kinet. $\underline{16}$, 801 (1984).

[20]J. S. Francisco and H. B. Schlegel, J. Chem. Phys. $\underline{88}$, 3736 (1988).

[21]D. M. Rayner, R. P. Steer, P. A. Hackett, C. L. Wilson, and P. John, Chem. Phys. Lett. $\underline{123}$, 449 (1986).

[22]J. W. Thoman and J. I. Steinfeld, Chem. Phys. Lett. $\underline{124}$, 35, (1986).

[23] C. D. Eley, M. C. A. Rowe, and R. Walsh, Chem. Phys. Lett. 126, 153 (1986).

[24] J. O. Chu, D. B. Beach, and J. M. Jasinski, J. Phys. Chem. 91, 5340 (1987).

[25] J. M. Jasinski and J. O. Chu, J. Chem. Phys. 88, 1678 (1988).

[26] Y. Mishima, M. Hirose, Y. Osaka, K. Nagamine, Y. Ashida, N. Kitagawa, and K. Isogaya, Jpn. J. Appl. Phys. 22, L46 (1983).

[27] T. Iwanaga and M. Hanabusa, Jpn. J. Appl. Phys. 23, L473 (1984).

[28] G. W. Bethke and M. K. Wilson, J. Chem. Phys. 26, 1107 (1957).

[29] F. W. Lampe, Spectrochim. Acta A43, 257 (1987).

[30] J. G. Martin, M. A. Ring, and H. E. O'Neal, Int. J. Chem. Kinet. 19, 715 (1987).

[31] R. D. Johnson III and J. W. Hudgens, Chem. Phys. Lett. 141, 163 (1987).

[32] S. Francisco, R. Barnes, and J. W. Thoman, J. Chem. Phys. 88, 2334 (1988).

[33] C. M. Van Zoeren, J. W. Thoman, Jr., J. I. Steinfeld, and M. W. Rainbird, J. Phys. Chem. 92, 9 (1988).

[34] J. Berkowitz, J. P. Green, H. Cho, and B. Ruscic, J. Chem. Phys. 86, 1235 (1987).

[35] G. Olbrich, Chem. Phys. 101, 381 (1986).

[36] M. E. Coltrin, R. J. Kee, and J. A. Miller, J. Electrochem. Soc. 133, 1206 (1986).

[37] M. J. Kushner, J. Appl. Phys. 63, 2532 (1988).

[38] P. M. Agrawal, D. L. Thompson, and L. M. Raff, Surface Sci. 195, 283 (1988).

31

FIGURES

FIG. 1. The VLPΦ reactor, drawn to scale, used to measure sticking coefficients in the range 0.01 to 0.5. The inner tube is 16.5 mm in diameter and 210 mm long.

FIG. 2. Energy level diagram for the REMPI of I, $CF_3I^{\ddagger}$, and CF_3.

FIG. 3. Time dependence of the total REMPI signals at 474.5 nm (circles, represent I) and 477.8 nm (squares represent $CF_3I^{\ddagger}$). The CF_3I pressure was 1.1×10^{-3} Torr, and the extent of depletion was ~2% at the repetition rate of 11 Hz.

FIG. 4. Time dependence of the total REMPI signal at 455.6 nm (CF_3). The HFA pressure was 1.1×10^{-3} Torr, and the extent of depletion was 10% at the repetition rate of 11 Hz. The solid point on the right vertical axis represents the amount of signal present at 90 ms.

FIG. 5. REMPI spectra of the products of the IRMPD of n-butylsilane in the wavelength range 485 to 520 nm (Coumarin 503 dye.) The pressure was 0.16×10^{-3} Torr, the depletion was 12%, and the delay time was 20 μs. The dye laser pulse energy was 2.6 mJ at 500 nm and 0.8 mJ at 488 nm.

FIG. 6. Comparison of the REMPI spectra of the products of the IRMPD of n-butylsilane and disilane (Coumarin 500 dye; the center of the power curve is shifted slightly from that of Coumarin 503). For both precursors, the pressure was 0.6×10^{-3} Torr, and the delay time was 5 μs. The dye laser pulse energies were 3 mJ at 500 nm and 2 mJ at 488 nm. For n-butylsilane, the depletion was 7%, and the vertical scale was 0.5 V per division. For disilane, the depletion was less than 1%, and the vertical scale was 50 mV per division.

FIG. 7. Energy level diagram for the REMPI of $SiH_2^{\ddagger}$ and SiH_2.

Fig. 8. REMPI spectra of the products of the IRMPD of n-butylsilane in the wavelength range 335 to 345 nm (p-terphenyl dye). The pressure was 0.7 $\times 10^{-3}$ Torr, the depletion was ~1-10%, and the delay time was 5 μs. The dye laser pulse energy was 0.4 mJ at the maximum of the power curve, near 342 nm.

FIG. 9. REMPI spectra of the products of the IRMPD of n-butylsilane in the wavelength range 345 to 370 nm (DMQ dye.) The pressure was 0.9×10^{-3} Torr, the depletion was ~1-10%, and the delay time was 5 μs. The dye laser pulse energy was 1.1 mJ at the maximum (663 nm), falling to 0.5 mJ at 350 nm.

FIG. 10. Time dependence of the total REMPI signals at 487.9 (crosses) and 500 nm (triangles), representing $SiH_2^{\ddagger}$ and SiH_2, respectively; n-butylsilane pressure was 1.2×10^{-3} Torr, and the depletion was ~1-

10%. The signal at 500 nm at 90 ms was 76 (arbitrary units) and decreased to zero without IR radiation. The 487.9 nm signal was zero at 90 ms and without IR radiation.

FIG. 11. Time dependence of the total REMPI signal at 349.3 nm, representing SiH_2. The n-butylsilane pressure was 0.9×10^{-3} Torr, and the depletion was ~1-10%.

FIG. 12. (a) Variation of k_1 with n-butylsilane pressure. The extent of depletion for this data set was less than 5%. (b) Variation of the normalized mass spectrometer signal at m/e - 88 with the pressure of n-butylsilane. The extent of depletion by IRMPD is given by low pressure intercept, ~1-15%.

FIG. 13. Mass spectrometric scans, with the IR laser on and off, in the mass region from m/e - 88 (parent peak of n-butylsilane) to m/e - 118 (parent peak of n-butyldisilane). The n-butylsilane pressure was 5.5×10^{-3} Torr.

FIG. 14. Time dependence of the total REMPI signals at 487.9 (crosses) and 495 nm (triangles), representing $SiH_2^{\ddagger}$ and SiH_2, respectively. Disilane pressure was 2.6×10^{-3} Torr, and the extent of depletion was less than 2%. The signal at 495 nm at 90 ms (same as without IR) was 690 (arbitrary units). The signal at 487.9 nm at 90 ms and without IR was 7.

Table I

CHARACTERISTIC RATE CONSTANTS FOR THE VLPΦ/REMPI EXPERIMENT
The appropriate time scales for M = SiH_2 are also shown

Process		Analytic Expression	Rate Constant (S^{-1})	Time Constant for SiH_2
Production				2 μs
Dilution	k_d	~v_{th}/r_b	$30000(T/M)^{1/2}$	10 μs
Wall collision	ω	$v_{th}A_{eT}/4V_T$	$9000(T/M)^{1/2}$	35 μs
Escape from tube	k_{eT}	$v_{th}A_{eT}/4V_T$	$135(T/M)^{1/2}$	2.3 ms
Escape from reactor	k_{eR}	$v_{th}A_{eR}/4V_R$	$0.24(T/M)^{1/2}$	1.3 s

*T is the temperature in Kelvin, M is the molecular mass in atomic units, v_{th} is the average thermal velocity of M, r_B is the radius of the laser beam generating the neutral transient, A and V are the area and the volume of the inner tube (T) and the Knudsen cell (R), respectively. For the escape rate constants, the subscript e refers to the area of the respective escape apertures.

Table II

STICKING COEFFICIENT RESULTS

Transients	Precursor	λ (nm)	Pressure (10^{-3}Torr)	f	k_d ($1000\ s^{-1}$)	C_d	k_1 ($1000\ s^{-1}$)	γ
I	CF_3I	474.5	1.1	0.02	38	4.2	2.2	0.16
CF_3I[#]	CF_3I	477.8	1.1	0.02	22	8	--	>0.5
CF_3	HFA	455.6	1.1	0.1	97	14	--	<0.01
SiH_2[#]	$n-BuSiH_3$	487.9	1.3	0.1	63	500	--	>0.5
SiH_2	$n-BuSiH_3$	487.9	1.3	0.1	--	--	2.7	0.09
$Si\dot{H}_2$	$n-BuSiH_3$	500	1.3	0.1	58	20	3.2	0.11
SiH_2	$n-BuSiH_3$	495	1.2	0.2	58	40	2.5	0.09
SiH_2	$n-BuSiH_3$	349.3	0.9	0.14	62	18	3.1	0.11
SiH_2	$n-BuSiH_3$	349.3	0.6	0.11	64	13	2.3	0.08
SiH_2	$n-BuSiH_3$	362.5	0.8	0.11	--	--	2.4	0.07
SiH_2	$n-BuSiH_3$	340	1.0	0.1	49	7	3	0.1
SiH_2[#]	Si_2H_6	487.9	2.6	<0.02	59	500	--	>0.5
SiH_2[#]	Si_2H_6	487.9	2.6	<0.02	--	--	3.4	0.12
SiH_2	Si_2H_6	495	2.6	<0.02	60	18	4.9	0.17

Gas Inlet
Inner Tube

(-90 V)

CO₂
Laser

70-mm
Lens

Dye Laser

(+90 V)
MPI Signal
Electrodes

To Mass
Spectrometer

Butterfly
Valve
with 3mm
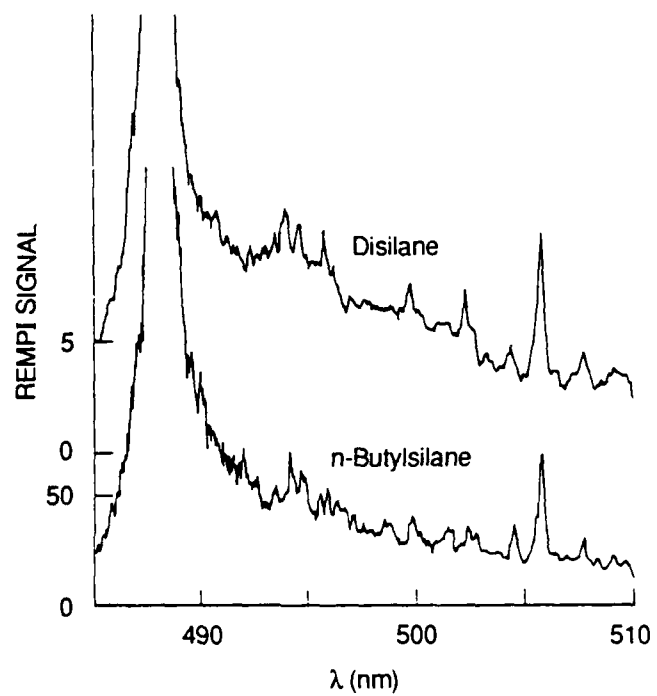Aperture
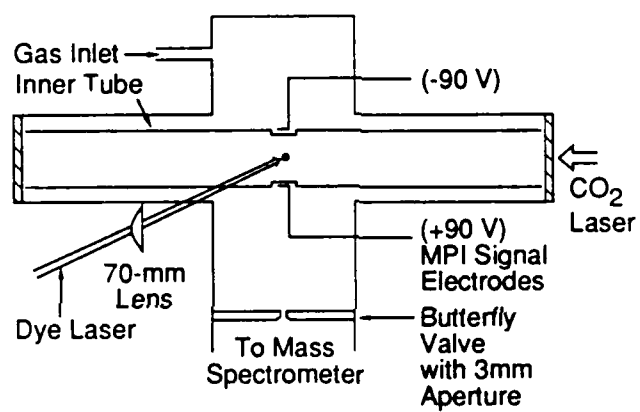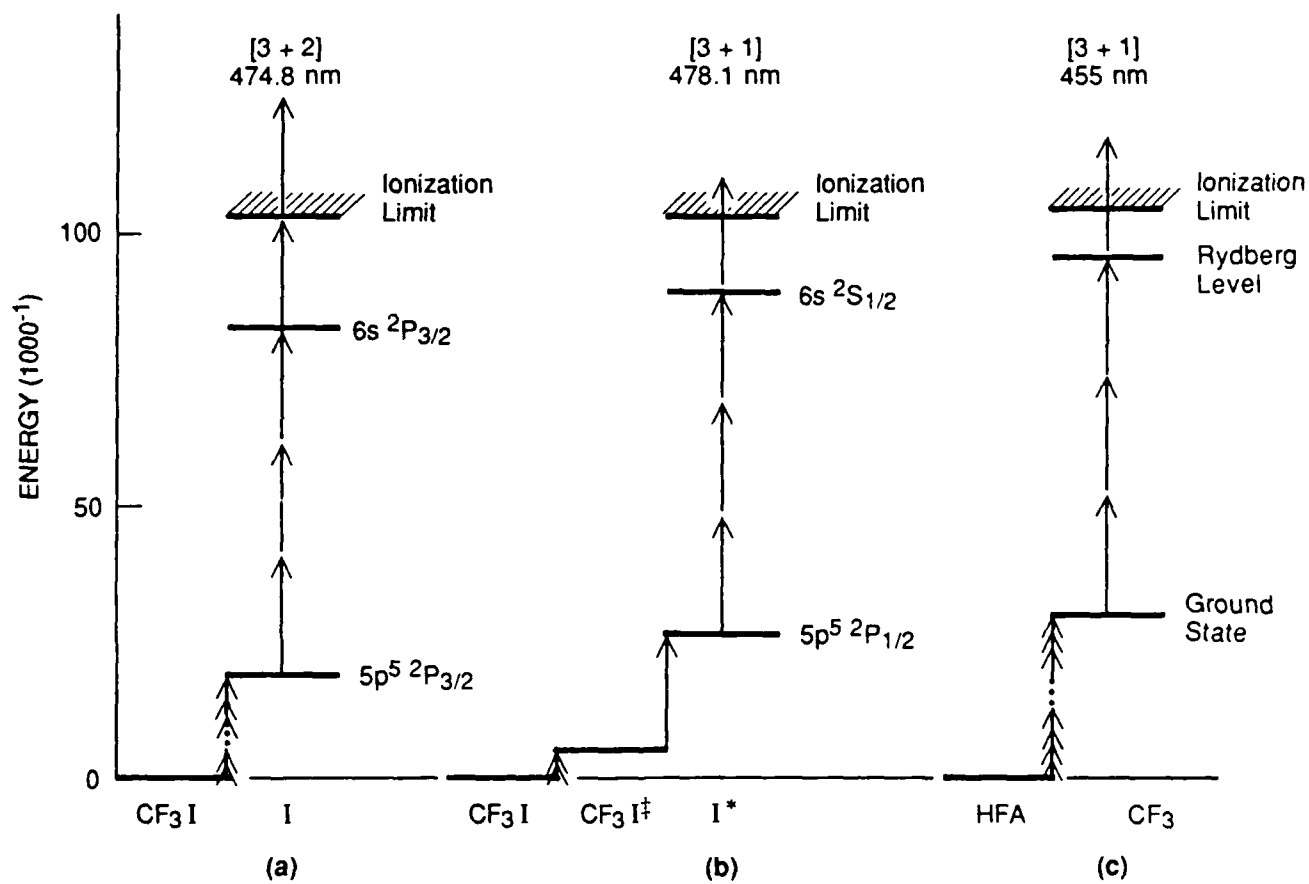
RA-M-1227-37B
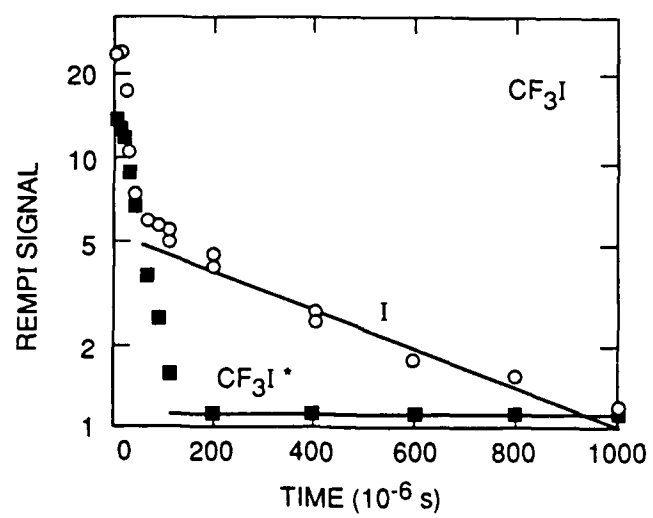
Figure 1
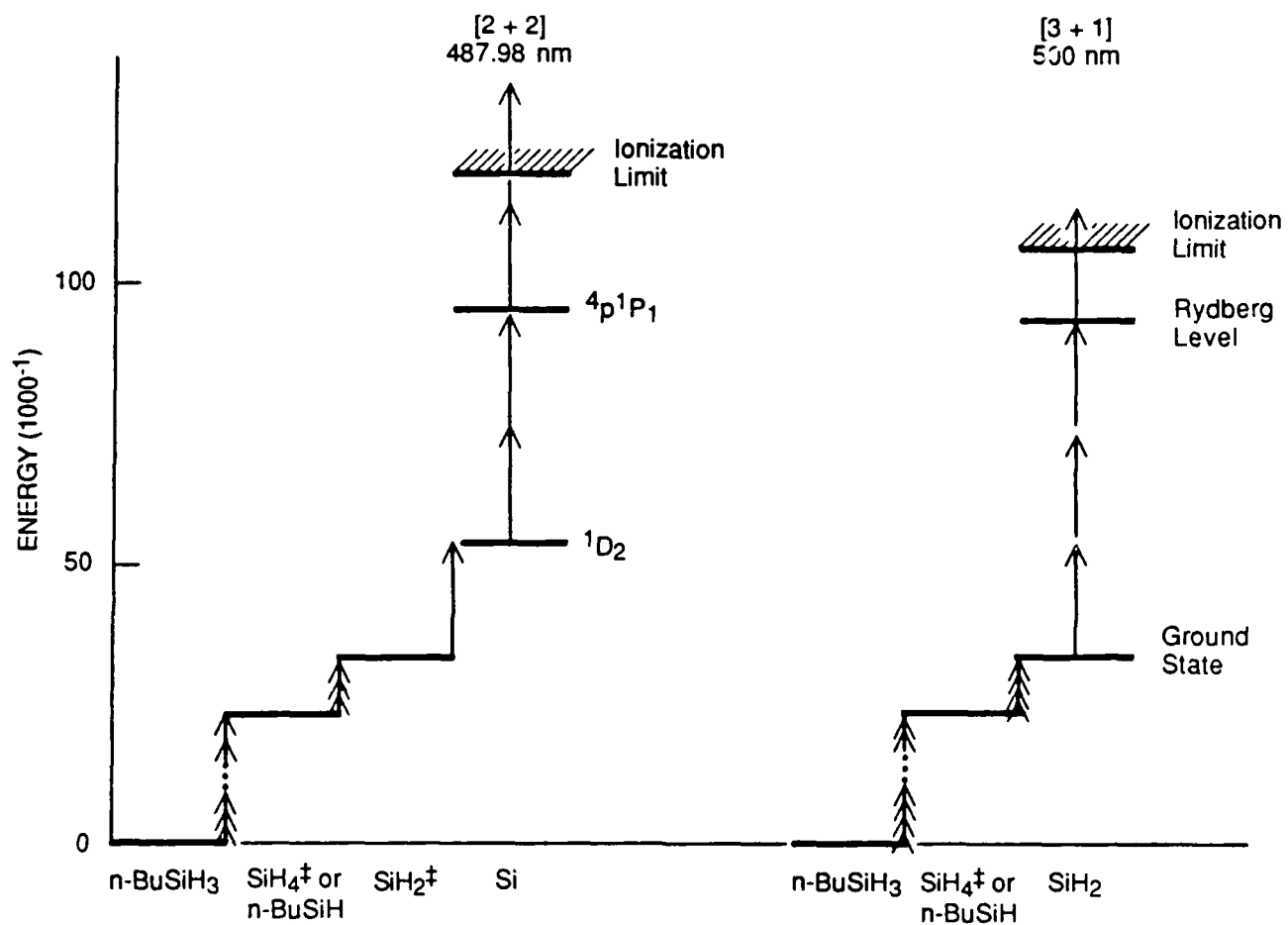
Figure 2

RA-M-1227-42
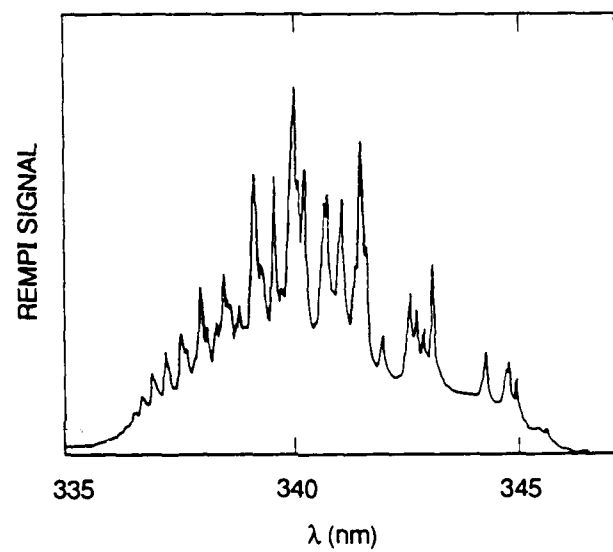
Figure 3
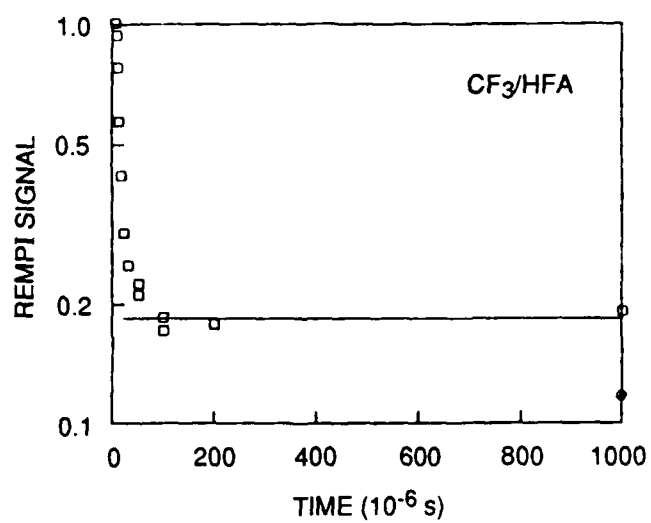
RA-1227-45

Figure 4
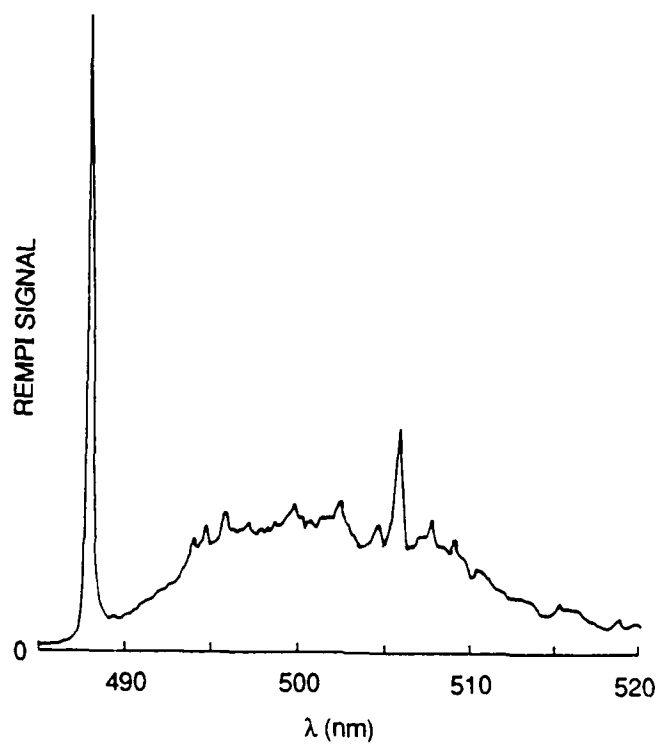
RA-1227-41

Figure 5

RA-320522-172A

Figure 6

Figure 7

REMPI SIGNAL

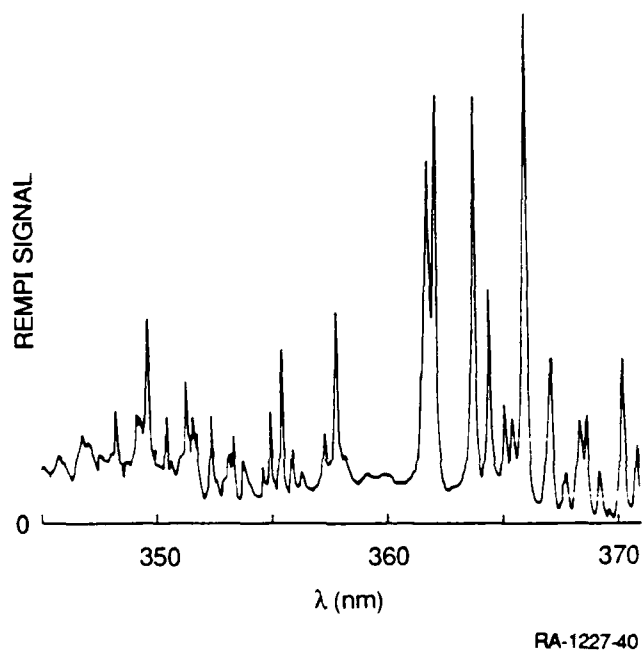335   340   345
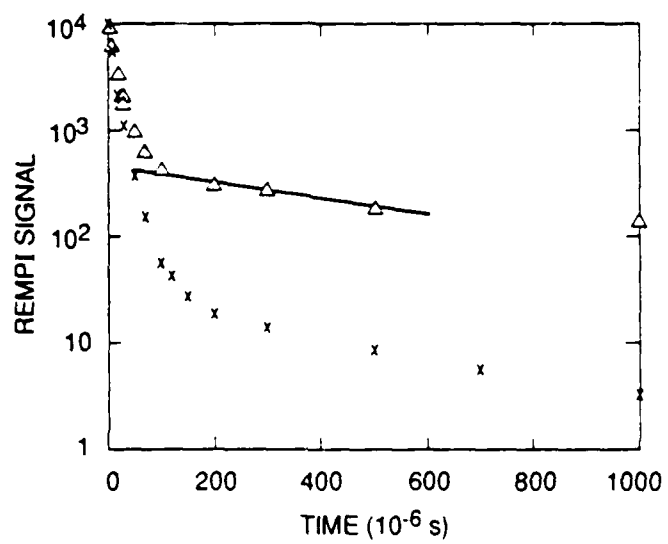
λ (nm)

RA-320522-173A

Figure 8

REMPI SIGNAL

λ (nm)

RA-1227-40

Figure 9
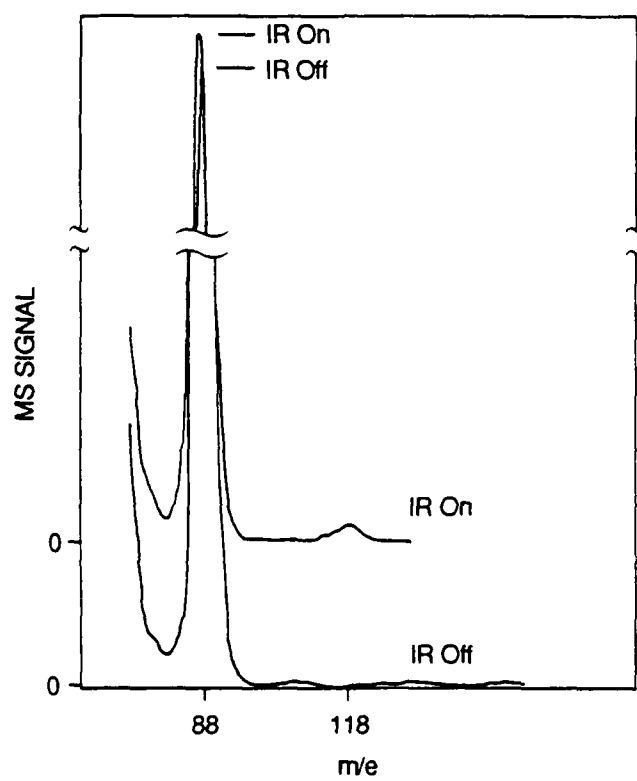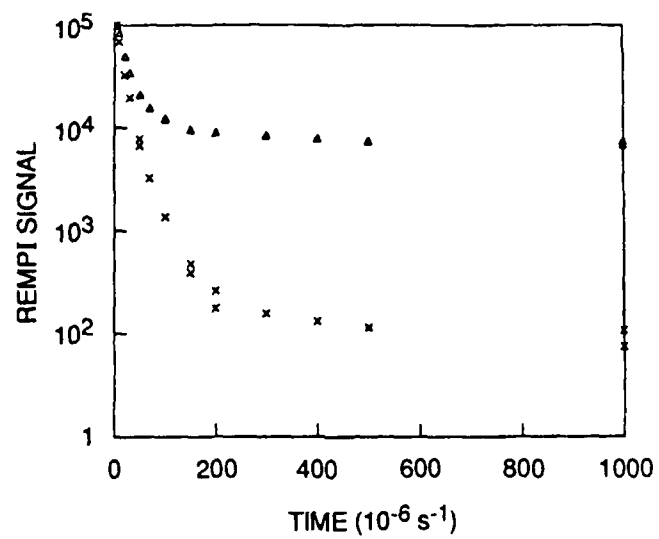
RA-320522-171C

Figure 10
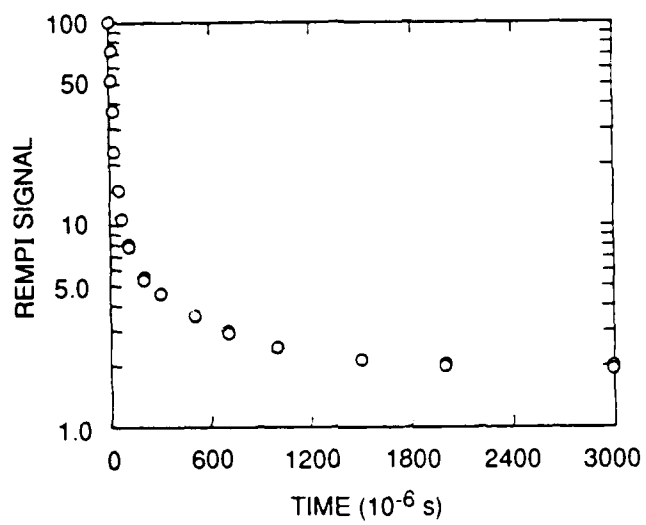
RA-320522-174B
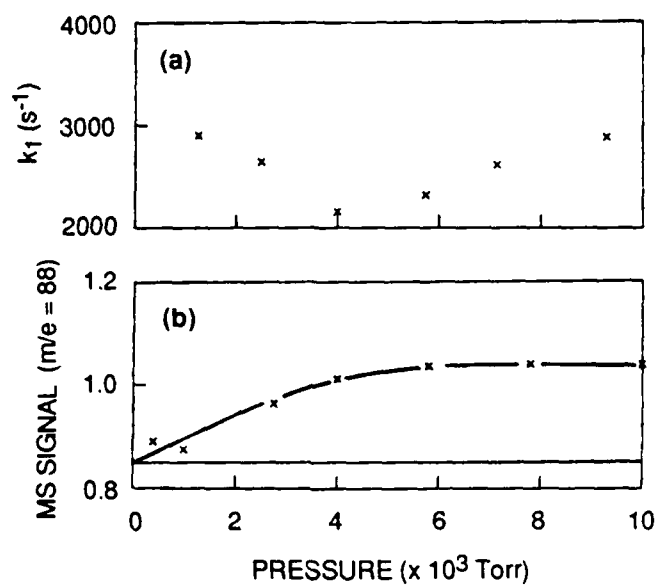
Figure 11

RA-330525-17A

Figure 12

RA-320525-27A

Figure 13

RA-1227-44

Figure 14